The Astronomical Journal, 153:111 (49pp), 2017 March doi:10.3847/1538-3881/153/3/111

Galaxy And Mass Assembly (GAMA): Gas Fueling of Spiral Galaxies in the Local Universe. I. The Effect of the Group Environment on Star Formation in Spiral Galaxies

M. W. Grootes[1,2], R. J. Tuffs[1], C. C. Popescu[1,3,4], P. Norberg[5], A. S. G. Robotham[6,7], J. Liske[8], E. Andrae[1], I. K. Baldry[9], M. Gunawardhana[5], L. S. Kelvin[9], B. F. Madore[10], M. Seibert[10], E. N. Taylor[11], M. Alpaslan[12], M. J. I. Brown[13], M. E. Cluver[14], S. P. Driver[7,15], J. Bland-Hawthorn[16], B. W. Holwerda[17], A. M. Hopkins[18], A. R. Lopez-Sanchez[18], J. Loveday [19], and M. Rushton[1,3,4]

[1] Max-Planck-Institut für Kernphysik, Saupfercheckweg 1, D-69117 Heidelberg, Germany; mgrootes@cosmos.esa.int, meiert.grootes@mpi-hd.mpg.de
[2] ESA/ESTEC SCI-S, Keplerlaan 1,2201 AZ, Noordwijk, The Netherlands
[3] Jeremiah Horrocks Institute, University of Central Lancashire, Preston PR1 2HE, UK
[4] The Astronomical Institute of the Romanian Academy, Str. Cutitul de Argint 5, Bucharest, Romania
[5] Institute for Computational Cosmology, Department of Physics, Durham University, Durham DH1 3LE, UK
[6] University of Western Australia, Stirling Highway Crawley, WA 6009, Australia
[7] International Centre for Radio Astronomy Research (ICRAR), University of Western Australia, Stirling Highway Crawley, WA 6009, Australia
[8] Hamburger Sternwarte, Universität Hamburg, Gojenbergsweg 112, D-21029 Hamburg, Germany
[9] Astrophysics Research Institute, Liverpool John Moores University, Twelve Quays House, Egerton Wharf, Birkenhead, CH41 1LD, UK
[10] Observatories of the Carnegie Institution for Science, 813 Santa Barbara Street, Pasadena, CA 91101, USA
[11] School of Physics, the University of Melbourne, Parkville, VIC 3010, Australia
[12] NASA Ames Research Center, N232, Moffett Field, Mountain View, CA 94035, USA
[13] School of Physics and Astronomy, Monash University, Clayton, Victoria 3800, Australia
[14] University of the Western Cape, Robert Sobukwe Road, Bellville, 7535, South Africa
[15] Scottish Universities' Physics Alliance (SUPA), School of Physics and Astronomy, University of St Andrews, North Haugh, St Andrews, KY16 9SS, UK
[16] Sydney Institute for Astronomy, School of Physics, University of Sydney NSW 206, Australia
[17] Leiden Observatory, University of Leiden, Niels Bohrweg 2, 2333 CA Leiden, The Netherlands
[18] Australian Astronomical Observatory, P.O. Box 915, North Ryde, NSW 1670, Australia
[19] Astronomy Centre, University of Sussex, Falmer, Brighton BN1 9QH, UK

Received 2016 April 4; revised 2016 December 9; accepted 2016 December 18; published 2017 February 15

Abstract

We quantify the effect of the galaxy group environment (for group masses of $10^{12.5}$–$10^{14.0}\,M_e$) on the current star formation rate (SFR) of a pure, morphologically selected sample of disk-dominated (i.e., late-type spiral) galaxies with redshift $\lesssim 0.13$. The sample embraces a full representation of quiescent and star-forming disks with stellar mass $M_* \gtrsim 10^{9.5} M_e$. We focus on the effects on SFR of interactions between grouped galaxies and the putative intrahalo medium (IHM) of their host group dark matter halos, isolating these effects from those induced through galaxy–galaxy interactions, and utilizing a radiation transfer analysis to remove the inclination dependence of derived SFRs. The dependence of SFR on M_* is controlled for by measuring offsets $\Delta\log(\psi_*)$ of grouped galaxies about a single power-law relation in specific SFR, $y_* \propto {}_{*}$ $M^{-0.45\pm0.01}$, exhibited by non-grouped "field" galaxies in the sample. While a small minority of the group satellites are strongly quenched, the group centrals and a large majority of satellites exhibit levels of ψ_* statistically indistinguishable from their field counterparts, for all M_*, albeit with a higher scatter of 0.44 dex about the field reference relation (versus 0.27 dex for the field). Modeling the distributions in $\Delta\log(\psi_*)$, we find that (i) after infall into groups, disk-dominated galaxies continue to be characterized by a similar rapid cycling of gas into and out of their interstellar medium shown prior to infall, with inflows and outflows of ~1.5–5 x SFR and ~1–4 x SFR, respectively; and (ii) the independence of the continuity of these gas flow cycles on M_* appears inconsistent with the required fueling being sourced from gas in the circumgalactic medium on scales of ~100 kpc. Instead, our data favor ongoing fueling of satellites from the IHM of the host group halo on ~Mpc scales, i.e., from gas not initially associated with the galaxies upon infall. Consequently, the color–density relation of the galaxy population as a whole would appear to be primarily due to a change in the mix of disk- and spheroid-dominated morphologies in the denser group environment compared to the field, rather than to a reduced propensity of the IHM in higher-mass structures to cool and accrete onto galaxies. We also suggest that the required substantial accretion of IHM gas by satellite disk-dominated galaxies will lead to a progressive reduction in the specific angular momentum of these systems, thereby representing an efficient secular mechanism to transform morphology from star-forming disk-dominated types to more passive spheroid-dominated types.

Key words: galaxies: fundamental parameters – galaxies: groups: general – galaxies: ISM – galaxies: spiral – intergalactic medium – surveys

Supporting material: data behind figures

1. Introduction

The current paradigm of galaxy formation (e.g., Rees & Ostriker 1977; White & Rees 1978; Fall & Efstathiou 1980; White & Frenk 1991; Mo et al. 1998) holds that luminous

galaxies form and initially evolve as disk galaxies at the center of isolated dark matter halos (DMHs). Under this paradigm, as dark matter (DM) overdensities decouple from the large-scale flow and collapse, the baryons of the ambient intergalactic

medium bound to the potential well of the nascent DMH will collapse and shock-heat at some radius comparable or interior to the virial radius of the halo, giving rise to a pressure-supported (and thereby dynamically decoupled from the DM) intrahalo medium (IHM). Subsequently, radiative cooling of the baryons of the IHM will precipitate the further infall of some fraction of the gas toward the center of the DMH. The angular momentum of the cooling baryons, built up from the torques exerted by the tidal shear in the earlier large-scale flow of DM (e.g., Fall & Efstathiou 1980), is thereby transported from the IHM into a rotationally supported disk of cold gas on some smaller scale related to the specific momentum of the halo (e.g., van den Bosch et al. 2002; Bett et al. 2010; Hahn et al. 2010). The surface density of gas in the disk increases as gas from the IHM continues to be accreted, until it becomes sufficient for the formation of dense, self-gravitating clouds that rapidly collapse to form stars, which then trace the disk as a visible galaxy. The rotationally supported gas in the disk therefore constitutes an interstellar medium (ISM), at least interior to some radius where the surface density of gas exceeds the threshold for star formation.

In the subsequent evolution, the galaxy will continue to accrete gas, thus fueling ongoing star formation in its disk; including gas from the initial IHM, but mainly from secondary infall, i.e., baryons from the ambient IGM of the surrounding large-scale structure infalling onto the DMH (Fillmore & Goldreich 1984; Bertschinger 1985; Pichon et al. 2011). Accordingly the net rate of accretion from the IHM into the ISM of the galaxy, and thereby the availability of fuel for star formation, will be determined by (i) the *maximum achievable* rate at which accretable, i.e., sufficiently cool, gas can be delivered to the galaxy, as determined by the properties of the large-scale environment, in particular the DMH; and (ii) feedback from processes in the galaxy predicted to regulate the accretion of IHM onto the galaxy.

A generic expectation of the accretion of IGM onto a DMH is the formation of an accretion shock (Binney 1977). However, the formation and radial location of a stable shock depend on the cooling timescale in the post-shock gas being longer than the free-fall timescale in order to establish and maintain a pressure-supported atmosphere/IHM supporting the shock (Rees & Ostriker 1977; White & Frenk 1991; Birnboim & Dekel 2003). In halos where this is not the case at any radius exterior to the galaxy at the center, the IGM being accreted onto the halo will continue to the galaxy on the free-fall timescale, resulting in a highly efficient maximum achievable fueling rate limited by the cosmological accretion rate onto the DMH, commonly referred to as "cold-mode" accretion (Kereš et al. 2005; Dekel & Birnboim 2006). Conversely, in halos capable of supporting a shock, the infalling IGM will be shock-heated and remain hot until it radiatively cools on the cooling timescale, resulting in a less efficient maximum fueling rate determined by the cooling timescale, so-called "hot-mode" accretion (Kereš et al. 2005; Dekel & Birnboim 2006). As the cooling timescale depends, inter alia, on the temperature of the post-shock gas, and as such on the depth of the potential well of the DMH, i.e., its mass, this introduces an environmental dependence into the process of gas fueling in the form of a transition between fueling modes at a certain halo mass and an additional halo mass dependence within the "hot-mode" fueling (Rees & Ostriker 1977; White & Frenk 1991; Benson et al. 2001; Birnboim & Dekel 2003; Kereš et al. 2005; Dekel & Birnboim 2006; Benson & Bower 2011; van de Voort et al. 2011). For cosmological DMH detailed thermodynamic considerations of this process find a transition mass between these two modes, i.e., where the free-fall timescale equals the cooling timescale at the virial radius of $\sim 10^{11}$–$10^{12}\,M_{\odot}$ (Kereš et al. 2005; Dekel & Birnboim 2006).[20] As such, the accretion in low-mass halos, and thus predominantly in the early universe, is dominated by cold-mode accretion, while hot-mode accretion becomes increasingly relevant at lower redshifts and in the present universe (e.g., Dekel et al. 2013).

The net rate of accretion from the IHM into the ISM of the galaxy, and thereby the availability of fuel for star formation, however, will not be determined by the maximum achievable fueling rate alone. Rather, the accretion of IHM into the ISM is predicted to be subject to regulation by galaxy-specific feedback linked to energetic processes in the galaxy, e.g., star formation and active galactic nucleus (AGN) activity. This feedback includes the mechanical removal of gas from the ISM, as well as the heating of the IHM, preventing it from cooling.[21] Feedback from star formation, i.e., from supernovae, is predicted to remove gas from the ISM of the galaxy, most efficiently for low-mass galaxies. While star formation and thus stellar feedback are intrinsically stochastic processes, the feedback will evolve into a near-steady-state relation as galaxies grow large enough to support widespread star formation activity, although the efficiency of stellar feedback in removing ISM from the galaxy will decrease with increasing mass of the galaxy/depth of the potential well (e.g., Faucher-Giguère et al. 2011; Hopkins et al. 2013, and references therein), leading to a self-regulated level of accretion of gas from the IHM into the ISM. For the most massive galaxies, residing in massive DMH, AGN feedback from the black hole at the center of the galaxy, heating the IHM and preventing it from cooling and being accreted, is predicted to dominate the feedback from the galaxy (e.g., Fabian 2012, and references therein). Unlike star-formation-driven feedback, where a quasi-steady-state relation is expected, AGN feedback, which is still a major subject of investigation, may always be stochastic in nature (e.g., Pope 2007; Pavlovski & Pope 2009; Hickox et al. 2014; Werner et al. 2014). Overall, the growth of the galaxy will thus continue until the supply of gas from the IHM is interrupted, e.g., by the galaxy being shifted away from the center of the potential well by a merging event with another halo of comparable or larger mass, or by the activity of an AGN efficiently heating the IHM.

In summary, for galaxies at the center of their DMH—so-called centrals—basic physical considerations founded on the current paradigm of galaxy formation predict the rate at which gas from the IHM is accreted into the ISM of the galaxy, i.e., its gas fueling, to be determined by a balance between the possible rate of accretion as set by the DMH and galaxy-specific feedback, thus displaying a dependence on both environmental and galaxy-specific properties. This picture is consistent with work on the abundance matching of galaxies with halos from

[20] It should be noted that the inflow of ambient IGM onto the halo will be anisotropic with preferential inflow along the filaments of the large-scale DM structure (Kereš et al. 2005, 2009; Brooks et al. 2009; Dekel et al. 2009; Pichon et al. 2011). Thus, the transition between cold and hot modes will not be sharp, as the filamentary flows of cold IGM may penetrate hot atmospheres. The degree to which this is the case is not yet clear, however, although penetration decreases with temperature and extent of the hot halo (Nelson et al. 2013).

[21] Feedback from the galaxy may also impact the cooling timescale in the post-shock gas by heating the IHM and/or enriching it with metals from the ISM.

DM simulations, which suggests that the efficiency of the conversion of baryons to stars is greatest in DMHs of $\sim 10^{12} M_{\odot}$ (Moster et al. 2010; Behroozi et al. 2013). Thus, regardless of the exact underlying cause, $10^{12} M_{\odot}$ represents a critical mass in understanding environment-dependent galaxy evolution and gas fueling in particular.

In addition to centrals, the hierarchical formation of large-scale structure expected for a ΛCDM universe gives rise to a population of so-called satellite galaxies, i.e., galaxies that are bound to their host DMH but are not at rest with respect to its center of mass, having been captured during the merging of two smaller DMHs. In the context of the flow of gas from the IHM into the ISM it is essential to distinguish between these two types of galaxy group members. While for centrals the physical processes—driven by galaxy–IHM interactions—that determine gas fueling can reasonably be expected to be similar to those of isolated field central galaxies, this is not the case for satellites. For satellites, their motion relative to a putative virialized hot IHM introduces further galaxy–IHM interactions, which may affect the rate of accretion of gas from the IHM into the ISM of the galaxy, as well as the gas content of the ISM and of any circumgalactic reservoirs of gas bound to the galaxy (circumgalactic medium [CGM]). This includes ram pressure stripping of the ISM of galaxies in the environment of galaxy clusters (and groups; e.g., Gunn & Gott 1972; Abadi et al. 1999; Hester 2006; Bahé & McCarthy 2015), as well as ram pressure stripping of the CGM of a galaxy in the galaxy group and low-mass cluster environment, a process often referred to as "strangulation" (e.g., Larson et al. 1980; Kimm et al. 2009), as it is thought to slowly limit star formation in the galaxy by removing the gas reservoirs from which star formation is fueled. Thus, satellite galaxies are expected to display suppressed star formation activity with respect to comparable field galaxies.

On the scale of massive clusters of galaxies, the predicted processes and trends have been observed, both directly by observations of ram-pressure-stripped tails of gas emanating from galaxies (Fumagalli et al. 2014) and indirectly by the frequent occurrence of galaxies in these massive clusters truncated in Hα and by a prevalence of galaxies with red colors and suppressed star formation rate (SFR; e.g., Koopmann & Kenney 1998, 2004; Gavazzi et al. 2013).

An empirical quantification of the predictions on the scale of lower-mass galaxy groups, however, has proven challenging, as the ram pressure stripping of the ISM and CGM is expected to be less severe and potentially even limited to the CGM (e.g., Kawata & Mulchaey 2008; McCarthy et al. 2008; but see also Hester 2006; Bahé & McCarthy 2015, for a contrasting view), necessitating a statistical consideration of the galaxy group population to discern the impact of the group environment on these galaxies. In order to observationally identify galaxy groups, many works (e.g., Smail et al. 1998; Balogh et al. 2002; Pimbblet et al. 2002, 2006; Jeltema et al. 2006; Urquhart et al. 2010; Erfanianfar et al. 2014) have made use of X-ray-selected samples, for which properties of the DMH such as mass may be deduced from the X-ray emission. However, samples selected in this manner may be biased toward more massive DMHs and against the more ubiquitous (and therefore arguably more important) loose, low- and intermediate-mass galaxy groups. To circumvent this potential bias, with the onset of wide-field spectroscopic galaxy surveys, many studies have made use of optically defined spectroscopic galaxy group catalogs (e.g., Gómez et al. 2003; Balogh et al. 2004, 2016; Kauffmann et al. 2004; Collister & Lahav 2005; Robotham et al. 2006; Weinmann et al. 2006, 2010; van den Bosch et al. 2008; Pasquali et al. 2009; Hester 2010; van der Wel et al. 2010; Peng et al. 2012; Wheeler et al. 2014). These, however, suffer from the relatively low spectroscopic completeness in dense regions achieved by most spectroscopic surveys, such that the majority of galaxies in lower-mass halos are central galaxies rather than satellites, and the halo masses assigned to each group depend on the shape of the assumed halo mass function. An alternative approach, pursued by a number of authors, has been to consider the (marked) correlation functions of galaxy samples drawn from spectroscopic surveys and to consider the clustering properties of red and blue galaxies (e.g., Blanton & Berlind 2007; Skibba et al. 2009; Zehavi et al. 2011). While largely model independent, this approach makes linking observations of galaxy properties to the properties of their host group difficult. Nevertheless, in general, all these works have found the fraction of red and quiescent galaxies to be larger in galaxy groups than in the field, in line with expectations, leading to the general assumption that galaxies are cut off from gas fueling upon becoming satellites, although the exact combination, importance, and effectivity of the processes assumed to be responsible remain a subject of debate (e.g., Blanton & Berlind 2007; van den Bosch et al. 2008; Kimm et al. 2009; Pasquali et al. 2009; Hester 2010; Wetzel et al. 2013, 2014; McGee et al. 2014; Peng et al. 2015).

Interpreting such observations in terms of the gas fueling and ISM content of galaxies and its relation to the group environment, however, is subject to a number of compounding problems, foremost among which is that of galaxy morphology. Empirically, the abundance of spheroidal galaxies is known to be higher in denser environments, corresponding to galaxy clusters (and to a lesser extent galaxy groups), than among largely isolated field galaxies (e.g., Dressler 1980; Goto et al. 2003; Bamford et al. 2009), i.e., it is higher in the higher-mass DMHs of these objects. However, it is not clear to what extent spheroidal galaxies are capable of retaining cold gas and sustaining significant star formation for any prolonged period (e.g., Oosterloo et al. 2010; Smith et al. 2012). In other words, while copious amounts of cold gas are observed in rotationally supported disk/spiral galaxies, the virial temperature of spheroidal pressure-supported systems is well above that conducive to forming and maintaining giant molecular clouds. Thus, the prevalence of red, low specific SFR (sSFR) galaxies may actually be more indicative of transformative processes affecting the morphology of satellite galaxies than of effects linked to the supply of gas, making control of the galaxy morphology paramount to any empirically driven investigation of gas fueling.

Finally, the ability to interpret observations of the properties of group galaxies in the context of the gas fueling of these objects requires the ability to control for degeneracies in the observables arising from galaxy–IHM and galaxy–galaxy interactions, as well as that the observables considered be sensitive to changes on timescales $\lesssim 1$ Gyr, i.e., comparable to the typical dynamical timescale of galaxy groups and shorter than that to which properties such as red and blue fractions, stellar metallicity, and optical colors are sensitive. Accordingly, empirically probing gas fueling and its environmental dependencies requires a sample of known morphology probing the

environment down to the scale of low-mass groups of $\sim 10^{12} M_e$, for which the measurement of the gas content (or its proxy tracer) is sensitive to changes on the scale of 10^8 yr and for which the effects of galaxy–IHM interactions can be isolated. Thus, although a number of works have accounted for the morphology of their samples (e.g., Hashimoto et al. 1998; Bamford et al. 2009; Hester 2010), the fundamental process of gas fueling in the group environment currently lacks a direct incisive empirical reference with which to compare and constrain theoretical predictions.

In this paper (Paper I) and its companion papers in this series (M. W. Grootes et al. 2017, in preparation) we focus on remedying this situation and providing a direct empirical reference with which to compare predictions of gas fueling as a function of environment with a focus on galaxy groups. This work makes use of a sample of galaxies of known uniform disk-dominated morphology (which we will refer to as spirals for simplicity), probing the full ranges of group environmental properties (e.g., DMH mass), galaxy-specific properties (e.g., stellar mass M_*, SFR), and galaxy properties related to the group environment (e.g., central or satellite, distance from group center). In identifying and selecting galaxy groups, we make use of the spectroscopic galaxy group catalog (the G3C; Robotham et al. 2011) of the Galaxy And Mass Assembly (GAMA) survey (Driver et al. 2011; Liske et al. 2015). This catalog samples the full mass range of galaxy groups (down to DMH masses of $\sim 10^{12} M_e$) with high completeness, enabling the determination of robust dynamical mass estimates, and represents the only resource of a statistically significant number of spectroscopic galaxy groups with kinematic determinations of the DMH mass down to low masses currently available.

Given the scarcity of direct measurements of the ISM content of galaxies in wide-field spectroscopic surveys,[22] in our analysis we make use of the SFR of a galaxy derived from its near-UV (NUV) emission, tracing star formation activity on timescales of $\sim 10^8$ yr (as shown in Figure 1), as a proxy measurement of its ISM content.

In addition to ensuring that the relation between ISM and star formation is as consistent as possible over the range of environments for the galaxies considered, controlling for galaxy morphology also aids in isolating the effects of galaxy–IHM interactions from those of galaxy–galaxy interactions, which may severely impact the SFR of galaxies (e.g., Robotham et al. 2014; Alatalo et al. 2015; Davies et al. 2015; Bitsakis et al. 2016). As major galaxy–galaxy interactions can strongly perturb disk galaxies and lead to a morphological transformation, focusing on disk-dominated galaxies ensures that no major merger has taken place, effectively enabling us, in combination with the deselection of close pairs of galaxies based on the G3C, to isolate the effects of galaxy–IHM interactions.

The plan of this paper is then as follows. In Section 2 we briefly describe the GAMA survey, as well as the relevant raw data products, followed by a description in Section 3 of the relevant derived physical properties. We then detail our sample selection and the resulting samples of disk-dominated/spiral galaxies in Section 4. Subsequently, we present our core empirical results on the sSFR–stellar mass relation and the distribution of sSFR for field and group spirals in Sections 5 and 6, as well as for central and satellite (group) spiral galaxies in Section 7. Making use of our samples and the relations derived, we investigate the star formation activity and star formation history (SFH) of group satellite spiral galaxies in Section 8, contrasting a range of simple parameterized SFHs with our observations to identify relevant elements of the SFH. In Section 9 we then consider our results on the star formation activity and history of spiral satellite galaxies in the context of the gas fueling cycle of these objects, including the implications of our results in terms of the gas reservoirs from which the gas fueling may be sourced. Finally, in Section 10 we discuss the broader implications of our results, and we summarize our results and conclude in Section 11.

In subsequent papers (M. W. Grootes et al. 2017, in preparation) we will focus on the gas fueling of central spiral galaxies and proceed with a detailed investigation of the impact of the group environment, as characterized, e.g., by the mass of the DMH, the mean galaxy density in the galaxy group, and the presence/absence of an AGN, on the gas fueling of our samples of satellite and central spiral galaxies in galaxy groups, again using the field spiral galaxies as a reference.

Throughout the paper, except where stated otherwise, we make use of magnitudes on the AB scale (Oke & Gunn 1983)

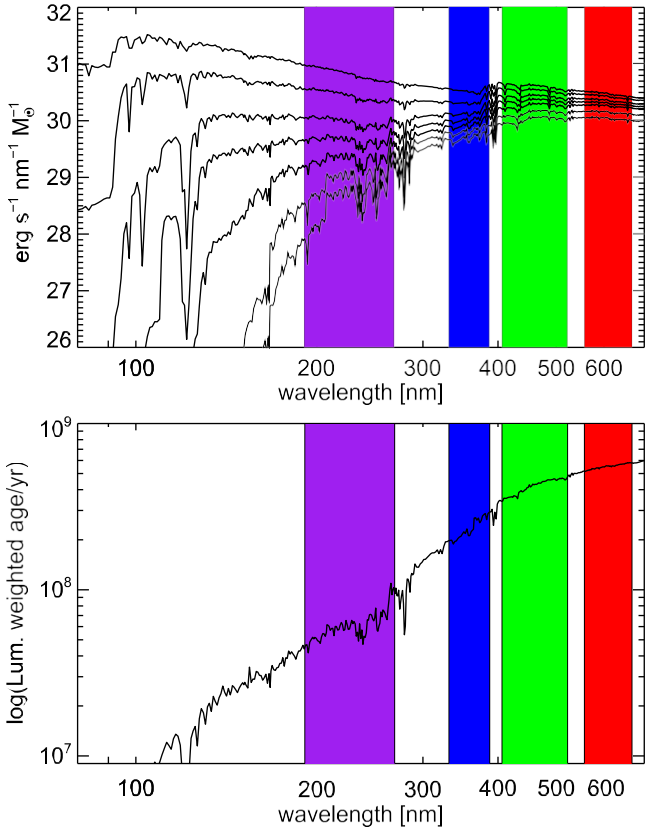

Figure 1. Top: mass-normalized spectral luminosity density as a function of wavelength. The spectra correspond to those of a galaxy that has been constantly forming stars until 0, 10, 100, 250, 500, 1000, and 2000 Myr ago (from top to bottom). Bottom: luminosity-weighted mean age of the emission of a galaxy with constant SFR as a function of wavelength. The shaded regions correspond to the *GALEX* NUV filter (purple) and the Sloan Digital Sky Survey (SDSS) u, g, and r bands (blue, green, and red, respectively).

[22] For wide-field spectroscopic surveys, direct measurements of the ISM content of the majority of surveyed galaxies are generally not available given the very long exposure time radio observations that would be required to obtain the necessary data. While this is currently also the GAMA survey, upcoming surveys using pathfinder facilities for the Square Kilometer Array (ASKAP DINGO; PI: M.Meyer) are striving to remedy this situation in the GAMA fields.

and an $\Omega_M = 0.3$, $\Omega_\Lambda = 0.7$, $H_0 = 70\,\mathrm{km\,s^{-1}\,Mpc^{-1}}$ cosmology (Spergel et al. 2003).

2. Data: The GAMA Survey

Our analysis of the effect of environment on the SFR and gas fueling of spiral galaxies is based on the GAMA survey (Driver et al. 2011). GAMA consists of a highly complete spectroscopic survey covering 286 deg^2 to a main survey limit of $r_{AB} \lesssim 19.8$ mag in three equatorial (G09, G12, and G15) and two southern (G02 and G23) regions using the 2dF instrument and the AAOmega spectrograph on the Anglo-Australian Telescope. Uniquely, the spectroscopic survey is accompanied by an associated multiwavelength database spanning the full UV–optical–far-IR (FIR)/submillimeter–radio spectrum. A full description of the survey is given in Driver et al. (2011) and Liske et al. (2015), with details of the spectroscopy provided in Hopkins et al. (2013) and details of the input catalog and tiling algorithm provided in Baldry et al. (2010) and Robotham et al. (2010), respectively. Importantly in the context of our investigation, GAMA has obtained science quality redshifts[23] for 263,719 target galaxies covering $0 < z \lesssim 0.5$ with a median redshift of $z \sim 0.2$ and an overall completeness of >98%[24] to its limiting depth. Due to its multipass nature and tiling strategy, this completeness remains constant even on small scales, i.e., is unaffected by the density of neighboring galaxies, enabling the construction of a high-fidelity galaxy group catalog extending to low-mass, low-multiplicity groups of $\gtrsim 10^{12}\,M_e$ (Robotham et al. 2011). For the work presented here we have made use of the first 3 yr of GAMA data—frozen and referred to as GAMA I—consisting of the three equatorial fields to a homogeneous depth of $r_{AB} \lesssim 19.4$ mag[25] (for both galaxies and galaxy groups). In the following we briefly present the GAMA data products relevant to this work.

2.1. GAMA Spectroscopy: Redshifts and Emission-line Measurements

Our main use of the spectroscopic data of the GAMA survey is in the form of redshift measurements, which have enabled the construction of the galaxy group catalog (Robotham et al. 2011). However, we also make use of the emission-line measurements to identify AGNs (as detailed in Section 3.2). Spiral galaxies hosting AGNs are not used, since the UV emission of such objects may no longer be a reliable tracer of their star formation activity. A full description of the GAMA spectroscopy is given in Hopkins et al. (2013), along with details of the quantitative measurement of emission lines, while the determination of redshifts from the spectra is described in Liske et al. (2015).

2.2. GAMA Photometry: Optical

Our analysis makes use of optical photometry for the determination of the sizes, inclinations, and morphologies of galaxies, as well as in determining their stellar masses. The GAMA optical photometry (u, g, r, i, z) is based on archival imaging data of SDSS.[26] As outlined in Driver et al. (2011) and detailed in Hill et al. (2011) and Kelvin et al. (2012), the archival imaging data are scaled to a common zero point on the AB magnitude system and convolved using a Gaussian kernel to obtain a common FWHM of the point-spread function of 2″. The resulting data frames are combined using the SWARP software developed by the TERAPIX group (Bertin et al. 2002), which performs background subtraction using the method described for SExtractor (Bertin & Arnouts 1996). From these "SWARPS" aperture-matched Kron photometry is extracted, as detailed in Hill et al. (2011), and Sérsic photometry is extracted by fitting the light profiles using single Sérsic profiles, as detailed in Kelvin et al. (2012). Along with the value of the fit profile integrated to 10 effective radii, the index of the profile n, the half-light angular size, and the ratio of semiminor to semimajor axis are also reported, together with quality control information regarding the fit.

Foreground extinction corrections in all optical bands have been calculated following Schlegel et al. (1998), and k-corrections to $z = 0$ have been calculated using kcorrect_v4.2 (Blanton & Roweis 2007).

2.3. GAMA Photometry: UV

Critical to our investigation is the use of space-borne spatially integrated UV photometry to measure SFR. Coverage of the GAMA fields in the ultraviolet (far-UV [FUV] and NUV) is provided by *GALEX* in the context of *GALEX* MIS (Martin et al. 2005; Morrissey et al. 2007) and by a dedicated guest investigator program *GALEX-GAMA*, providing a largely homogeneous coverage to ~23 mag. Details of the GAMA UV photometry are provided in Liske et al. (2015), in E. Andrae et al. (2017, in preparation), and on the *GALEX*-GAMA Web site.[27] In summary, extraction of UV photometry proceeds as follows. GAMA provides a total of three measurements of UV fluxes. First, all *GALEX* data are processed using the *GALEX* pipeline v7 to obtain a uniform blind source catalog[28] with a signal-to-noise ratio (S/N) cut at 2.5σ in the NUV. This catalog has subsequently been matched to the GAMA optical catalog using an advanced matching technique, which accounts for the possibility of multiple matches between optical and UV sources, redistributing flux between the matches as described in Andrae et al. and on the *GALEX*-GAMA Web site. Additionally, FUV and NUV photometry at the positions of all GAMA target galaxies is extracted using a curve-of-growth algorithm, as well as in apertures defined based on the measured size of the source in the r band. For one-to-one matches preference is given to the pipeline photometry, while for extended sources and multiple matches the curve-of-growth and aperture photometry is preferred, since it provides better deblending and better integrated fluxes in these cases.The resulting best estimates of the total FUV and NUV flux of the galaxy are reported as BEST_FLUX_NUV and BEST_FLUX_FUV, respectively, in the UV photometric catalog and used in the work presented.

Foreground extinction corrections and k-corrections have been applied as in the optical bands. In calculating foreground

[23] GAMA assigns each redshift determined from a spectrum a quality metric nQ, the details of which are described in Liske et al. (2015). Briefly, however, redshifts used for science purposes should fulfill $nQ \gtrsim 3$.

[24] In the equatorial regions.

[25] The r-band magnitude limit for the GAMA survey is defined as the SDSS Petrosian foreground extinction-corrected r-band magnitude.

[26] This is now being replaced by KiDS imaging.

[27] www.mpi-hd.mpg.de/galex-gama/

[28] The band-merged *GALEX* blind catalog is NUV-centric, i.e., FUV fluxes have been extracted in NUV-defined apertures, entailing that no cataloged source can be detected only in the FUV.

extinctions in the NUV we make use of $A_{\rm NUV} = 8.2\,E(B-V)$, as provided by Wyder et al. (2007).

3. Derived Physical Properties

Additionally, we make use of some of the more advanced data products of the GAMA survey. Notably, we have made use of the GAMA galaxy group catalog (Robotham et al. 2011), as well as the GAMA stellar mass measurements (Taylor et al. 2011), and have derived AGN classifications from the emission-line measurements and SFRs from the UV photometry. In the following we provide details on the derived physical properties used in our analysis.

3.1. The GAMA Galaxy Group Catalog G^{3}Cv5

In order to identify galaxies in groups and to characterize their environment, we make use of the GAMA Galaxy Group Catalog v5 (G^{3}Cv5; Robotham et al. 2011). Due to the multipass nature of the GAMA survey and the resulting high spectroscopic completeness even in dense regions, this unique galaxy group catalog extends the halo mass function down to the range of low-mass, low-multiplicity galaxy groups, providing measurements of the dynamical mass of the groups over the whole range in mass. The G^{3}Cv5 encompasses the GAMA I region, extending to a homogeneous depth of $r_{\rm AB} \lesssim 19.4$, and spans a large range in group multiplicity, i.e., the number of detected group members ($2 \leqslant N_{\rm FoF} \leqslant 264$), as well as an unprecedented range in estimated dynamical mass ($5 \cdot 10^{11}\,M_{\odot} \leqslant M_{\rm dyn} \leqslant 10^{15}\,M_{\odot}$). This catalog has been constructed using a friends-of-friends (FoF) algorithm to identify galaxy groups in $a/d - z$ space. The catalog contains 12,200 (4487) groups with two (three) or more members, totaling 37576 (22,150) of 93,325 possible galaxies, i.e., ~40% of all galaxies are grouped.

As discussed in Robotham et al. (2011), the most accurate recovery of the dynamical center of the group is obtained using the so-called iterative group center. Using this method, the center always coincides with a group member galaxy. For the purposes of our analysis, we have defined this galaxy as the central galaxy of the group, and we consider all other group member galaxies to be satellite galaxies. We note that Robotham et al. (2011) have calibrated the group finder on mock survey light cones, finding no bias in the recovery of groups and of the center of groups, respectively, as a function of larger-scale structure. Furthermore, Alpaslan et al. (2014) have shown that observed galaxy groups from the group catalog trace out a large-scale structure of filaments and tendrils in the GAMA survey volume, so that overall we hold our identification of central and satellite galaxies to be robust.

3.2. AGN Classification Based on Emission-line Measurements

In converting UV luminosity to SFR it is essential to ensure that the measured UV luminosity indeed originates from the star formation activity of the galaxy and is not dominated by emission from a central AGN. Accordingly, in this work we have made use of the GAMA emission-line database, as detailed in Hopkins et al. (2013), to identify AGNs. In order to classify a galaxy as hosting an AGN, we impose the requirement of line measurements with S/N > 3 in all four lines required for the BPT classification (Hα, NII, Hβ, and OIII) and that the galaxy lie in the AGN-dominated region of parameter space as defined by Kewley et al. (2001).

3.3. Stellar Mass Estimates

In order to control for the effect of intrinsic galaxy properties on the SFR of galaxies and separate this from environmental effects, we characterize our galaxy sample by stellar mass M_*, using the GAMA stellar mass estimates of Taylor et al. (2011), which are derived from the GAMA aperture-matched broad-band photometry.[29] We note that Taylor et al. (2011) make use of a Chabrier (2003) initial mass function (IMF) and the Bruzual & Charlot (2003) stellar population library, and that hence any systematic variations due to the choice of IMF or the stellar population library are not taken into account. Furthermore, stellar masses predicted by Taylor et al. incorporate a single fixed prediction of the reddening and attenuation due to dust derived from Calzetti et al. (2000). Thus, expected systematic variations in reddening and attenuation with inclination, disk opacity, and bulge-to-disk ratio are not taken into account in the determination of M_*. However, as discussed by Taylor et al. (see also Figures 2 and 15 of Driver et al. 2007), the resulting shifts in estimated stellar mass are much smaller than the individual effects on color and luminosity. Finally, as we have constructed a morphologically selected sample, we are largely robust against possible morphology-dependent biases in the stellar mass estimates arising from different stellar populations associated with different galaxy morphologies. Overall, Taylor et al. (2011) determine the formal random uncertainties on the derived stellar masses to be ~0.1–0.15 dex on average, and the precision of the determined mass-to-light ratios to be better than 0.1 dex.

3.4. Star Formation Rates

Making use of the SFRs of late-type galaxies as a tracer of their gas content and its dependence on the galaxies' environment requires a tracer that is sensitive to changes on timescales significantly shorter than the typical dynamical timescale of ~1 Gyr of galaxy groups. On the other hand, the tracer must reliably trace the spatially integrated star formation of the galaxy and be robust against individual bursts of star formation. As shown in Figure 1, which shows the spectral luminosity density of a galaxy as a function of wavelength for a range of times after the cessation of star formation, as well as the luminosity-weighted mean age as a function of wavelength for a galaxy with a constant SFR, the NUV emission ideally fulfills these requirements. Probing timescales of order 10^8 yr, it can resolve (in time) changes on the typical dynamical timescale of galaxy groups while being robust against individual stochastic bursts of star formation, unlike Hα emission line based tracers and to a lesser extent the FUV, which trace star formation on timescales of $\sim 10^7$ yr. Furthermore, the GAMA NUV photometry provides a robust estimate of the total spatially integrated NUV flux of the galaxy, and hence of the total SFR as desired, in contrast to emission-line-based tracers, which require more or less sizable aperture corrections due to the size of the fiber, depending on the distance of the source. Finally, the conversion of NUV luminosity to an SFR may depend on the age of the stellar population, i.e., the SFH, and on the metallicity. Using the spectral synthesis code Starburst99 (Leitherer et al. 2014), we find the derived SFR to vary by ≲10% over a range of

[29] Following E. N. Taylor (private communication), we scale the stellar mass estimates by the ratio of the Sérsic r-band magnitude to the Kron r-band magnitude to account for flux missed by the fixed aperture.

1.8 < Z < 0.05 (a large range compared to that expected based on the evolution of the average metallicity of star-forming galaxies over the redshift range 0 < z < 0.8 (Yuan et al. 2013), and between a constant SFH and a declining SFH following the star-forming main sequence (SFMS).

It is, however, essential to make use of the *intrinsic* NUV emission of the galaxies, i.e., to correct for the attenuation of the stellar emission due to the dust in the galaxy, which is particularly severe at short (UV) wavelengths (e.g., Tuffs et al. 2004).

In the context of the work presented here, it is important that these corrections be as precise and accurate as possible for two main reasons:

(i) With the analysis relying on the identification of systematic effects of the SFR and sSFR, all scatter in the values of $M_{\rm NUV}$ used in determining these quantities will reduce the sensitivity of the analysis.

(ii) In order to provide a quantitative analysis that can eventually be used in constraining structure formation calculations, an accurate treatment of systematic effects influencing the determination of intrinsic SFR is required.

For our purposes we have adopted the method of Grootes et al. (2013), which uses the radiation transfer model of Popescu et al. (2011) and supplies attenuation corrections on an object-by-object basis for spiral galaxies, taking into account the orientation of the galaxy in question and estimating the disk opacity from the stellar mass surface density. A recent quantitative comparison of this method with other methods of deriving attenuation corrections, including the UV slope, has shown it to have a higher fidelity, with smaller scatter and systematics in measuring SFR compared to other commonly used methods (see Figures 4 and 9 of Davies et al. 2016).

The geometry on which the RT model relies has been empirically calibrated on a sample of nearby edge-on spiral galaxies. Details of the derivation of attenuation corrections are provided in Appendix B. Corrections are typically ∼1.4 mag for high stellar mass galaxies ($M \gtrsim 10^{10.5} M_{\rm e}$) and lower (∼0.74 mag) for lower-mass galaxies ($M_* \gtrsim 10^{9.5} M_{\rm e}$). To illustrate the impact of the attenuation corrections, in Figure 2 we show the distribution of NUV absolute magnitudes for largely isolated spiral galaxies in two ranges of stellar mass ($10^{9.5} M_{\rm e} < M_* < 10^{9.8} M_{\rm e}$ and $10^{10.3} M_{\rm e} < M_* < 10^{10.6} M_{\rm e}$) drawn from our FIELDGALAXY sample (see Section 4.3 for a definition of the FIELDGALAXY sample) before (red) and after (blue) applying attenuation corrections to the observed NUV emission. The tail in the distribution due to dust for more edge-on systems is effectively removed. This tail would otherwise have been confused with galaxy quenching in a way not depending on the color of the galaxy.

Using the intrinsic absolute foreground extinction-corrected NUV magnitudes derived in this manner, we estimate the SFR Φ_* using the conversion given in Kennicutt (1998b) scaled from a Salpeter (1955) IMF to a Chabrier (2003) IMF as in Salim et al. (2007). For ease of comparison we explicitly supply our conversion from NUV luminosity to SFR in Equation (1). It is then also simple to derive the sSFR ψ_* following Equation (2):

$$\mathrm{F}_*[M_\odot\,\mathrm{yr}^{-1}] = \frac{L_{\rm NUV}\,[\mathrm{Js}^{-1}\,\mathrm{Hz}^{-1}]}{1.58 \times 7.14 \cdot 10^{20}}, \quad (1)$$

$$y_* = \mathrm{F}_* / M_* \quad . \quad (2)$$

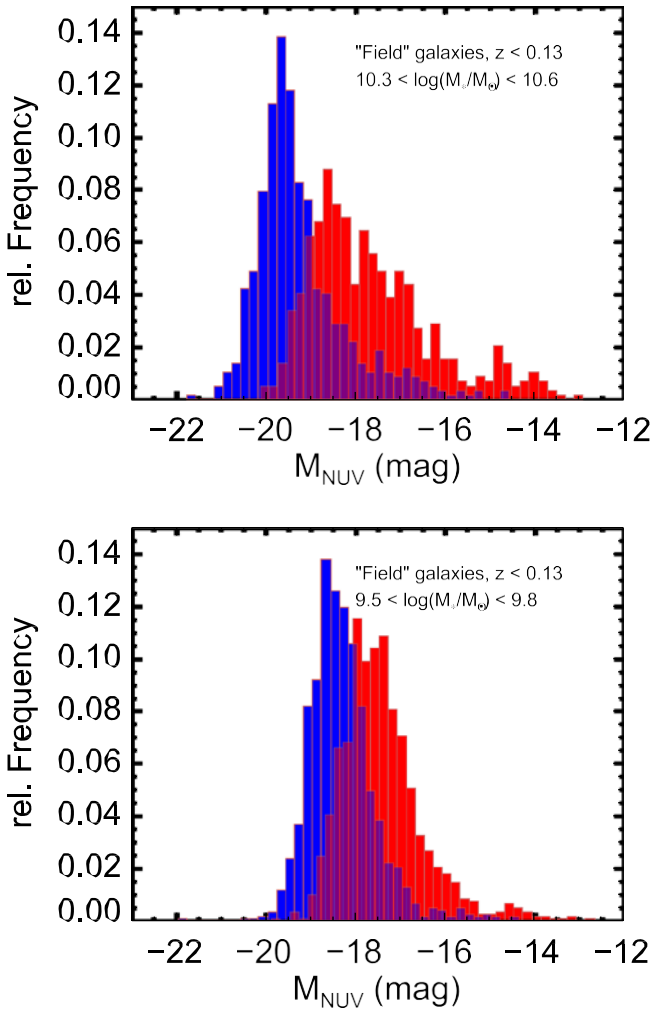

Figure 2. Distributions of NUV absolute magnitude $M_{\rm NUV}$ in two ranges of stellar mass before (red) and after (blue) applying attenuation corrections as prescribed by Grootes et al. (2013). Notice the reduction of the scatter and the removal of the tail toward faint values of $M_{\rm NUV}$, especially in the high stellar mass range.

4. Sample Selection

For our purpose of using disk-dominated/spiral galaxies as test particles to probe the influence of environment on the star formation and gas fueling of galaxies, we require a morphologically selected sample of spiral galaxies in galaxy groups. However, in order to separate environmental effects from the effects of secular evolution, we also require a morphologically selected sample of non-grouped spiral galaxies as a reference sample. For reasons of brevity we will refer to non-grouped galaxies as field galaxies. Additionally, as the probability of the morphological transformation of a galaxy may/will vary with environment, we require a well-defined uniform parent sample from which to select the morphologically defined samples for our analysis, which will allow us to quantify the evolution in the morphological fractions between different environments. Furthermore, these requirements entail that the sample must be of homogeneous depth, must have been observed by *GALEX*,[30] and must have available stellar mass measurements, as well as structural information in the form of Sérsic photometry. In the

[30] *GALEX* coverage of the GAMA equatorial footprint is high but not complete. See E. Andrae et al. (2017, in preparation) and Liske et al. (2015) for

details.

Table 1
Summary of Sample Selection Process

Sample	Criteria	No. of Gal.	No. of Groups
Parent sample	i–vi	16,791	2734
Spiral galaxies	See Section 4.2	7988	1861
FIELDGALAXY	See Section 4.3	5202	⋯
GROUPGALAXY	See Section 4.4	971	532
Satellites	See Section 4.5	892	502
Centrals	See Section 4.5	79	79

following, we describe the sample selection process, beginning with the definition of a uniform parent sample. A synoptic overview of the sample selection is provided in Table 1.

4.1. The Parent Sample

As the basis of our analysis we have constructed a uniform sample of galaxies from the GAMA database by selecting those that fulfill the following criteria:

(i) $r_{AB} < 19.4$;
(ii) science quality redshift available from the GAMA data set;
(iii) *GALEX* NUV coverage of the galaxy position, which is not affected by artifacts (deselection of window and dichroic reflection artifacts);
(iv) redshift $z > 0.13$;
(v) successful Sérsic profile photometry in the GAMA data set (r-band quality flag = 0);
(vi) GAMA stellar mass estimate with $M_* > 10^9 M_e$.

This results in a sample of 16,791 galaxies. Criteria (i) and (ii) ensure a balanced comparison of group and field galaxies by restricting the selection to the galaxies used in the construction of the galaxy group catalog G^{3}Cv5. This work makes use of NUV photometry in estimating SFR of galaxies and (criterion (iii)) ensures either that a source has been detected or that an upper limit can be derived. The redshift limit given by criterion (iv) ensures that the resolution of the imaging data is sufficient to allow reasonable determinations of galaxy morphology, while criterion (v) ensures that the necessary structural information for the morphological classification, as discussed in detail below, and the attenuation correction is indeed available. Finally, in combination criteria (i), (iv), and (vi) ensure that our sample selection is robust against the effects of cosmological surface brightness dimming over the volume considered.

As shown by Taylor et al. (see Figure 6 of Taylor et al. 2011), the GAMA survey (limited to $r_{AB} = 19.4$) in the redshift range of $z > 0.13$ is largely stellar mass complete, i.e., volume limited, to $M_* > 10^{9.5} M_e$ (>80% complete to $M_* > 10^{9.5} M_e$ at $z \approx 0.13$). Thus, choosing a stellar mass limit as specified in criterion (vi) in combination with criterion (iv) leads to a nearly volume-limited sample of galaxies. It must be noted, however, that below $M_* = 10^{9.5}$, the galaxy samples selected will suffer from a Malmquist bias toward blue galaxies. Quantitatively, for a mass of $M_* = 10^9 M_e$, the survey will only be largely mass complete to $z = 0.08$. By introducing a color bias to the galaxy population, the Malmquist bias affecting the stellar mass completeness of the GAMA survey at $M_* > 10^{9.5} M_e$ may also give rise to a bias in the SFR and ψ_* properties of the galaxy samples in that range of stellar mass. Nevertheless, in order to at least provide an indication of the behavior of galaxies with $M_* < 10^{9.5} M_e$, we extend our sample down to $M_* = 10^9 M_e$ and have taken the bias into account appropriately. A detailed quantification and discussion of the bias are provided in Sections 4.3, 4.4, and 5.

4.2. Selection of Disk/Spiral Galaxies

A key element in our approach is the selection of a morphologically defined pure sample of disk/spiral galaxies, unbiased in their SFR distribution. This requirement entails that no selection method that makes use of information linked to ongoing star formation activity (e.g., galaxy colors or clumpiness) can be used. For the purpose of selecting our sample we have therefore adopted the method of Grootes et al. (2014). This method, which has been trained using the GALAXY ZOO DR1 (Lintott et al. 2011), provides the user with a number of selection parameter combinations, some of which are optimized to recover samples with an unbiased SFR distribution.

In particular, we have chosen to use the parameter combination $(\log(n), \log(r_e), M_i)$, where n is the index of the single Sérsic profile fit to the galaxy in the r band, r_e is the r-band effective (half-light) radius, and M_i is the total i-band absolute magnitude. As shown in Grootes et al. (2014), this particular parameter combination selects ≈77%[31] of SDSS galaxies classified as spiral/disk galaxies in GALAXY ZOO DR1 (≈70% of visual spiral/disk galaxies extending to types S0/Sa based on the classifications of Nair & Abraham 2010), with a contamination of ≈2% by elliptical galaxies. Nevertheless, as demonstrated in Grootes et al. (2014), the use of this parameter combination results in samples that are representative of the SFR distribution of visual spiral/disk galaxies, as the recovered samples are largely unbiased with respect to the Hα equivalent width distribution (indicative of the sSFR distribution). We also find support for this representative recovery of the parent sSFR distribution when considering the $z < 0.06$ subsample of GAMA galaxies with visual morphological classifications presented in Kelvin et al. (2014). For these sources we find the overall distribution of SFR at fixed stellar mass to be statistically indistinguishable for a sample selected by our adopted proxy, as well as by the available visual classifications (even under the inclusion of S0/Sa galaxies).

Although the performance of the selection method has been demonstrated on the parent population of spiral/disk galaxies, the use in this work of galaxy samples differentiated by environment requires the consideration of a further difficulty. For a spiral galaxy consisting of a predominantly old[32] bulge component and a younger star-forming disk, a quenching of the star formation will lead to a secular passive fading of the disk with respect to the bulge, which might cause a spiral galaxy to be shifted out of the selection by changing the resulting value of n or r_e, although its actual morphology remains unaltered. Thus, although the recovery of the SFR distribution appears largely unbiased, the possibility of slight remaining bias against quenched systems remains. As the group environment may cause a cessation or decline of star formation in member galaxies, the possibility of the environment exacerbating the possible small bias induced by fading and impacting the

[31] As shown in Grootes et al. (2014), the rate of recovery decreases for very small and very bulge-dominated systems.
[32] In terms of its stellar population.

recovery of the group spiral/disk population arises. However, as we show in detail in Appendix A, even for the higher range of bulge-to-disk ratios represented by the higher stellar mass range of our samples (B/T ≈ 0.3) we only expect shifts of ∼0.1 over timescales of several gigayears, i.e., not out of the range of B/T values encompassed by the selection method of Grootes et al. (2014), so that passive fading will not significantly bias our sample selections.

In our analysis we have used the parameter combination (log(n), log(r_e), M_i) to provide a sample of morphologically late-type/disk galaxies. A detailed discussion of the morphological selection is provided in Appendix A. Applying the morphological selection to the sample of 16,791 galaxies previously selected, we obtain a sample of 7988 disk/spiral galaxies.

4.3. The Field Galaxy Sample

From the sample of disk/spiral galaxies we select a so-called "field" sample for reference purposes in this paper (and the following papers in this series) by selecting those galaxies that have not been grouped together with any other spectroscopic GAMA galaxy in the G^{3}Cv5 to the apparent magnitude limit of r_{AB} < 19.4 mag. Furthermore, we impose the requirement that the galaxy not host an AGN. This results in a sample of 5202 galaxies, referred to as the FIELDGALAXY sample. As a comparison, a total of 9606 galaxies from the parent sample are non-grouped in the G^{3}Cv5, and we refer to these as the field galaxy parent sample.

It should be emphasized that the FIELDGALAXY sample does not strictly represent a sample of truly isolated galaxies, as potentially galaxies below the magnitude limit may be associated with its constituent galaxies (i.e., rendering them grouped). However, given the stellar mass completeness of GAMA to $M_* \approx 10^{9.5}\,M_e$ at z = 0.13, as well as the high spectroscopic completeness achieved by the GAMA survey, it is nevertheless very likely that the FIELDGALAXY sample galaxies lie at the center of their DMH and are the dominant galaxy in it, as for normal mass-to-light ratios it is unlikely that they are actually the satellite of a more massive but r-band-faint galaxy. As such, the galaxies in the FIELDGALAXY sample can be thought of as representing a highly pure sample of largely isolated spiral central galaxies.

The fraction of the field galaxy parent sample included in the FIELDGALAXY sample, i.e., the field spiral fraction, varies as a function of stellar mass M_*, as shown in Figure 3. We find the spiral fraction to decrease from ∼65% at $M_* \approx 10^{9.5}\,M_e$ to ∼30% at $M_* \approx 10^{10.75}\,M_e$. In terms of frequency, the distribution of M_* for the FIELDGALAXY sample is peaked at the lower bound of the volume-limited mass range (see Figure 3), with the frequency gradually declining toward higher values of M_* and only ∼2% of the sample being more massive than $10^{10.75}\,M_e$.

Finally, the distributions of stellar mass M_*, SFR, and sSFR Ψ_* as a function of redshift z for the FIELDGALAXY sample are shown in Figure 4 and evidence the presence of the previously discussed Malmquist bias. Figures 3 and 4 also demonstrate that the *GALEX* NUV coverage is sufficiently deep so as to ensure that the median and quartiles of the distributions of SFR and sSFR are defined by actual detections, rather than by upper limits.

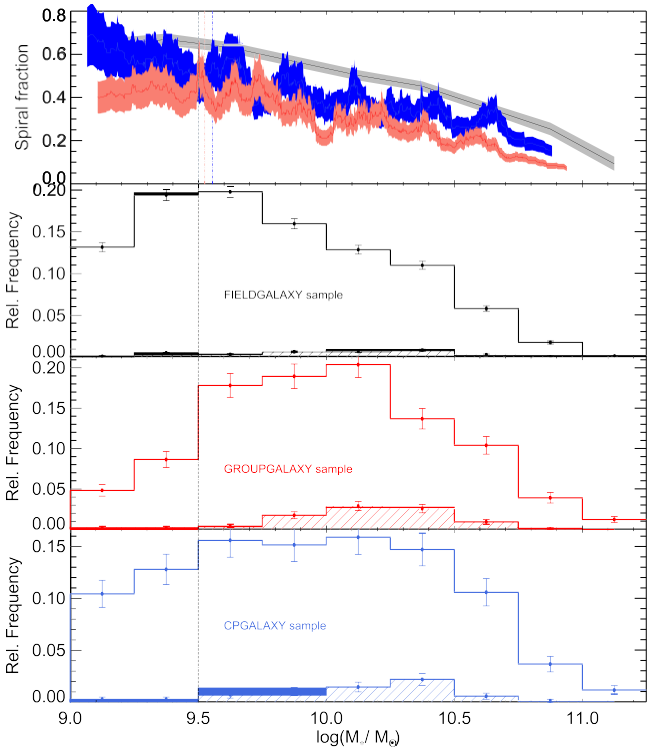

Figure 3. Spiral fraction (i.e., fractional contribution of the spiral sample in question to the relevant parent sample) for the FIELDGALAXY, GROUPGALAXY, and CPGALAXY samples in sliding top-hat bins containing 40 galaxies, as detailed in Section 6. The shaded area indicates the (Poisson) uncertainty in each bin. Colored dot-dashed lines indicate the stellar mass above which the bins can be considered to be complete. The lower panels show the distribution of stellar mass M_* for the FIELDGALAXY, GROUPGALAXY, and CPGALAXY samples. Hatched histograms show the stellar mass distributions of sources with NUV upper limits. The spiral fraction as a function of stellar mass and the stellar mass distributions are available online as "data behind the figure." The data used to create this figure are available.

4.4. The Group Galaxy Sample

The sample of field spiral galaxies is complemented by our sample of spiral/disk-dominated galaxies within galaxy groups as characterized by the G^{3}Cv5 of Robotham et al. (2011) (see also Section 3), referred to as the GROUPGALAXY sample. In constructing this sample, we proceed by selecting from the sample of 7988 disk/spiral galaxies all those that are assigned to a group with three or more members (of any morphology), each with $M_* > 10^{9.5}\,M_e$. This selection ensures that the groups considered in our analysis can be selected over the full redshift range considered, thus avoiding any implicit bias in Ψ_* as a function of group properties, which could result from the Malmquist bias in the galaxy sample. Obviously, groups selected in this manner thus may actually consist of more members, some having $M_* < 10^{9.5}\,M_e$, due to the flux-limited nature of the GAMA survey.

From this selection, we discard all galaxies residing in groups in which the velocity dispersion is dominated by the total error on the velocity dispersion,[33] and we furthermore impose the requirement that the galaxy not host an AGN.

[33] As discussed in Robotham et al. (2011), no estimate of the dynamical mass is possible in groups in which the total error on the velocity dispersion, composed of the uncertainties on the individual redshifts, is comparable to the measured velocity dispersion.

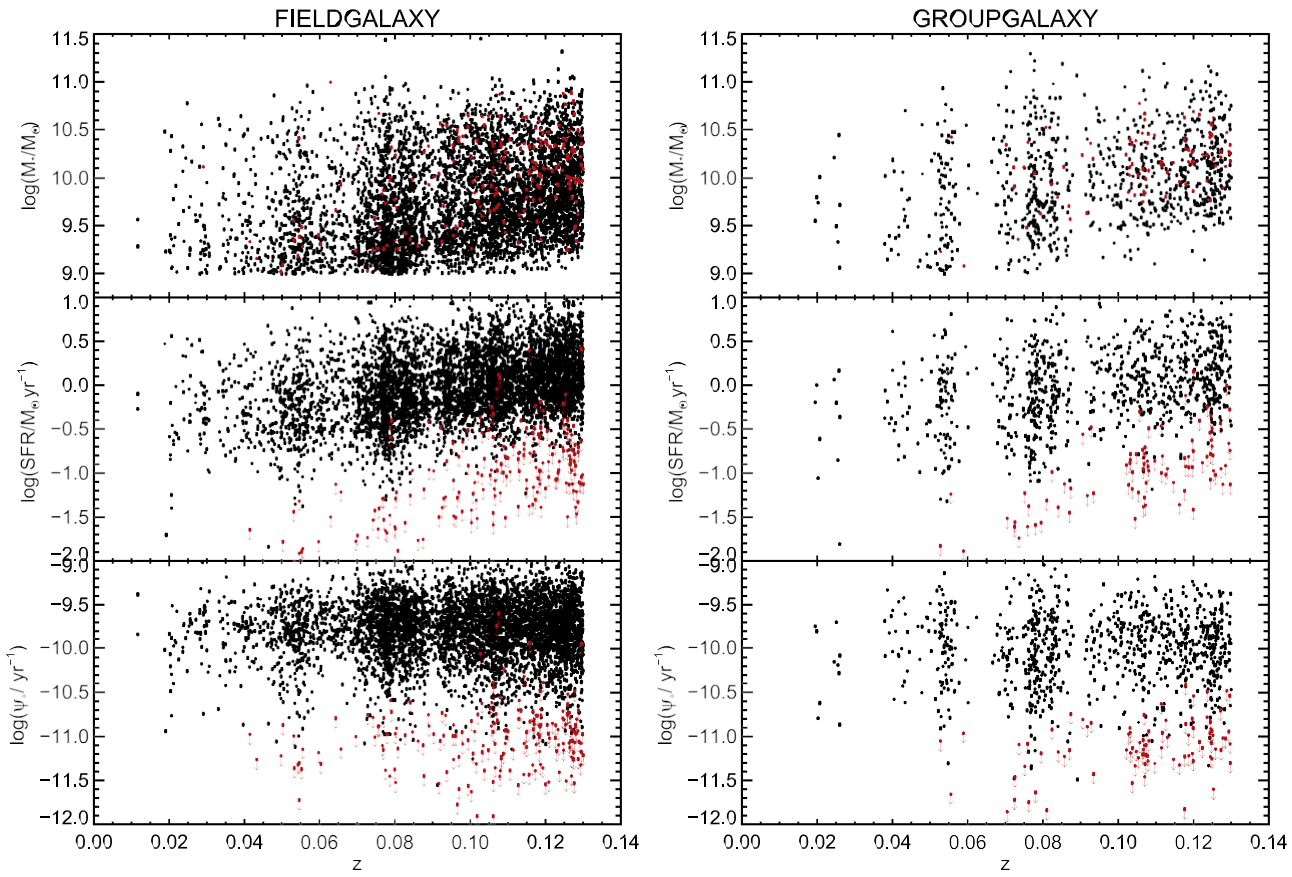

Figure 4. Distributions of stellar mass $M*$ (top), SFR (middle), and sSFR ψ* (bottom), as a function of redshift z for the FIELDGALAXY sample (left) and the GROUPGALAXY sample (right). Galaxies for which only 2.5σ upper limits in the NUV are available are shown in red. The effects of the Malmquist bias on the population of galaxies with $M* < 10^{9.5}$ are clearly visible. Above this mass no indication of a bias is present. The vast majority of sources are detected by *GALEX* in the NUV, ensuring that the median and quartiles of the distributions are defined by detections rather than upper limits.

In using the galaxies in our samples as test particles and their SFR as a probe of gas fueling, it is essential to exclude close pairs of galaxies, as the effects of galaxy–galaxy interactions are known to boost the rate at which galaxies convert their ISM into stars (e.g., Barton et al. 2000; Robotham et al. 2013; Davies et al. 2015). Although these galaxy–galaxy interactions, which are likely to be present in close pairs, are an important and interesting aspect of galaxy evolution in the group environment, they will be superimposed on the galaxy–IHM effects, which are the focus of this work. We therefore discard galaxies that are a member of a close pair, i.e., have a neighbor galaxy within 1000 km s^{-1} and a projected separation $\square 50\,\mathrm{kpc}\,h^{-1}$.

To verify that the minimal separation chosen in the exclusion of close pairs of galaxies is sufficient to isolate galaxy–IHM interactions from galaxy–galaxy interactions, we consider the offset of the sSFR ψ* of the galaxies in the GROUPGALAXY sample from the median value of ψ* for FIELDGALAXY sample galaxies of the same mass, Δlog(ψ*) as defined in Equation (3) of Section 6, as a function of stellar mass $M*$, and of the projected distance to the nearest group member galaxy $r_{\mathrm{proj,NN}}$, as shown in Figure 5. No systematic dependence of Δlog(ψ*) on $r_{\mathrm{proj,NN}}$ is visible for $r_{\mathrm{proj,NN}} \square 50\,\mathrm{kpc}\,h^{-1}$, implying that environmental effects on ψ* as a function of group parameters are unlikely to be contaminated by the effects of recent interactions. For galaxies within our exclusion limit, we do see signs of an enhanced star formation at low projected distances, in particular for $M* \square 10^{10}\,M_{\mathrm{e}}$, in line with the results of the dedicated investigation of star formation in close pairs presented by Davies et al. (2015).

Applying this selection, the resulting GROUPGALAXY sample consists of 971 galaxies drawn from 532 distinct galaxy groups as identified by the G^{3}Cv5. As a comparison, a total of 4419 galaxies from the parent sample reside in galaxy groups with three or more members (this number includes close pair galaxies, as well as AGN host galaxies). We refer to these galaxies as the group galaxy parent sample.

In terms of the spiral fraction as a function of stellar mass for group galaxies, we find that the trend found for the FIELDGALAXY sample is approximately mirrored by the GROUPGALAXY sample over the full range in $M*$. However, the actual fraction of spiral galaxies embodied by the GROUPGALAXY sample is lower by 30%–40% over the entire range in $M*$ considered. Furthermore, the distribution of $M*$ for the GROUPGALAXY sample, as shown in Figure 3, is more skewed toward intermediate- and higher-mass galaxies than that of the FIELDGALAXY sample, displaying a peak in the relative frequency distribution at $M* \approx 10^{10}$–$10^{10.25}\,M_{\mathrm{e}}$ and increased relative weight above this stellar mass with respect to the FIELDGALAXY sample. This increase in relative weight can be attributed to the requirement that a group contain $\square 3$ galaxies with $M* \square 10^{9.5}\,M_{\mathrm{e}}$ in order to enter the GROUPGALAXY sample, leading to a selection of more massive halos than those sampled by the largely isolated central galaxies of the

FIELDGALAXY sample. These relatively more massive halos can and do host relatively more massive galaxies, skewing the stellar mass distribution.

Finally, as for the FIELDGALAXY sample, the distributions of $M*$, SFR, and sSFR for the GROUPGALAXY sample are depicted in Figure 4 and show evidence of the expected Malmquist bias below $M = 10^{9.5} M_e$.

4.5. Group Central and Satellite Spiral Galaxies

As outlined in the introduction, the distinction between a galaxy being a central or a satellite galaxy may be fundamental to its SFR and SFH. For the purpose of our detailed investigation of the impact of the group environment on the SFR of spiral/disk galaxies, we further divide the GROUPGALAXY sample into satellite and central spiral group galaxies, which we will refer to as satellites and centrals, respectively. This distinction is based on the identification of the group central galaxy supplied by the G^{3}Cv5.

In total, we find 892 group satellite spiral galaxies and 79 group central spiral galaxies. The spiral fractions of the satellites and centrals[34] as a function of $M*$ are shown in Figure 6. With the satellites constituting ∼91% of the GROUPGALAXY sample, the spiral fraction of the satellites unsurprisingly mirrors that of the GROUPGALAXY sample in both trend and absolute values. However, we find not only that the spiral fraction of the centrals also displays the same trend with stellar mass as the satellites and the FIELDGALAXY sample, but also that the actual spiral fraction of centrals is comparable to that of satellites over the full mutual mass range, i.e., 30%–40% suppressed with respect to the FIELDGALAXY sample.

Figure 6 also shows the distributions of $M*$ for the group satellite and group central spiral galaxies. As for the GROUPGALAXY sample, the sample of satellite spiral galaxies is more skewed toward intermediate values of stellar mass with respect to the FIELDGALAXY sample (see the second panel from the top in Figure 6), with the distribution of $M*$ peaking at $M* = 10^{10}$–$10^{10.25} M_e$, as shown in the third panel from the top in Figure 6. The relative frequencies of the satellites and the GROUPGALAXY sample agree within their uncertainties, although the satellites appear slightly more weighted toward lower values of $M*$ (see Figures 3 and 6), as expected given the distribution of $M*$ for centrals (see bottom panel of Figure 6). The latter, namely, is skewed toward high-mass galaxies, with the distribution of $M*$ for the sample of centrals peaking at $M* = 10^{10.5}$–$10^{10.75} M_e$.

4.6. The Close Pair and Merging Galaxy Samples

We have constructed our FIELDGALAXY and GROUPGALAXY samples to exclude close pairs of galaxies, defined as being grouped with Δv □ 1000 km s^{-1} and a projected separation less than $50 h^{-1}$ kpc, and merging galaxies, in order to safeguard against contamination by the effects of galaxy–galaxy interactions on the SFR of our sample galaxies. To qualitatively understand whether this exclusion is necessary/justified, we have constructed a sample of close pair galaxies, referred to as the CPGALAXY sample, which meet all the morphological and photometric requirements of the

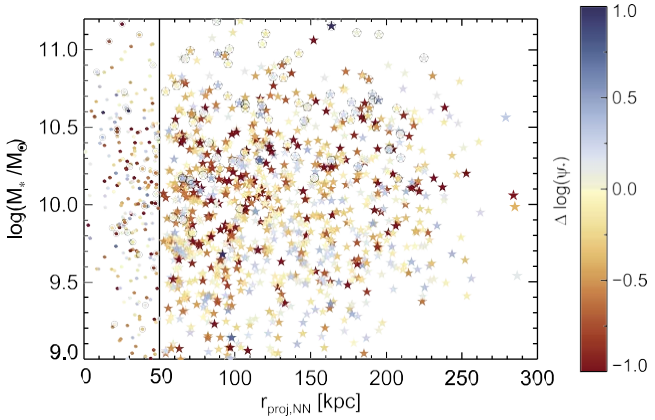

Figure 5. $M*$ as a function of the projected distance to the nearest group neighbor, $r_{proj,NN}$. Galaxies in the GROUPGALAXY sample are shown as stars, with galaxies that are the central galaxy of their respective group marked by a circle. The offset from the median value of ψ* for field sample galaxies of the same stellar mass as the satellite (Δlog(ψ*)) is color-coded from blue (enhanced) to red (suppressed), as shown in the figure. The vertical solid black line indicates the minimum projected separation required for inclusion in the GROUPGALAXY sample. Galaxies that would have been included in the GROUPGALAXY sample save for having a (group member) neighbor within $50 h^{-1}$ kpc are shown as colored filled circles, with centrals again indicated by black circles.

GROUPGALAXY sample (including not hosting an AGN) but are a member of a close pair of galaxies.[35] In total, this CPGALAXY sample contains 680 galaxies. Of these, 50 have been visually classified as merging galaxies. We have removed these from the CPGALAXY sample and designate these 50 galaxies to be the MERGER sample. At this point we emphasize that for these samples derived properties such as SFR may suffer from systematic physical effects, impacting our ability to recover intrinsic SFR. The purpose of these samples is solely to gain a qualitative measure of the potential impact of galaxy–galaxy interactions on the SFR of spiral galaxies.

In terms of the distribution of stellar mass and the spiral fraction of the CPGALAXY sample, Figure 3 shows that the CPGALAXY sample is more skewed toward intermediate and high stellar masses than the FIELDGALAXY sample, similar to the GROUPGALAXY sample. However, the peak at intermediate values of $M*$ is less pronounced. While the spiral fraction of the CPGALAXY sample also approximately mirrors the trend with stellar mass found for the FIELDGALAXY and GROUPGALAXY samples, in terms of the actual fraction of spirals, at a given stellar mass the CPGALAXY sample fraction lies between the FIELDGALAXY and GROUPGALAXY samples, being lower than that of the FIELDGALAXY by 10%–30% over the full range in $M*$. These trends are in line with expectations, given the CPGALAXY being composed of galaxies in groups, as well as in very low multiplicity systems.

4.7. Selection of Groups

No explicit selection of the galaxy groups on the basis of group properties has been made in this analysis. Instead, groups and their member galaxies have been included by virtue of their hosting a spiral/disk-dominated galaxy of the GROUPGALAXY sample as detailed in Section 4.4, with the only requirement being that the group consist of at least three member galaxies,

[34] Spiral fractions for centrals and satellites are defined as the fraction of group central/satellite galaxies in the relevant parent sample that are in the central/satellite subsample of the GROUPGALAXY sample.

[35] Unlike for the GROUPGALAXY sample, no requirement on the multiplicity of the group has been applied, i.e., galaxies in groups of two galaxies have been included.

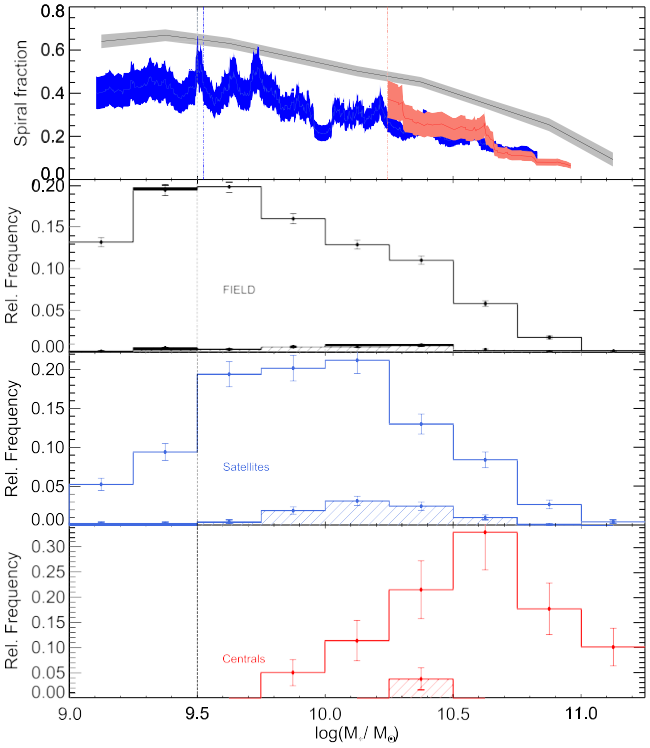

Figure 6. Top panel: fraction of galaxies classified as spirals as a function of M_* for the FIELDGALAXY sample (black), the satellite galaxies in the GROUPGALAXY sample (blue), and the central galaxies in the GROUPGALAXY sample (red). Fractions have been determined in the sliding top-hat bins containing 40 and 25 galaxies in the case of the satellites and centrals, respectively, as described in Section 6. The shaded areas indicate the (Poisson) uncertainties. The dot-dashed colored lines indicate the mass above which the population of the top-hat bin can be considered mass complete. The bottom panels show the distribution of M_* for each galaxy category, with the distribution of the sources with upper limits in ψ_* shown as a hatched histogram. The dotted vertical gray line indicates the mass limit beyond which the samples considered represent a volume-limited sample. The spiral fraction as a function of stellar mass and the stellar mass distributions are available online as "data behind the figure." The data used to create this figure are available.

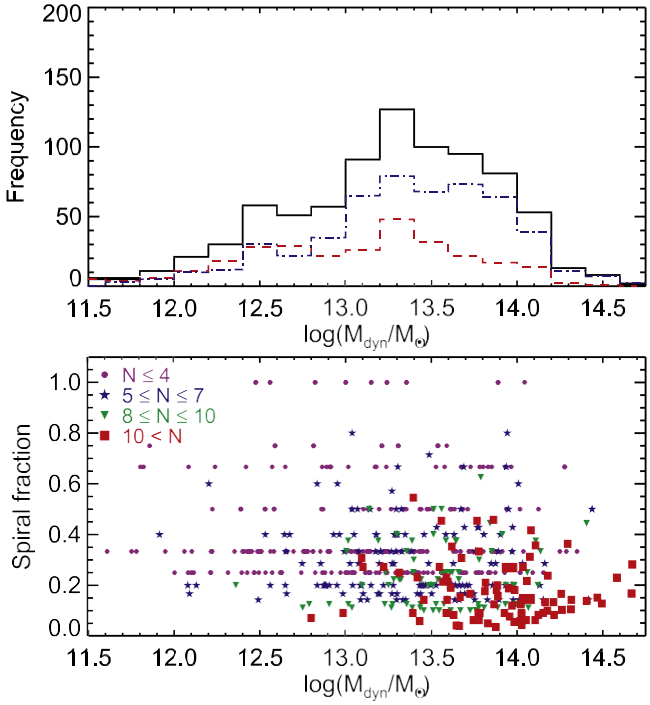

Figure 7. Top: distribution of the estimated dynamical mass of the galaxy group M_{dyn} as provided by the G^{3}Cv5 for all 824 galaxy groups with ≥ 3 member galaxies with $M_* \geq 10^{9.5} M_e$ and science quality redshifts for which an estimate of the dynamical mass is possible (black solid line). The distribution of M_{dyn} for the 532 groups sampled by the GROUPGALAXY sample (i.e., containing a spiral) is shown in blue, while that of the 292 groups not sampled (i.e., not containing a spiral galaxy) is shown in red. Bottom: spiral fraction (i.e., fraction of group members in the GROUPGALAXY sample) as a function of M_{dyn} for the galaxy groups sampled by the GROUPGALAXY sample. The number of group members is encoded in the color and plotting symbol used (purple circle: $N \leq 4$; blue star: $5 \leq N \leq 7$; green inverted triangle: $8 \leq N \leq 10$; red square: $N > 10$).

each with $M_* \geq 10^{9.5} M_e$, in order to guarantee that the sample of groups be volume limited.

Inside of $z = 0.13$ the G^{3}Cv5 contains 824 galaxy groups for which an estimate of the dynamical mass is possible and that consist of at least three member galaxies (of any morphology), each with $M_* \geq 10^{9.5} M_e$ and science quality redshifts. Of these, a total of 631 groups (77%) contain at least one spiral galaxy. In 99 of these the (only) spiral galaxy is a member of a close pair, resulting in a total of 532 (65%) of all possible galaxy groups being probed by the GROUPGALAXY sample. Although Grootes et al. (2014) cite a completeness of ~70% for the morphological selection criteria we have adopted, and it is accordingly possible that some of the groups not sampled by the GROUPGALAXY sample do in fact contain a spiral galaxy (in addition to those in which the spiral is in a close pair), it is nevertheless conceivable that the selection applied to define the GROUPGALAXY sample (in particular the morphological selection) might introduce a bias into the population of galaxy groups considered. In the following we will briefly consider potential biases in the distribution of group parameters of groups included in the GROUPGALAXY sample, compared to the full volume-limited sample of galaxy groups.

The top panel of Figure 7 shows the distribution of group dynamical mass for all 824 groups (black), as well as for the 532 (blue) and 292 (red) groups probed and not probed, respectively, by the GROUPGALAXY sample (top panel), while the bottom depicts the fraction of group member galaxies that are spirals as a function of the dynamical mass of the group (for the 532 groups probed by the GROUPGALAXY sample). We find the distribution of group dynamical mass for groups sampled by the GROUPGALAXY sample to be skewed toward more massive groups than that of the groups without a spiral galaxy. This, however, results from the fact that although the average spiral fraction decreases with group mass, the multiplicity increases. This increase in multiplicity is more rapid than the decrease in the spiral fraction, so that higher-mass groups are slightly more likely to host at least one spiral galaxy and thus be included in the GROUPGALAXY sample. Any bias toward higher mass, however, is mild, and the selection of the GROUPGALAXY sample does not appear to introduce any significant bias into the population of groups considered in our analysis.

5. The sSFR–M_* Relation for Field Spiral Galaxies

It is well documented that the main observationally accessible property influencing the sSFR of a galaxy is its stellar mass M_* (Noeske et al. 2007; Peng et al. 2010; Whitaker

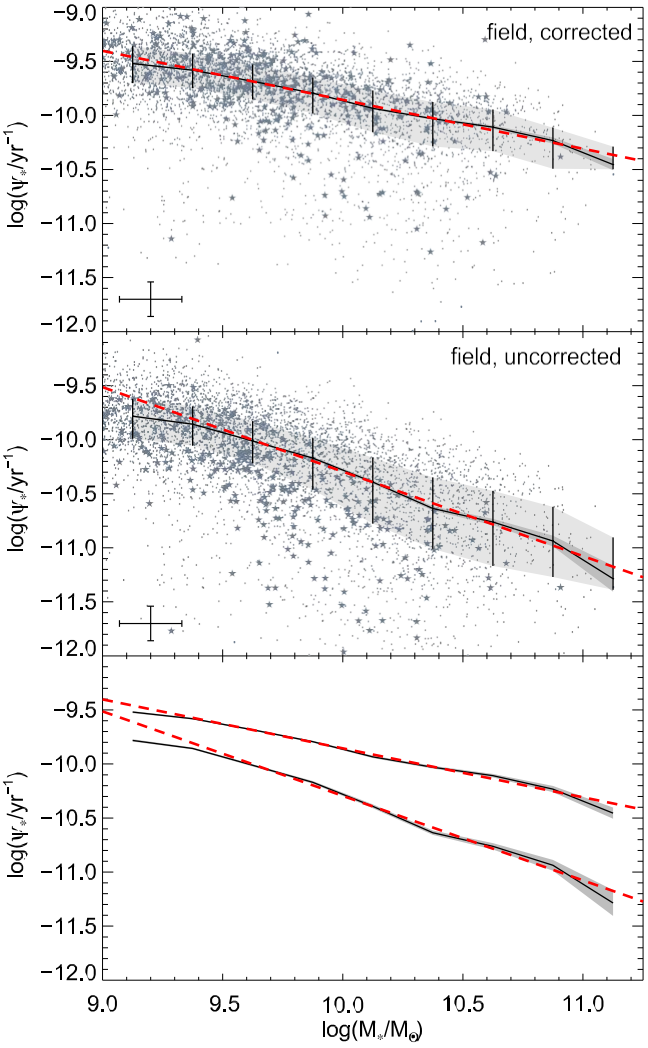

Figure 8. $\psi*$ as a function of $M*$ for the FIELDGALAXY sample, before (middle) and after (top) application of attenuation corrections. The median of the distribution in bins of 0.25 dex in $M*$ is shown as a solid line, with the error bars and the light-gray shaded region indicating the interquartile range and the uncertainty in the median (estimated by bootstrapping) shown as a gray shaded region. Median measurement uncertainties are shown at bottom left. The red dashed lines indicate single power-law fits to the binwise median values of $\psi*$ in the range of $M* > 10^{9.5}\,M_{\odot}$. The 5% most inclined galaxies are denoted by stars. A comparison of the corrected and uncorrected sSFR of these galaxies shows that a significant fraction of red galaxies actually have normal sSFRs. For ease of comparison the bottom panel shows both the corrected and uncorrected median relations, as well as the corresponding fitted power laws. The corrected and uncorrected FIELDGALAXY $\psi*$–$M*$ relations, including interquartile range and uncertainty of the median, are available online as "data behind the figure." The data used to create this figure are available.

et al. 2012). Therefore, in aiming to identify the influence of environmental effects on the sSFR of a galaxy, we require a means of accounting for this dependence and separating out the effects of the environment from galaxy-specific effects. Here, we make use of the relation between the sSFR $\psi*$ and the stellar mass $M*$ for spiral/disk-dominated galaxies thought to be free of major environmental influences, i.e., the largely isolated central spiral galaxies of our FIELDGALAXY sample, as shown in Figure 8, as a baseline from which to identify environmental effects.

Figure 8 also clearly reiterates the need to make use of the *intrinsic* (i.e., corrected for the affects of attenuation by dust) $\psi*$–$M*$ relation, as a comparison of the corrected and uncorrected relation shows that attenuation due to dust both significantly increases the scatter[36] (0.53 dex versus 0.36 dex for the intrinsic relation) and changes the (high stellar mass) slope of the relation. Furthermore, Figure 8 (and also Figure 10 below), in which the 5% most inclined galaxies in each mass bin have been highlighted, demonstrates the importance of accounting for the inclination of the galaxy as discussed in Section 3.4, as it is apparent that a significant fraction of the apparently red high-mass galaxies are highly inclined and actually have "normal" sSFRs.

Applying the attenuation corrections obtained using the method of Grootes et al. (2013) (as detailed in Appendix B), we find the intrinsic $\psi*$–$M*$ relation for the spiral/disk galaxies of the FIELDGALAXY sample to be well described by a power law $\psi_* \propto M_*^{\gamma}$ with a slope of $\gamma = -0.45 \pm 0.01$ over the entire range of $9.0 \leq \log(M_*/M_{\odot}) \leq 11.25$. The values of scatter and the coefficients of the power-law fits before and after applying attenuation corrections are compiled in Table 2. Because of the morphological selection, which makes no use of any parameters linked directly to star formation, the relation presented here represents a real unbiased specification of the $\psi*$–$M*$ relation for spiral/disk galaxies in the field, including spiral galaxies with little or no star formation. We note that this consideration of morphologically selected spirals, rather than a star-formation-driven selection, leads to our derived slope being considerably steeper than that found by Peng et al. (2010) (who selected visibly blue galaxies) and comparable to that of, e.g., Whitaker et al. (2012), who used a more encompassing selection of star-forming systems. We refer the reader to Grootes et al. (2014) for a more detailed discussion.

It is quite likely that much of the remaining scatter may be intrinsic and not due to dust, as the accuracy of the systematic dust corrections is supported by the reduction in scatter. Furthermore, we draw attention to the fact that although the scatter in the $\psi*$–$M*$ plane is reduced, due to the rarefication of the population of galaxies with low values of sSFR after the application of the attenuation corrections, a population of quiescent galaxies with very low sSFRs remains. These quiescent galaxies are predominantly of intermediate and high stellar mass, as can be seen from a comparison of the middle and top panels of Figure 8. Accordingly, as we have considered largely isolated central spiral galaxies, this result may imply the existence of a secular shutoff mechanism for star formation in spirals in isolated halos, linked only to the properties of the galaxy and its surrounding IHM.

5.1. *Quantification of the Malmquist Bias for Low-mass Galaxies*

While our samples of spiral galaxies, i.e., the FIELDGALAXY and GROUPGALAXY sample, are volume limited at $M* \geq 10^{9.5}\,M_{\odot}$, below this mass, driven by the relation between galaxy color and the mass-to-light ratio, the distribution of galaxy colors, and hence sSFR, may be subject to Malmquist bias, biasing the distributions toward bluer colors and higher sSFR. To quantify the impact this bias may have below the mass completeness limit of $M* \geq 10^{9.5}\,M_{\odot}$, and to verify that there is indeed no bias at greater stellar masses, we consider the FIELDGALAXY sample, split into a local

[36] All measurements of scatter were calculated as the difference between the quartiles of the distribution in $\psi*$, averaged over equal-sized bins in $M*$ of 0.25 dex in width, and weighted by the number of galaxies in each bin.

Table 2

Compilation of Power-law Fits to the y_*–M_* Relation

Sample	(Un)corrected (u/c)	Scatter (dex)	1σ Equiv. (dex)[a]	γ	A	Sections
FIELDGALAXY	u	0.53	0.39	−0.78 ± 0.02	−10.30 ± 0.03	5
FIELDGALAXY	c	0.36	0.27	−0.45 ± 0.01	−9.86 ± 0.02	5
FIELDGALAXY (z < 0.06)	c	0.35	0.26	−0.42 ± 0.06	−9.94 ± 0.03	5
FIELDGALAXY (z > 0.06)	c	0.36	0.27	−0.45 ± 0.01	−9.85 ± 0.02	5
GROUPGALAXY	u	0.77	0.57	−0.74 ± 0.04	−10.44 ± 0.02	6
GROUPGALAXY	c	0.59	0.44	−0.43 ± 0.03	−9.99 ± 0.02	6

Note. Power-law fits of the form $\log(y_*) = A + g \cdot (\log(M_*) - 10)$ to the y_*–M_* relations for different samples of spiral galaxies. The column "(Un)corrected" signifies whether attenuation corrections have been applied (c) or not (u). Scatter is calculated as detailed in Section 5. The uncertainties reflect the formal uncertainties of the fit.

[a] The weighted mean interquartile range is converted to an equivalent 1σ scatter under the assumption of a Gaussian distribution.

and distant sample at $z = 0.06$ as shown in Figure 9. Considering the median sSFR for subsamples of the local and distant samples with $10^9\,M_e \lesssim M_* \lesssim 10^{9.5}\,M_e$, we find that in the local sample it is ∼0.16 dex lower, and the interquartile range is ∼0.05 dex smaller, than in the distant sample. A similar consideration of the local and distant subsamples of the FIELDGALAXY sample limited to $10^{10}\,M_e \lesssim M_* \lesssim 10^{10.5}\,M_e$, and thus expected to be complete for both redshift ranges, displays a shift of ∼0.06 dex toward lower values for the low-z sample, with similar interquartile ranges (∼0.4 dex) in both samples. Fitting power laws to the local and distant subsample in the range $M_* > 10^{9.5}\,M_e$ (see Table 2), we find the fit to the local sample to be offset toward lower sSFR by 0.07–0.1 dex with respect to the fit to the distant sample, while the slopes agree within their uncertainties. We will discuss this shift in the context of the evolution of the main sequence of star-forming galaxies in Section 5.2.1. The additional shift of ≈0.09 dex in the low-mass range, however, can thus be attributed to the Malmquist bias affecting the sample below $M_* = 10^{9.5}\,M_e$.

We complement this test by comparing the distribution of the intrinsic $g - i$ color, derived by Taylor et al. (2011) in parallel to the stellar mass estimates and based on stellar population synthesis modeling, for the local and distant subsamples of the FIELDGALAXY sample using a Kolmogorov–Smirnov test. The distributions of the $g - i$ color are considered in a sliding bin of 0.2 dex in M_*. While the distributions in the bins up to and including $10^{9.3}\,M_e \lesssim M_* \lesssim 10^{9.5}\,M_e$ are statistically consistent with having been drawn from different parent distributions at above the 95% confidence level ($p \approx 0.01$), the higher-mass bins show no statistical evidence of having been drawn from different parent distributions $p \approx 0.545$.

We have applied analogous tests to the GROUPGALAXY sample using the same subsample definitions and find shifts of 0.1 and 0.05 dex toward lower values of ψ_* for the local subsamples in the low- and high-mass ranges, respectively. For the range $10^9\,M_e \lesssim M_* \lesssim 10^{9.5}\,M_e$ the null hypothesis that the $g - i$ color distributions have been drawn from the same subsample can be (marginally) rejected ($p = 0.042$), while for the high-mass bin there is no significant evidence of the $g - i$ distributions having been drawn from statistically different parent samples ($p = 0.52$).

Overall, these results imply that, as expected, the galaxy samples suffer from a mild bias toward blue, star-forming galaxies below $M_* = 10^{9.5}\,M_e$, with a systematic upward bias of ≈0.06 dex in the median sSFR of these objects, but that above this mass the samples are indeed complete and volume limited.

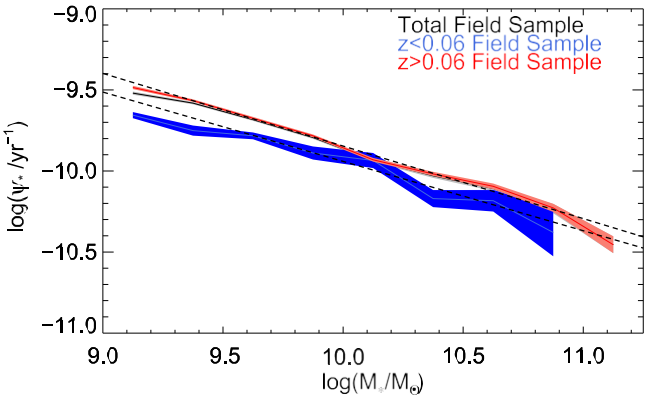

Figure 9. ψ_* as a function of M_* for the FIELDGALAXY sample (gray) and the local (blue) and distant (red) subsamples. The median of the distribution in bins of 0.25 dex in M_* is shown as a solid line, with the shaded region indicating the bootstrapped uncertainty in the median. The power-law fits tabulated in Table 2 are plotted as black dashed lines.

5.2. The y_*–M_* Relation for Spiral Galaxies versus the Main Sequence of Star-forming Galaxies

The ψ_*–M_* relation for spiral/disk-dominated galaxies considered here is closely related to the well-established so-called main sequence of star-forming galaxies (SFMS; e.g., Noeske et al. 2007; Peng et al. 2010; Whitaker et al. 2012). As shown by Wuyts et al. (2011), out to $z \approx 2.5$ the locus of star-forming galaxies in the SFR–M_* plane, commonly referred to as the SFMS, is dominated by galaxies whose light profiles can be well described by an exponential disk with a Sérsic index of ∼1. As such, as the majority of our spiral galaxies are star-forming (although we observe a non-negligible population of quiescent spirals), the ψ_*–M_* relation for spiral galaxies is likely to form the dominant backbone of the SFMS, at least in the local universe. In turn, this implies that the ψ_*–M_* relation for spirals, which may arguably be more constrained in terms of the physical drivers (Grootes et al. 2014), may be used to gain insight into the physical drivers of the SFMS. Here we briefly touch on two such uses.

5.2.1. Redshift Evolution

In our above consideration of the Malmquist bias affecting our sample we have split the FIELDGALAXY sample into two redshift ranges ($0 < z \lesssim 0.06$ and $0.06 < z \lesssim 0.13$). For the stellar mass range $M_* > 10^{9.5}\,M_e$, i.e., not affected by the Malmquist bias, we have found the normalization of the

relation to shift by ∼0.1 dex, while the slopes of the power-law fits in both redshift ranges agree within uncertainties. This shift can be attributed to a real evolution of the $\psi*$–$M*$ relation over this small redshift baseline. Comparing these results with the recently published fit of the redshift evolution of the SFMS provided by Speagle et al. (2014), we find the shift of ∼0.1 dex to be in line with the evolution predicted for the SFMS over this redshift baseline.[37] As the evolution over the small redshift baseline for the isolated central spirals of our sample can only readily be attributed to a smooth evolution of the available amount of fuel for star formation, this lends support to the idea (e.g., Kereš et al. 2005; Davé et al. 2011; Lilly et al. 2013; Saintonge et al. 2013) that the smooth evolution of the SFMS over much longer redshift baselines, as observed by Speagle et al., is also driven by gas supply processes. In this context we will consider the gas fueling of central spiral galaxies in more detail in a subsequent paper in this series.

5.2.2. Impact of Galaxy Morphology on the SFMS

Over the past decade, the SFMS has generally been considered to be well described by a single power law with a fixed slope and a normalization evolving with redshift (Noeske et al. 2007; Peng et al. 2010). However, more recently, a number of authors have found that at the high stellar mass end, the slope of the SFMS appears to flatten (Karim et al. 2011; Whitaker et al. 2012; Lee et al. 2015; Schreiber et al. 2015; Erfanianfar et al. 2016). This break, located at $M* \sim 10^{10}$–$10^{10.5}\,M_e$, is generally attributed to the increasing contribution of a passive bulge component to the stellar mass of a galaxy (e.g., Lee et al. 2015; Schreiber et al. 2015; Erfanianfar et al. 2016), in line with the findings of Wuyts et al. (2011).

As shown above, the $\psi*$–$M*$ relation for our FIELDGALAXY sample, consisting of a morphologically selected pure sample of disk-dominated systems, shows no indication of a break over its entire stellar mass range of $10^9\,M_e$–$10^{11}\,M_e$. As we will show in Section 6, this is also the case for the $\psi*$–$M*$ relation of the GROUPGALAXY sample, with both findings being consistent with previous work on the $\psi*$–$M*$ relation of spiral galaxies (Grootes et al. 2014). As a result, we thus conclude that our findings supply strong evidence that the observed break in the SFMS can be attributed to more bulge-dominated galaxies entering/dominating the sample at higher stellar mass. In essence the occurrence of the break is then linked to bulges and disks differing in the amount of star formation they can support per unit stellar mass, which may potentially be linked to their different kinematics, as argued in Grootes et al. (2014). We will return to this question in the context of a more detailed analysis of the SFMS, decomposed by morphology, in an upcoming paper (L. J. M. Davies et al. 2017, in preparation).

6. The sSFR–M_* Relation for Spiral Galaxies in the Group Environment

For the GROUPGALAXY sample we derive the median $\psi* - M*$ relation in exactly the same manner as used for the FIELDGALAXY sample. This is illustrated in Figure 10, where we plot the relation for the GROUPGALAXY sample before (top panel) and after (middle panel) applying attenuation corrections, using the same binning in stellar mass $M*$ as for the FIELDGALAXY sample shown in Figure 8. In both cases the scatter in the relation is larger than that for the field sample. This may result from a larger intrinsic scatter in the relation or be due to differential effects of the environment on the dust content of and hence attenuation of emission from galaxies. However, as we show in Appendix B, the latter explanation appears unlikely, so we attribute the finding to a true increase in the scatter of the SFR of spiral/disk galaxies at fixed $M*$ in the group environment.

As for the FIELDGALAXY sample, we find that the attenuation-corrected $\psi*$–$M*$ relation of the GROUPGALAXY sample can be, to first order, well described by a power law $y_* \mu M^g_*$ The results of this fit are listed in Table 2. After applying attenuation corrections, we find a value of $\gamma = -0.43 \pm 0.03$ over the full range in $M*$ considered, with a scatter of 0.59 dex interquartile[38] (see Table 2). Thus, the slope of the relation is close to that found for the FIELDGALAXY sample, although the scatter is twice as large, indicative of an influence of the group environment on the sSFR of group member spiral galaxies.

A comparison of our results for the power-law fits to the y_*–M_* relation of the FIELDGALAXY and GROUPGALAXY samples, as listed in Table 2, with the power-law fit by Grootes et al. (2014) to the $\psi*$–$M*$ relation of a morphologically selected sample of galaxies being analogous to ours but without distinction between group and field galaxies ($\gamma = -0.5 \pm 0.12$), finds them to be consistent. The slopes of the fits agree within the uncertainties, and while Grootes et al. (2014) find a scatter of 0.43 dex interquartile rather than 0.35 dex as for the FIELDGALAXY sample, given that we find that ∼22% of spiral galaxies of a given stellar mass $M*$ are *not* in the FIELDGALAXY sample, this is entirely consistent with the expected contribution to the scatter arising from grouped spiral galaxies.

For the purposes of considering the influence of the group environment on the SFR of spiral/disk galaxies, a rigid stellar mass binning such as hitherto employed may blunt the sensitivity of the analysis to differential effects as a function of stellar mass, in particular if the binning is relatively coarse (due to small sample sizes). For this reason, in the rest of the paper we have chosen to adopt a slightly different approach to identifying the median y_*–M_* relation for our samples of group galaxies. Rather than using a fixed binning in stellar mass, we make use of a sliding top-hat bin containing 40 galaxies and determine the median and quartiles of the sSFR $\psi*$ in this bin, plotting the derived values against the median stellar mass of the galaxies in the bin. The choice of 40 galaxies is dictated by the need for the span in mass to be small enough for the systematic shift of $\psi*$ arising from gradients in the source density of the sample as a function of stellar mass to be small over the extent stellar mass sampled by the bin. The result of this approach is shown in the bottom panel of Figure 10, where the median is shown as a solid red line, and the uncertainty on the median and the interquartile range are depicted as dark and light shaded regions, respectively. Its advantages are immediately apparent, as the undulation of the binned

[37] For comparison purposes, we have used the median redshift of the galaxy population in the high stellar mass local and distant bins, which are $z = 0.05$ and $z = 0.1$, respectively. We then calculate the expected shift using Equation (28) of Speagle et al. (2014).

[38] The scatter has been determined as for the FIELDGALAXY sample relation.

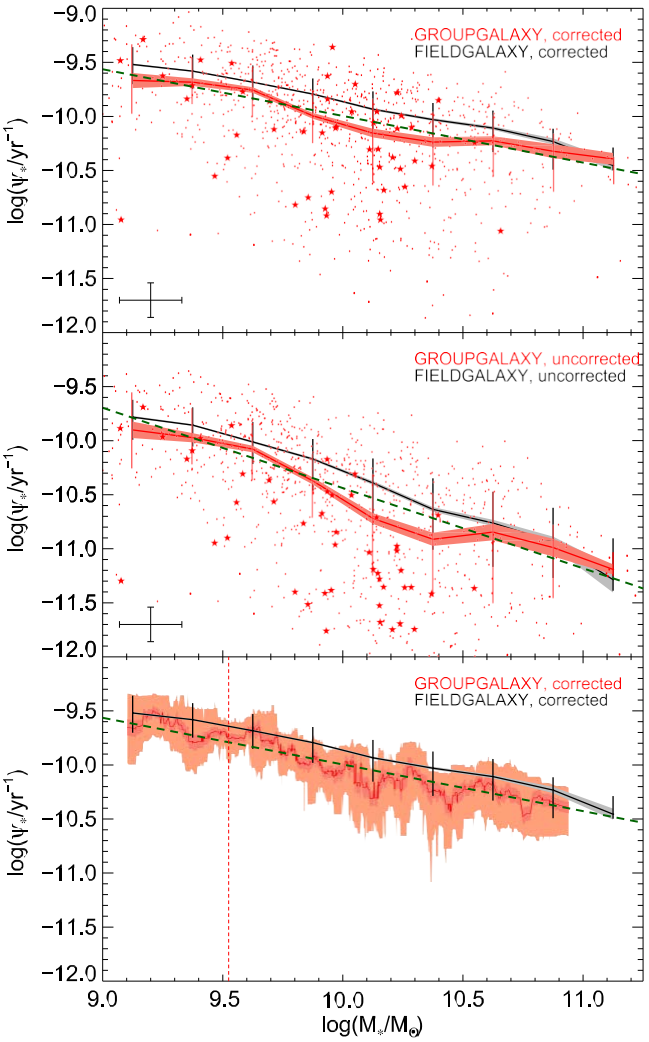

Figure 10. ψ* as a function of $M*$ for the GROUPGALAXY sample, before (middle) and after (top) application of attenuation corrections. The median of the distribution in bins of 0.25 dex in $M*$ is shown as a red solid line, with the error bars indicating the interquartile range and the bootstrapped uncertainty in the median shown as a shaded region. For comparison the average measurement uncertainties (1σ) for an average galaxy are shown at bottom left. The relation for the FIELDGALAXY sample is overplotted for comparison. Dark-green dashed lines indicate single power-law fits to the binwise median values of ψ* for the GROUPGALAXY sample in the range of $M* > 10^{9.5}\,M_e$. As in Figure 8, the 5% most inclined galaxies are denoted by stars, demonstrating that also in the group environment a significant fraction of apparently red low-sSFR galaxies actually have normal sSFRs. The bottom panel shows the median ψ*–$M*$ relation for the GROUPGALAXY sample determined in a sliding top-hat bin containing 40 galaxies. The resulting median relation is shown as a solid red line, with the uncertainty on the median and the interquartile range shown as dark and light shaded regions, respectively. The y_*–M_* relation from Figure 8 is overplotted, as is the power-law fit to the attenuation-corrected GROUPGALAXY sample from the top panel (see also Table 2). The stellar mass limit above which the top-hat bins can be considered mass complete is shown as a vertical red dot-dashed line. The ψ*–$M*$ relations for the FIELDGALAXY and GROUPGALAXY samples, including interquartile ranges and uncertainties of the median (for both fixed and top-hat binning), are available online as "data behind the figure." The data used to create this figure are available.

ψ*–$M*$ relation around the power-law fit for the attenuation-corrected GROUPGALAXY sample seen in the top panel of Figure 10 is revealed as most likely arising from statistical fluctuations.

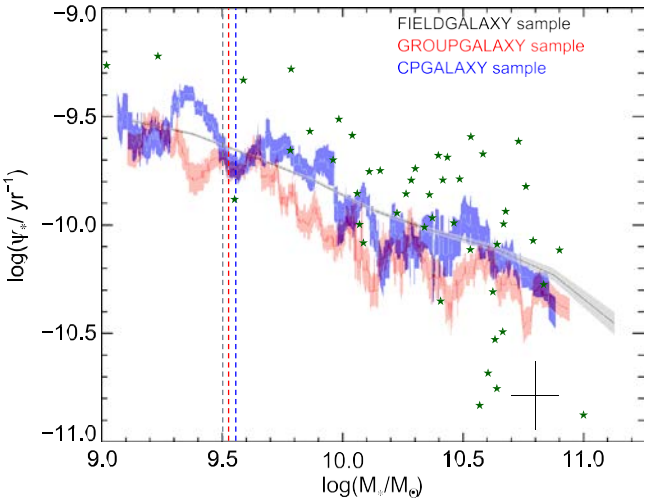

Figure 11. ψ* as a function of $M*$ for the FIELDGALAXY sample (gray), the GROUPGALAXY sample (red), and the CPGALAXY sample (blue). For the GROUPGALAXY and CPGALAXY samples, the median value of ψ* in a sliding top-hat bin containing 40 galaxies is shown as a solid line. The wider shaded area indicates the bootstrapped uncertainty on the median. For the FIELDGALAXY sample the relation is shown in bins of equal size in $M*$ as in Figure 8, with the shaded area again corresponding to the uncertainty in the median. The stellar mass limit above which the samples can be considered mass complete ($M* = 10^{9.5}\,M_e$) is indicated by a dotted gray line. Colored dot-dashed lines indicate the stellar mass above which the galaxies in the moving top-hat bins are all above the mass completeness limit. The galaxies in the MERGER sample have been overplotted as dark-green stars. The ψ*–$M*$ relations for the FIELDGALAXY, GROUPGALAXY, and CPGALAXY samples, including uncertainties of the median, are available online as "data behind the figure." The data used to create this figure are available.

6.1. Comparison with the FIELDGALAXY Sample

In order to quantify the effect of the group environment on the star formation of spiral/disk galaxies, we begin by comparing the median ψ*–$M*$ relation of the GROUPGALAXY and FIELDGALAXY samples as shown in Figure 11 (see also Figure 8). The median ψ*–$M*$ relation for the GROUPGALAXY sample in a sliding top-hat bin of 40 galaxies in width is shown in red, with the uncertainty on the median indicated by the shaded area, while the reference relation defined by the FIELDGALAXY sample is shown in black/gray. Although the scatter is large, it is apparent that the median relation of the GROUPGALAXY sample is suppressed with respect to the reference relation for galaxies with stellar mass $M* \gtrsim 10^{9.7}\,M_e$. This suppression, while only mild (0.1–0.2 dex), is quite marked, with no readily discernible dependence on galaxy stellar mass.

Although the median represents a statistically robust characteristic of a sample, very different distributions may result in the same median value. Therefore, to complement our consideration of the median ψ*–$M*$ relation that collapses the range of ψ* for a narrow bin of stellar mass $M*$, we also consider the full distribution of ψ* in two disjoint ranges of $M*$ separated at $M* = 10^{10}\,M_e$. Specifically, we investigate the effect of the group environment on the sSFR of spiral galaxies by considering the offset of a galaxy's sSFR ψ* from the median value found for galaxies of comparable stellar mass in the FIELDGALAXY sample, defined as

$$\mathrm{D}\log y_* = \log(y_*) - \log(\overline{y_{*,\mathrm{field}}}(M_*)), \quad (3)$$

where $\overline{y_{*,\mathrm{field}}}(M_*)$ is the median value of ψ* for a field galaxy of mass $M*$. $\overline{y_{*,\mathrm{field}}}(M_*)$ as used in Equation (3) has been

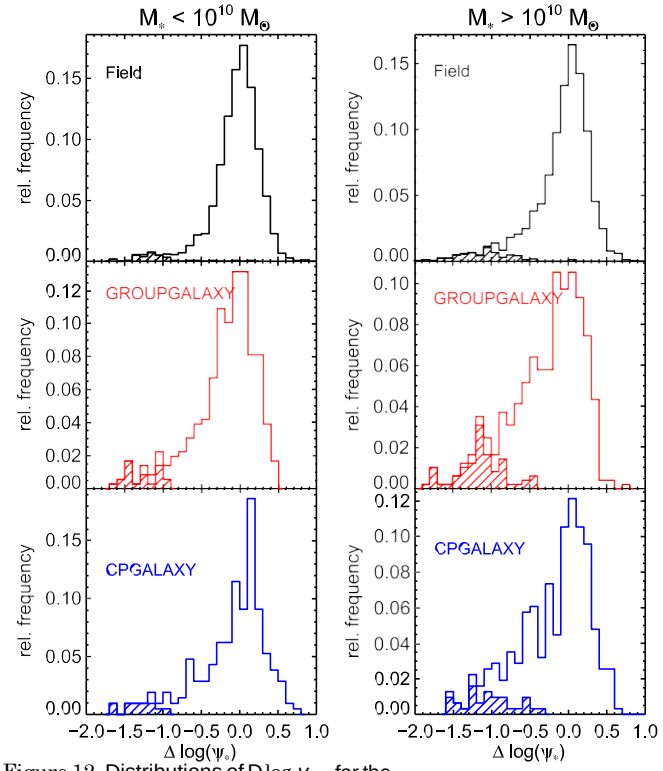

Figure 12. Distributions of $D\log(y_*)$ for the FIELDGALAXY ' GROUPGALAXY' and CPGALAXY samples in the low (left) and high (right) stellar mass range, separated at $M_* = 10^{10} M_e$. For the low-mass range we only consider the range over which the samples can be deemed mass complete ($10^{9.5} M_e \leq M_* < 10^{10} M_e$) in constructing the histograms. The distribution of upper limits is indicated by the hatched histograms. The distributions of $\Delta\log(\psi_*)$ of the FIELDGALAXY, GROUPGALAXY, and CPGALAXY samples in both stellar mass ranges are available online as "data behind the figure." The data used to create this figure are available.

defined as a piecewise continuous function obtained by the linear interpolation of the binned median values of ψ_* as shown in Figure 8.

Figure 12 shows the distributions of $D\log(y_*)$ for the FIELDGALAXY (top), GROUPGALAXY (middle), and CPGALAXY (bottom) samples in the low (left) and high (right) stellar mass range. For the FIELDGALAXY sample, we find that the distribution is strongly peaked around its median in both stellar mass ranges, with a small asymmetrical tail extending to values of $D\log y_*$ corresponding to very low sSFR. This tail is more populous in the higher stellar mass range ($M_* \geq 10^{10} M_e$), encompassing 18% of the sample in this range of M_* compared to 7% in the low stellar mass range, in agreement with Figure 8.

Similarly to the FIELDGALAXY sample, the distribution of $D\log(y_*)$ for the GROUPGALAXY sample displays a pronounced peak in both ranges of stellar mass, coinciding with that of the FIELDGALAXY sample. However, the population of galaxies in the GROUPGALAXY sample with very low values of $D\log y_*$, i.e., strongly suppressed sSFR with respect to the median of the FIELDGALAXY sample, is significantly larger in both stellar mass ranges, with ≥20% of the population with $10^9 M_e \leq M_* \leq 10^{9.5} M_e$ having $D\log y_* < -0.5$, in comparison to 7% for the FIELDGALAXY sample, and 30% of the GROUPGALAXY having $D\log y_* < -0.5$, compared to 18% of the FIELDGALAXY sample in the range $M_* > 10^{10} M_e$. Thus, the small shift observable in the median y_*–M_* relation can be attributed to an increase in the minority population of galaxies with strongly suppressed sSFR.

A more rigorous quantitative statistical investigation of of the similarity of the distributions of $D\log(y_*)$, and thus, by extension, also of the significance of the observed shift in y_*–M_*, is complicated by the fact that the measurements of ψ_* include upper limits at the 2.5σ level (NUV upper limits derived for the *GALEX*-GAMA photometry) in addition to reliable detections.[39] Accordingly, in quantifying the (lack of) similarity of the samples it is necessary to make use of a nonparametric test capable of accounting for censoring in the data. We have, therefore, adopted the generalized Wilcoxon test as suggested by Peto & Peto (1972), applied to the case of upper limits by, e.g., Avni et al. (1980), Pfleiderer & Krommidas (1982), and Feigelson & Nelson (1985), and available in the statistical analysis package STSDAS.[40] In the following we will refer to this test simply as the Peto test. It should be noted that any such test, by necessity, applies a weighting scheme to the upper limits, making the test more or less sensitive to different regions of the distribution, and cannot recover the information discarded by the use of upper limits.

Applying Peto tests to compare the distributions of $D\log(y_*)$ for the FIELDGALAXY and GROUPGALAXY samples supports our previous findings in the sense that the distributions are found to differ significantly in both stellar mass ranges ($p < 10^{-5}$). A summary of the Peto tests comparing the distributions of $D\log(y_*)$ for the FIELDGALAXY and GROUPGALAXY samples in both stellar mass ranges is presented in Table 3.

When comparing the distributions of $D\log(y_*)$ in wide bins of M_*, one must, in principle, also consider the relative distributions of M_* *within* the relevant bins. However, as the differences in the relative weighting in M_* in each range of M_* between the samples are small and the offset in the median relation is largely uniform over the full stellar mass range, the comparability of the distributions of $D\log(y_*)$ for the FIELDGALAXY and GROUPGALAXY samples is not strongly biased.

Finally, the main systematic uncertainty in the absolute shifts in ψ_* found for the members of the GROUPGALAXY sample is likely to be due to environment-dependent effects on the dust content and distribution of spiral galaxies, as discussed in Appendix B. However, shifts of the magnitude required to increase the population of galaxies with strongly suppressed sSFR seem unlikely, as they would require systematic changes in the dust surface density of the spiral galaxies by factors of a few, compared to the relation calibrated by Grootes et al. (2013). This is discussed further in Appendix B.

In summary, we find that for the GROUPGALAXY sample, i.e., spiral/disk galaxies in galaxy groups, the median sSFR ψ_* at a given stellar mass is suppressed by only 0.1–0.2 dex compared to similar objects in the FIELDGALAXY sample. Furthermore, this shift is the result of an increase in size of the minority population of galaxies with strongly suppressed sSFRs with

[39] Given that the distribution of the actual measurements of sSFR of undetected objects is likely to follow a Poisson distribution, the inclusion of these data at the 2.5σ upper limit level may significantly alter the shape of the distribution (with this being of increasing importance for samples with a potentially suppressed sSFR ψ_*).

[40] The STSDAS is a data analysis package based on the IRAF environment and developed and maintained by the software division of the Space Telescope Science Institute, Baltimore, Maryland, USA.

Table 3
Comparison of the FIELDGALAXY, GROUPGALAXY, and CPGALAXY Samples

Sample		GROUPGALAXY	CPGALAXY	FIELDGALAXY
GROUPGALAXY	$\log(M_*) \square 10$	1	$\square 10^{-5}$	$\square 10^{-5}$
	$\log(M*) > 10$	1	0.024	$\square 10^{-5}$
CPGALAXY	$\log(M*) \square 10$	$\square 10^{-5}$	1	0.87
	$\log(M*) > 10$	0.024	1	$\square 10^{-5}$
FIELDGALAXY	$\log(M*) \square 10$	$\square 10^{-5}$	0.87	1
	$\log(M*) > 10$	$\square 10^{-5}$	$\square 10^{-5}$	1

Note. Significance (p) values of Peto tests performed between the FIELDGALAXY, GROUPGALAXY, and CPGALAXY samples. For each combination Peto tests have been performed in two disjoint bins of stellar mass split at $M* = 10^{10}\,M_e$ (the low stellar mass bin has been limited to the mass complete sample, i.e., $M* \square 10^{9.5}\,M_e$.

respect to the median of the FIELDGALAXY sample, while the majority of galaxies in the GROUPGALAXY sample have sSFRs comparable to their FIELDGALAXY sample counterparts.

6.2. SFR of Spiral Galaxies in Close Pairs

While the members of close pairs of galaxies have been excluded from the *GROUPGALXAY* sample for the purposes of our main investigation, we briefly consider the CPGALAXY sample and the MERGER sample in terms of its median y_*–M_* relation and distribution of $\mathrm{D}\log(y_*)$, as shown in Figures 11 and 12.[41]

As expected (e.g., Barton et al. 2000; Robotham et al. 2013; Davies et al. 2015), we find that the sSFR of merging systems is, on average, enhanced, even with respect to field spirals, as shown by the green stars in Figure 11. There seems to be little stellar mass dependence of this enhancement over the range of $9.5 \square \log(M_*/M_\square) \square 10.5$. Above $\log(M_*/M_\square) = 10.5$, however, the sSFR of merging spirals appears to no longer only be enhanced, with some galaxies also showing a strongly suppressed sSFR with respect to the FIELDGALAXY reference sample, resulting in a huge spread in the sSFR of merging spiral galaxies at these masses.

For spiral galaxies that are members of close pairs of galaxies but not merging, we find that the median $\Psi*$–$M*$ relation, shown in blue in Figure 11, is comparable to the field reference relation and may even be elevated for galaxies with a stellar mass below $\sim 10^{10}\,M_e$. Figure 12 shows the distributions of $\Delta\log(\Psi*)$ for the CPGALAXY (blue) and FIELDGALAXY (black) samples in the low (left column) and high (right column) stellar mass ranges. Performing a Peto test comparing the distributions of $\mathrm{D}\log(y_*)$ of the CPGALAXY and FIELDGALAXY samples in the low stellar mass range, one finds that the null hypothesis is not rejected ($p = 0.87$; see Table 3 for the results of Peto tests comparing the CPGALAXY, GROUPGALAXY, and FIELDGALAXY samples in both ranges of stellar mass); however, a closer inspection does find the relative weight of the tail of galaxies with suppressed sSFR in the CPGALAXY sample to be greater than for the FIELDGALAXY sample, albeit slightly less so than for the GROUPGALAXY sample, as well as finding the CPGALAXY sample to be more skewed toward high values of $\mathrm{D}\log y_*$, i.e., increased sSFR, including a slight shift in the position of the peak. In line with these findings, we also find the distributions of $\mathrm{D}\log(y_*)$ of the CPGALAXY sample and the GROUPGALAXY sample to differ significantly ($p \square 10^{-5}$) in the low stellar mass range.

In the high stellar mass range we find the distribution of $\mathrm{D}\log(y_*)$ for the CPGALAXY to be peaked at the position of the peak of the FIELDGALAXY sample. However, in this mass range, the population of galaxies with strongly suppressed sSFR in the CPGALAXY sample is fully comparable to that of the GROUPGALAXY sample. Nevertheless, the CPGALAXY sample is slightly skewed toward increased sSFR with respect to the FIELDGALAXY sample. As a result, although the distributions of $\mathrm{D}\log y_*$ for both samples differ significantly ($p < 10^{-5}$), the median y_*–M_* relation, lying between that of the GROUPGALAXY sample and the FIELDGALAXY sample, as shown in Figure 11, is generally comparable to the field reference relation. Regardless of the increased similarity of the CPGALAXY and GROUPGALAXY samples in the range of $M* \square 10^{10}\,M_e$, the distributions of $\mathrm{D}\log(y_*)$ are found to differ significantly, as in the low-mass range, in summary retroactively justifying the exclusion of close pairs from our analysis.

Overall, we find that merging activity has a strong effect on the sSFR of spiral/disk galaxies, leading to a significant enhancement of the sSFR in spiral galaxies with $M* \square 10^{10.5}\,M_e$ and to a very large scatter above this mass. This effect is markedly stronger than any more general environmental impact. The sSFR of galaxies in close pairs appears to be only marginally affected by the fact of having a neighbor in the direct vicinity. However, for the adopted definition of a close pair (a neighbor within 50 kpc h^{-1} projected distance and 1000 km s^{-1}), it is likely that a large fraction of the close pairs identified in this manner are by no means interacting, diluting possible effects.

7. Spiral Galaxies in the Group Environment: Centrals and Satellites

Hitherto we have considered the GROUPGALAXY sample as a whole, i.e., we have considered all spiral/disk-dominated galaxies in galaxy groups, regardless of their being a satellite galaxy in the group, or of being the central galaxy of the group. However, as mentioned in the introduction, this distinction may be fundamental to the ability of galaxies to accrete gas and fuel ongoing star formation. In the following, we therefore separate the GROUPGALAXY sample into central and satellite spiral group galaxies as described in Section 4.5.

[41] Even though strong perturbative galaxy–galaxy interactions are likely to lead to morphological transformations, a subset of these close pair and merger galaxies will still have a largely spiral/disk structure. Insofar as these are identified as spirals, they have been treated analogously to the spiral galaxies in the FIELDGALAXY and GROUPGALAXY samples. The attenuation corrections and SFR estimates may, however, be less accurate for these perturbed systems.

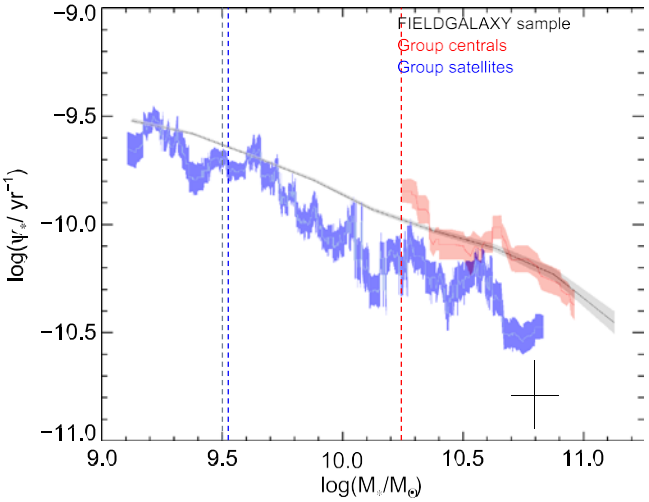

Figure 13. ψ* as a function of $M*$ for the FIELDGALAXY sample (gray), the satellite galaxies in the GROUPGALAXY sample (blue), and the central galaxies in the GROUPGALAXY sample (red). For the satellite and central galaxies in the GROUPGALAXY sample the solid line shows the median value in a sliding top-hat bin containing 40 and 25 galaxies, respectively. The wider shaded area indicates the uncertainty on the median. For the FIELDGALAXY sample the relation is shown in bins of equal size in $M*$ as in Figure 11, with the shaded area again corresponding to the uncertainty in the median. The stellar mass limit above which the samples can be considered mass complete ($M* = 10^{9.5} M_e$) is indicated by a dotted gray line. Colored dot-dashed lines indicate the stellar mass above which the galaxies in the moving top-hat bins are all above the mass completeness limit. The ψ*–$M*$ relations for the FIELDGALAXY sample, as well as for the central and satellite subsamples of the GROUPGALAXY sample, including uncertainties of the median, are available online as "data behind the figure." The data used to create this figure are available.

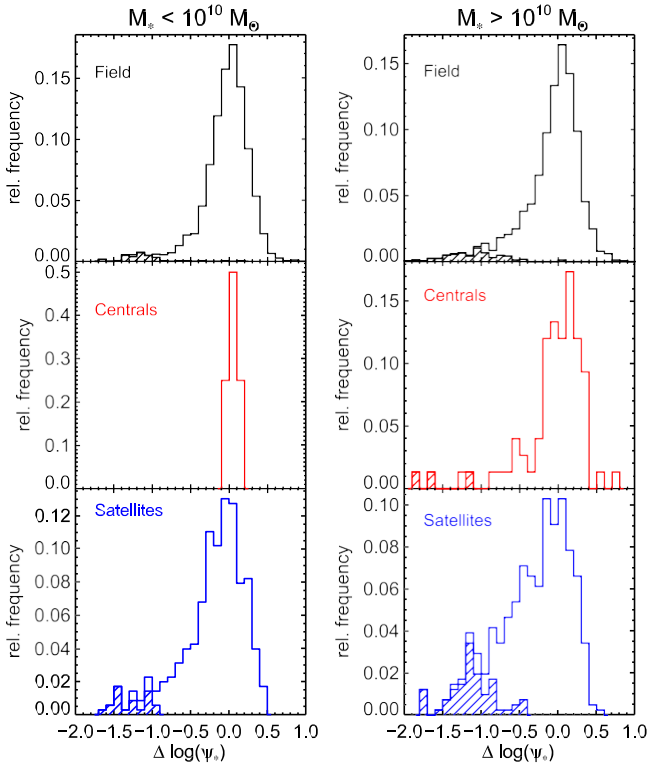

Figure 14. Histograms of the distribution of Δlog(ψ*) for field (top), central (middle), and satellite (bottom) spiral galaxies with $M* < 10^{10} M_e$ (left) and $M* > 10^{10} M_e$ (right). The distribution of upper limits is indicated by the hatched histograms. The distributions of Δlog(ψ*) for the FIELDGALAXY sample, as well as for the central and satellite subsamples of the GROUPGALAXY sample, are available online as "data behind the figure." The data used to create this figure are available.

7.1. Group Central Spiral Galaxies

Using the y_*–M_* relation of the FIELDGALAXY sample, i.e., largely isolated central spiral galaxies, as a reference, we consider the impact of the group environment on the star formation, more specifically the y_*–M_* relation, respectively, of group central spiral galaxies. As shown in Figure 6, the sample of group central spiral galaxies is skewed toward high-mass galaxies, as expected given the nature of these objects as the central galaxy of a group encompassing at least three galaxies with $M* \gtrsim 10^{9.5} M_e$. In terms of the median y_*–M_* relation, however, that of the group centrals is very close to that of our reference sample over the full mutual range in $M*$, as shown in red in Figure 13. Nevertheless, there is a hint that the slope in the relation may be slightly steeper for group central spiral galaxies than for the FIELDGALAXY sample, with galaxies at $M* \approx 10^{10.4} M_e$ having slightly higher median sSFR than the reference relation, while those with $M* \gtrsim 10^{11}$ appear to have a minimally suppressed median value of ψ*.

Considering the distributions of $\Delta \log(y_*)$ (shown in red in Figure 14 for the low and high stellar mass ranges, respectively), the centrals strongly resemble the FIELDGALAXY sample, with a pronounced peak at the position of the peak of the FIELDGALAXY sample and a negligible tail of galaxies with strongly suppressed sSFR with respect to the median relation of the FIELDGALAXY sample (13% in the stellar mass range $M* \gtrsim 10^{10} M_e$). As a total of four central spiral galaxies have masses below $M* = 10^{10} M_e$, we ignore the low stellar mass range in our comparisons. As summarized in Table 4, the null hypothesis that the distributions of $\Delta \log(y_*)$ for the group central spiral galaxies and the FIELDGALAXY sample in the mass range $M* > 10^{10} M_e$ are statistically similar cannot be discarded.

Table 4
Comparison of Satellites, Centrals, and the FIELDGALAXY Sample

Sample		Centrals	Satellites	FIELD
Centrals	log(M*) ≤ 10	1	0.18	0.69
	log(M*) > 10	1	≤10^−5	0.19
Satellites	log(M*) ≤ 10	0.18	1	≤10^−5
	log(M*) > 10	≤10^−5	1	≤10^−5
FIELD	log(M*) ≤ 10	0.69	≤10^−5	1
	log(M*) > 10	0.19	≤10^−5	1

Note. Significance (p) values of Peto tests performed between the central and satellite galaxy subsamples of the GROUPGALAXY samples and the reference FIELDGALAXY sample. For each combination Peto tests have been performed in two disjoint bins of stellar mass split at $M* = 10^{10} M_e$.

In summary, our analysis finds that the sSFR of group central spiral galaxies is comparable to that of largely isolated field central spiral galaxies matched in stellar mass, with almost no evidence of any influence of the group environment on the sSFR of central spiral galaxies. We will return to this result and our findings on the evolution of the y_*–M_* relation of the central spiral galaxies of the FIELDGALAXY sample in a subsequent paper in this series considering the gas fueling of

central spiral galaxies. In this paper, we will continue by focusing on the star formation and gas fueling of satellite spiral galaxies.

7.2. Group Satellite Spiral Galaxies

Given the expected differences in the physical circumstances of central spiral galaxies (in general) and satellite spiral galaxies vis à vis their ability to accrete gas, we consider the y_*–M_* for satellite spiral/disk-dominated galaxies, contrasting it with our reference relation defined by the FIELDGALAXY sample. As shown in Figure 13, the median y_*–M_* relation for satellite spiral galaxies (shown in blue) is suppressed with respect to the reference relation over the full range in stellar mass. The suppression of the median is found to be moderate, increasing very mildly from ~0.1–0.2 dex for $M* < 10^{9.75} M_e$ to ~0.2–0.3 dex at a given $M*$ for $M* \gtrsim 10^{10} M_e$. Overall, the offset of the y_*–M_* relation for satellite spiral galaxies from the FIELDGALAXY sample reference relation appears to be largely independent of stellar mass, albeit possibly with a very weak dependence in the sense that the offset is smaller at lower stellar mass.

Considering the distributions of $D\log(y_*)$ for the satellites (blue) with $M* < 10^{10} M_e$ (left column) and with $M* \gtrsim 10^{10} M_e$ (right column) as shown in Figure 14, and comparing with the distributions of the FIELDGALAXY sample (black) shown in the same figure, one finds that the satellites' distributions show a strong peak at the position of the peak in the FIELDGALAXY sample distribution. However, the population of galaxies with strongly suppressed sSFR is larger in the satellite sample (in both stellar mass ranges) than in the FIELDGALAXY sample. In the low stellar mass bin, 18% of the satellite galaxies have $D\log(y_*) < -0.5$, compared to 7% for the FIELDGALAXY sample, while the difference in the distributions is even more pronounced in the high stellar mass range, with 32% of the satellites having $D\log(y_*) < -0.5$, compared to 18% for the FIELDGALAXY sample. This is mirrored in the results of Peto tests comparing the distributions (the results of Peto tests comparing the distributions of satellites, centrals, and the FIELDGALAXY sample are summarized in Table 4), which find them to differ significantly in both ranges of $M*$.[42]

Overall, we find the majority (≳70%) of satellite spiral galaxies to be forming stars at a rate comparable to their counterparts in the FIELDGALAXY sample. The mild suppression of the median $\psi*$–$M*$ relation for these group satellite spiral galaxies can be attributed to a minority population (≲30%) of galaxies with strongly suppressed sSFR with respect to the FIELDGALAXY reference.

8. Star Formation and Star Formation Histories of Satellite Spiral Galaxies

In the previous section we have shown that the vast majority of satellite spiral/disk galaxies display sSFRs comparable to those of their field counterparts, with the observed moderate suppression of the median y_*–M_* relation for group satellite spiral galaxies being caused by a minority of galaxies with strongly suppressed sSFR, as shown in Figure 14. Thus, it appears that while the group environment in terms of galaxy–IHM interactions has a strong impact on a minority of satellite spiral/disk galaxies, the majority population remains unaffected and behaves nigh identically to their central counterparts in the field.

This observed similarity between the sSFR of satellite and field central spiral galaxies is highly surprising, since, as outlined in Section 1, satellite galaxies are expected to be largely unable to accrete gas to resupply/fuel star formation activity, while field central galaxies are thought to experience ongoing gas fueling. This is exacerbated by the fact that, as shown in Figure 6, the spiral fraction as a function of stellar mass for satellite galaxies has only decreased by 30%–40% with respect to galaxies in the field, and accordingly a substantial fraction of spiral satellites have likely resided in the group environment as satellite galaxies for several gigayears. As the majority of the spiral satellite galaxies (≳70%) display sSFRs comparable to those of their field counterparts, it seems inevitable that a substantial fraction of these actively star-forming spiral satellites have resided in the group environment for an extended period. The question one has to consider is thus whether gas fueling is ongoing for group satellite spiral galaxies.

As a first step to answering this question, we consider the gas exhaustion timescales for spiral galaxies with stellar masses in the range of $9.5 \lesssim \log(M_*/M_\odot) < 10$ and $10 \lesssim \log(M_*/M_\odot)$, respectively. We cannot do this directly for the GAMA sample, as measurements of the gas masses are not available; however, we can make use of the relation between stellar mass and gas mass for late-type galaxies compiled by Peeples et al. (2014) and the y_*–M_* relation for the FIELDGALAXY sample presented in Figure 8 to obtain a conservative estimate of the exhaustion timescales

$$t_{\rm exhaust} = M_{\rm gas}/{\rm SFR}. \quad (4)$$

Adopting this approach, one finds values of 2.8 and 2.7 Gyr for the mass ranges $9.5 \lesssim \log(M_*/M_\odot) < 10$ and $10 \lesssim \log(M_*/M_\odot)$, respectively.[43] Although quite substantial, these timescales represent the timescale on which *all* gas (atomic and molecular hydrogen) of the galaxy has been consumed by star formation alone, also ignoring any potential outflows of gas from the galaxy that may considerably reduce the actual exhaustion timescale (see also McGee et al. 2014). Thus, it seems difficult to explain the lack of a large shift in the star formation activity of the majority of the satellite spiral galaxies simply in terms of the depletion of the gas reservoir (even if these were to be retained in a form comparable to the largely non-grouped galaxies in the sample of Peeples et al. 2014). Nevertheless, these exhaustion timescales of ~3 Gyr are not really decisive, as they are only comparable to the expected time spent as a satellite by the galaxies considered.

To approach the question in a more quantitative manner, we therefore consider a number of simple parameterized SFHs for galaxies in the group environment that can be readily related to their gas cycle (see Section 9) and have been chosen to bracket the range of plausible SFHs for these objects. These SFHs are schematically illustrated in Figure 15. For the SFHs in these

[42] As for the FIELDGALAXY and GROUPGALAXY samples, the lack of stellar mass dependence of the offset of the median $\psi*$–$M*$ for satellite galaxies, combined with the similarity of the relative distributions of $M*$ within the

broad mass ranges considered, lends confidence in the comparability of the distributions of $\Delta\log(\psi*)$ for the FIELDGALAXY and satellite spiral samples.

[43] We have used stellar mass values corresponding to the median stellar mass in each range: $M* = 10^{9.75}\,M_e$ and $M* = 10^{10.3}\,M_e$, respectively.

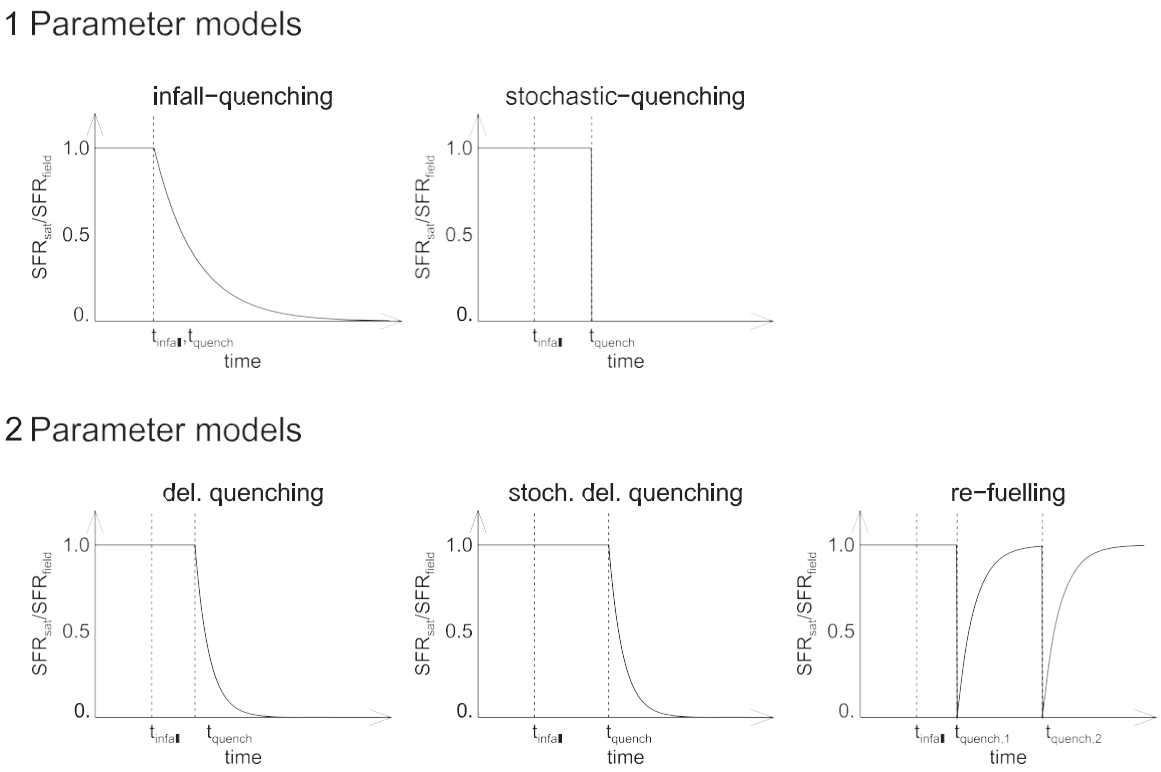

Figure 15. Schematic depictions of the parameterized SFH models (relative to a comparable field galaxy) considered, split into one- and two-parameter families as shown. Each model name is shown on the plot above the depiction of its characteristic SFH. In all cases the dashed vertical lines show the infall time $t_{\rm infall}$, i.e., the time at which the galaxy became a satellite for the first time, as well as the incidence of a "quenching event," i.e., either the complete shutoff of star formation (stochastic quenching model, refueling model) or the onset of a gradual decline (the other three models).

models we predict the distributions of $\Delta\log(\psi*)$ and compare these with our empirical results. This approach enables us to identify the SFH elements most applicable to our data and to subsequently (see Section 9) interpret our results in the physical context of the gas cycle of galaxies, including quantitative estimates of the in- and outflows of gas to and from the galaxy.

Full details of our modeling procedure are provided in Appendix C. In brief, however, we proceed by creating samples of galaxies infalling into groups and becoming satellites, which we evolve forward in time to observation at $z = 0.1$ following the parameterized SFH of our models. This approach requires knowledge of the time a galaxy has been a satellite, i.e., the infall time, as well as of the stellar mass and SFR at the time of infall, and we have, as far as possible, adopted an empirically driven approach to determining these quantities. In creating our samples of infalling galaxies we Monte Carlo sample the $z \approx 0.1$ FIELDGALAXY sample distributions of stellar mass and SFR (in bins of M^*) and evolve the galaxy back to its infall time following the empirical parameterization of the SFMS presented by Speagle et al. (2014). An empirical determination of the infall time distribution, however, is not possible. Therefore, in determining the distribution of infall times for our model samples we have made use of the distribution of infall times found for satellite galaxies in the mock GAMA survey light cones produced using the Millennium DM simulation (Springel et al. 2005) and the GALFORM semianalytic galaxy formation model (Bower et al. 2006; Merson et al. 2013).

As shown in Figure 6, the spiral fraction of satellite galaxies is 30%–40% lower than that of the FIELDGALAXY sample, and on average we find a satellite spiral fraction of 30%. The observed decrease in spiral / disk fraction is often linked to the more frequent occurrence of galaxy–galaxy interactions in the group environment, which can morphologically transform disk (-dominated) galaxies to more bulge-dominated systems. However, quenching of star formation in spiral (satellite) galaxies may also give rise to an apparent morphological transformation even without any galaxy–galaxy interaction, as a result of different degrees of fading for the largely passive bulge and the (previously) star-forming disk, and may lead to disk systems no longer being identified as such (e.g., Carollo et al. 2016). Although the selection method of Grootes et al. (2014) is designed to allow quenched systems to enter the selection and we expect the impact of fading to be limited, as previously discussed in Section 4.2, we have nevertheless adopted a very conservative approach to account for this possibility, i.e., in drawing infall times from the distribution found in the mock GAMA light cones for our modeling purposes we assume that the spiral group member satellites correspond to the 30% youngest group members and draw only from the corresponding fraction of the infall time distribution.[44] A full discussion of the modeling is provided in Appendix C.

8.1. One-parameter Models

8.1.1. The "Infall Quenching" Model

The simplest model is the "infall quenching" model shown in Figure 15. In this model, the SFR of a galaxy declines exponentially on a timescale $\tau_{\rm quench}$ upon the galaxy becoming

[44] This approach is conservative in the sense that it places the smallest requirements on the gas reservoirs of the satellite spiral galaxies.

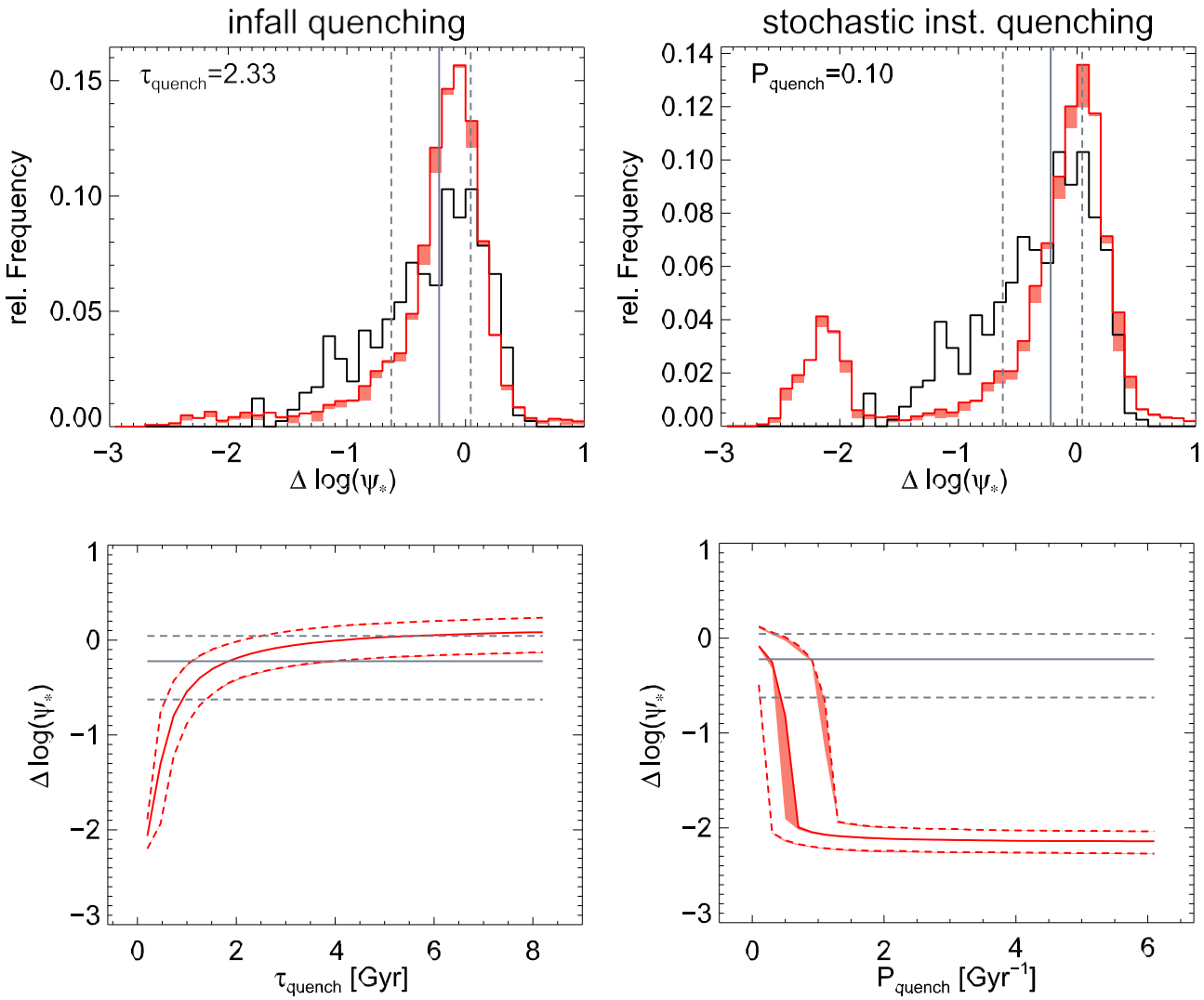

Figure 16. Top: observed distribution of Δlog(ψ*) for the stellar mass range $M* \sim 10^{10} M_e$ in gray, with the first quartile, median, and third quartile of the observed distribution indicated by a dashed, solid, and dot-dashed vertical line, respectively. The average Δlog(ψ*) distribution as obtained from 50 realizations of the infall quenching model (right) and the stochastic quenching model (left) is shown in red. The red shaded regions correspond to a range between the 16th and 84th percentiles in each bin in Δlog(ψ*) as found for the 50 realizations considered. The parameter value of the model depicted (chosen to best reproduce the position of the observed median) is shown at top left. Bottom: position of the first quartile, median, and third quartile (from bottom to top) of the Δlog(ψ*) distribution of the model (left: infall quenching; right: stochastic quenching) as a function of the model parameter in the mass range $M* \sim 10^{10} M_e$ in red. The red shaded regions indicate the range between the 16th and 84th percentiles at each trial value of the model parameter as found from 50 realizations. The locations of the three characteristics of the observed distribution are overplotted in gray, with the first quartile, median, and third quartile indicated by dashed, solid, and dot-dashed lines, respectively.

a satellite at $t_{\rm infall}$, i.e.,

$$\mathrm{SFR}(t) = \mathrm{SFR}(t_{\rm infall}) e^{-(t-t_{\rm infall})/\tau_{\rm quench}}. \quad (5)$$

The predicted distributions of the present-day star formation of group satellite spiral/disk galaxies for this model in the stellar mass ranges $\log(M_*/M_\odot) \sim 10$ and $9.5 \sim \log(M_*/M_\odot) < 10$ are shown in the top left panel of Figures 16 and 17, respectively, overlaid on the observed distribution in that mass range. In order to simplify the characterization of the distribution of Δlog(ψ*), we make use of three robust characteristics, the first quartile, the median, and the third quartile. For the observed distributions each of these is overplotted. The bottom left panels of Figures 16 and 17 show the locations of three characteristics of the Δlog(ψ*) distribution as a function of $\tau_{\rm quench}$ for the mass ranges $\log(M_*/M_\odot) \sim 10$ and $9.5 \sim \log(M*/M_e) < 10$, respectively. It is immediately apparent that the infall quenching model is incapable of simultaneously reproducing the locations of the characteristics of the distribution. Furthermore, the shape of the full distribution obtained for the value of best reproducing the median is very different from that of the data. In particular, the peak of the model distribution is shifted toward lower values of Δlog(ψ*), while displaying a smaller dispersion than the observed distribution.

8.1.2. The Stochastic Quenching Model

In the second one-parameter model, referred to as the "stochastic quenching" model, a galaxy becoming a satellite at time $t_{\rm infall}$ continues to form stars as if it were still a field (central) galaxy. However, with a probability per unit time $P_{\rm quench}$, the star formation of the galaxy is instantaneously completely shut off at a time $t_{\rm quench}$ with $t_{\rm quench} > t_{\rm infall}$, and the galaxy remains dormant thereafter, i.e.,

$$\mathrm{SFR}(t) = \begin{cases} \mathrm{SFR}_{\rm field}(t) & \text{for } t < t_{\rm quench} \\ 0 & t \sim t_{\rm quench}. \end{cases} \quad (6)$$

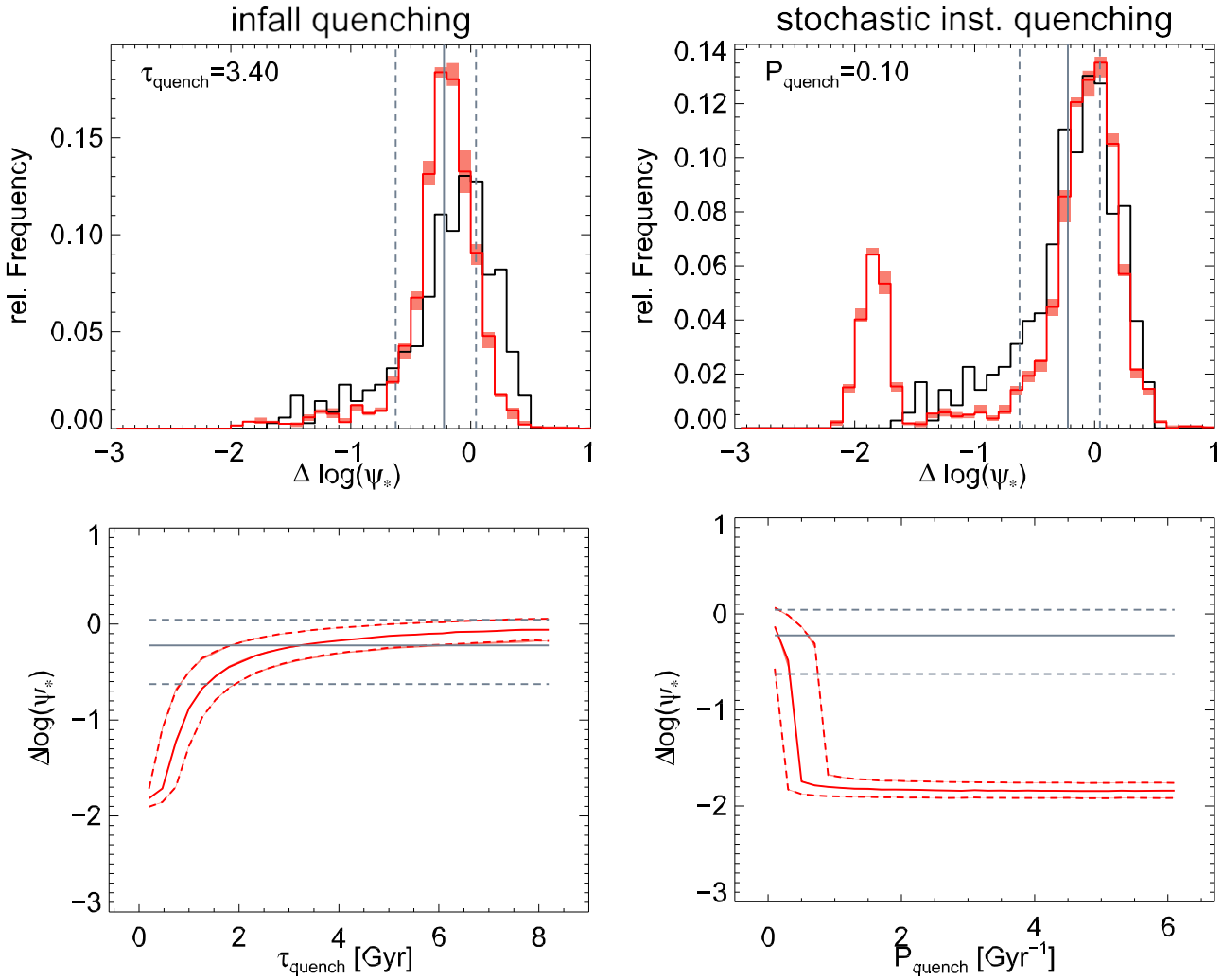

Figure 17. Same as Figure 16, but for the stellar mass range $10^{9.5}\,M_e \leq M_* < 10^{10}\,M_e$.

As for the "infall quenching" model, the locations of the second quartile, the median, and the third quartile of the predicted distribution of $\Delta\log(y_*)$, here as a function of $P_{\rm quench}$, are shown in Figures 16 and 17. For very low values of $P_{\rm quench}$ the stochastic model is nearly able to reproduce the location of all three characteristics of the distribution simultaneously. However, considering the full predicted distribution, one finds that, while the location of the main peak is correct, the "stochastic quenching" model gives rise to a far too large population of galaxies with very strongly suppressed sSFR and lacks the moderately suppressed galaxies found in the observational data.

In summary, neither of the one-parameter models considered is thus capable of satisfactorily reproducing the observed distributions of $\Delta\log(\psi_*)$.

8.2. Two-parameter Models

The family of two-parameter models depicted in Figure 15 encompasses three models. Unlike for the one-parameter models, for two-parameter models, the locations of the characteristics of the $\Delta\log(\psi_*)$ distribution can no longer easily be directly depicted as a function of the parameter values. Instead, we consider the topology of the expression

$$\Delta q_i(p_1, p_2) = \left| q_{i,\rm obs} - q_{i,\rm mod}(p_1, p_2) \right|, \quad (7)$$

where $q_{i,\rm obs}$ represents the ith quartile of the observed distribution of $\Delta\log(\psi_*)$ and $q_{i,\rm mod}(p_1, p_2)$ represents the ith quartile of the model distribution for the parameters p_1 and p_2. This is done separately for each characteristic, and a parameter combination corresponding to a good fit will simultaneously minimize the expressions for all three characteristics.

In the following, to quantify the ability of a model to simultaneously reproduce the characteristics of the observed $\Delta\log(\psi_*)$ distribution, we will consider the quantity

$$Q_i(p_1, p_2) = \begin{cases} [1 - \Delta q_i(p_1, p_2)] \cdot 0.3^{-3} & \text{for } \Delta q_i(p_1, p_2) \leq 0.3 \\ 0 & \text{otherwise} \end{cases} \quad (8)$$

for each characteristic and formulate a composite figure of merit for the performance of the model as

$$Q(p_1, p_2) = \sum_i Q_i(p_1, p_2), \quad (9)$$

which can take values between 1, for a perfect recovery of all characteristics, and 0, for a strong discrepancy between model and observed distributions of $\Delta\log(\psi*)$ (even in only one characteristic).

Figures 18 and 19 show the topologies of the three characteristics ($\Delta q_i(p_1, p_2)$), as well as the whole distribution of $\Delta\log(\psi*)$ for the preferred values of p_1 and p_2 overlaid on the observed distribution, for each of the models in the high and low stellar mass ranges, respectively. Figure 20 shows the topology of the figure of merit $Q(p_1, p_2)$ for each model in both stellar mass ranges, while the preferred parameter values, as well as the attained values of $Q(p_1, p_2)$, are provided in Table 5. In the following, we will discuss all three models individually.

8.2.1. The "Delayed Quenching" Model

The first of the two-parameter models shown in Figure 15 is referred to as the "delayed quenching" model. In this model a galaxy becoming a satellite at time $t_{\rm infall}$ continues to form stars as if it were still a field (central) galaxy for a fixed time $t_{\rm delay}$ until $t_{\rm quench} = t_{\rm infall} + t_{\rm delay}$, after which the SFR declines exponentially on a timescale $\tau_{\rm quench}$. Thus, the functional form of the SFR is given by

$$\mathrm{SFR}(t) = \begin{cases} \mathrm{SFR}_{\rm field}(t) & \text{for } t < t_{\rm quench} \\ \mathrm{SFR}_{\rm field}(t_{\rm quench}) e^{\frac{-(t-t_{\rm quench})}{\tau_{\rm quench}}} & \text{for } t > t_{\rm quench}. \end{cases} \quad (10)$$

As shown in Figure 18 (left column), the three characteristics of the distribution of $\Delta\log(\psi*)$ for the mass range $M* \geq 10^{10} M_{\rm e}$ (from top to bottom: first quartile, median, and third quartile) can each be reproduced by a number of combinations of $t_{\rm delay}$ and $\tau_{\rm quench}$. However, the topology of the quantity $Q(t_{\rm quench}, t_{\rm delay})$ shown in the top left panel of Figure 20 shows that only a very limited region of parameter space around $\tau_{\rm quench} = 0.5$ Gyr and $t_{\rm delay} = 2.5$ Gyr provides a good fit to all three characteristics simultaneously ($Q = 0.83$). Nevertheless, for this very narrow range of parameter space, the top panel of Figure 18 illustrates that these parameters provide a good fit not only of the characteristics but also of the distribution of $\Delta\log(\psi*)$ as a whole.

For the stellar mass range $10^{9.5} M_\odot \leq M_* < 10^{10} M_\odot$ Figure 20 (bottom left panel) shows the parameter space conducive to a simultaneous recovery of all three characteristics to be similarly limited as for the high stellar mass range. For the low-mass range, however, the preferred parameter values are $\tau_{\rm quench} = 0.5$ Gyr and $t_{\rm delay} = 2.9$ Gyr, i.e., while the preferred quenching timescale is the same, the preferred delay time before the onset of star formation quenching is slightly longer than for high-mass galaxies. As for the high stellar mass range, the preferred parameters provide a good fit to the full $\Delta\log(\psi*)$ distribution.

Overall, the "delayed quenching" model provides a good approximation of the observed distribution over the full range in stellar mass. However, the ranges in $t_{\rm delay}$ and $\tau_{\rm quench}$ for which all three characteristics can be reproduced are extremely narrow, with the solution being largely trivial, as the preferred delay time corresponds to a significant fraction (or even the whole) of the satellite lifetime for a large fraction of the model group galaxies.

8.2.2. The "Stochastic Delayed Quenching" Model

The second two-parameter model, referred to as the "stochastic delayed quenching" model, expands on the first by replacing the fixed delay time with a probability per unit time $P_{\rm quench}$ that gradual quenching of the SFR of the galaxy begins, i.e. a galaxy becoming a satellite at time $t_{\rm infall}$ continues to form stars as if it were still a field (central) galaxy. However, with a probability $P_{\rm quench}$, the SFR of the galaxy begins an exponential decline on a decay timescale of $\tau_{\rm quench}$. As such, the functional form of the time dependence of the SFR is identical to that given in Equation (10), with the difference lying in the stochastically determined delay time.

As shown in the middle panels of Figure 20, the parameter space conducive to a simultaneous recovery of all three characteristics is very limited, with this only being possible in the vicinity of $\tau_{\rm quench} = 0.9$ Gyr and $P_{\rm quench} = 0.3\,\mathrm{Gyr}^{-1}$ for the stellar mass range $M* \geq 10^{10} M_{\rm e}$, and for $\tau_{\rm quench} = 1.5$ Gyr and $P_{\rm quench} = 0.3$ Gyr in the low stellar mass range. As shown in the top panels of Figures 18 and 19, these parameters recover not only the three characteristics but also the distribution of $\Delta\log(\psi*)$ as a whole. However, the values of Q in both stellar mass ranges are lower than those achieved by the delayed quenching model, indicative of a poorer recovery of the distributions (see Table 5).

An important feature of the "stochastic delayed quenching" model is highlighted by the second, third, and fourth panels from the top in Figures 18 and 19. Considering the distributions of Δq_i for all three characteristics shown in these panels, it is apparent that the preferred solution becomes degenerate in $P_{\rm quench}$ for $P_{\rm quench} \gtrsim 1.5\,\mathrm{Gyr}^{-1}$. This results from the fact that at and above this frequency nearly every modeled infalling galaxy will experience a quenching event. Conversely, at the preferred value of $P_{\rm quench} \approx 0.3\,\mathrm{Gyr}^{-1}$, a sizable fraction ($\gtrsim$50%) of the infalling population does not experience a quenching event. Overall, therefore, although the stochastic delayed quenching model is capable of closely reproducing the observed distributions of $\Delta\log(\psi*)$, the solution is largely trivial.

8.2.3. The "Refueling" Model

The final two-parameter model is referred to simply as the "refueling" model. In this model, a galaxy becoming a satellite at time $t_{\rm infall}$ continues to form stars as if it were still a field (central) galaxy. With a probability per unit time $P_{\rm quench}$ the SFR of the galaxy is instantaneously completely shut off at a time $t_{\rm quench}$ with $t_{\rm infall} < t_{\rm quench}$, followed by an inversely exponential recovery to the level it would have had as a field galaxy on a timescale $\tau_{\rm fuel}$. Unlike the other models with a quenching probability, where although the occurrence of the instantaneous or gradual quenching was stochastic it could only take place once, in the refueling model we include the possibility of multiple such events as illustrated in Figure 15, i.e., this model explicitly includes a resuscitation of previously quenched star formation, and the evolution of the SFR is given by

$$\mathrm{SFR}(t) = \begin{cases} \mathrm{SFR}_{\rm field}(t) & \text{for } t < t_{\rm quench,1} \\ \mathrm{SFR}_{\rm field}(t)\left(1 - e^{\frac{-(t-t_{\rm quench,i})}{\tau_{\rm quench}}}\right) & \text{for } t > t_{\rm quench,i},\ \forall i. \end{cases} \quad (11)$$

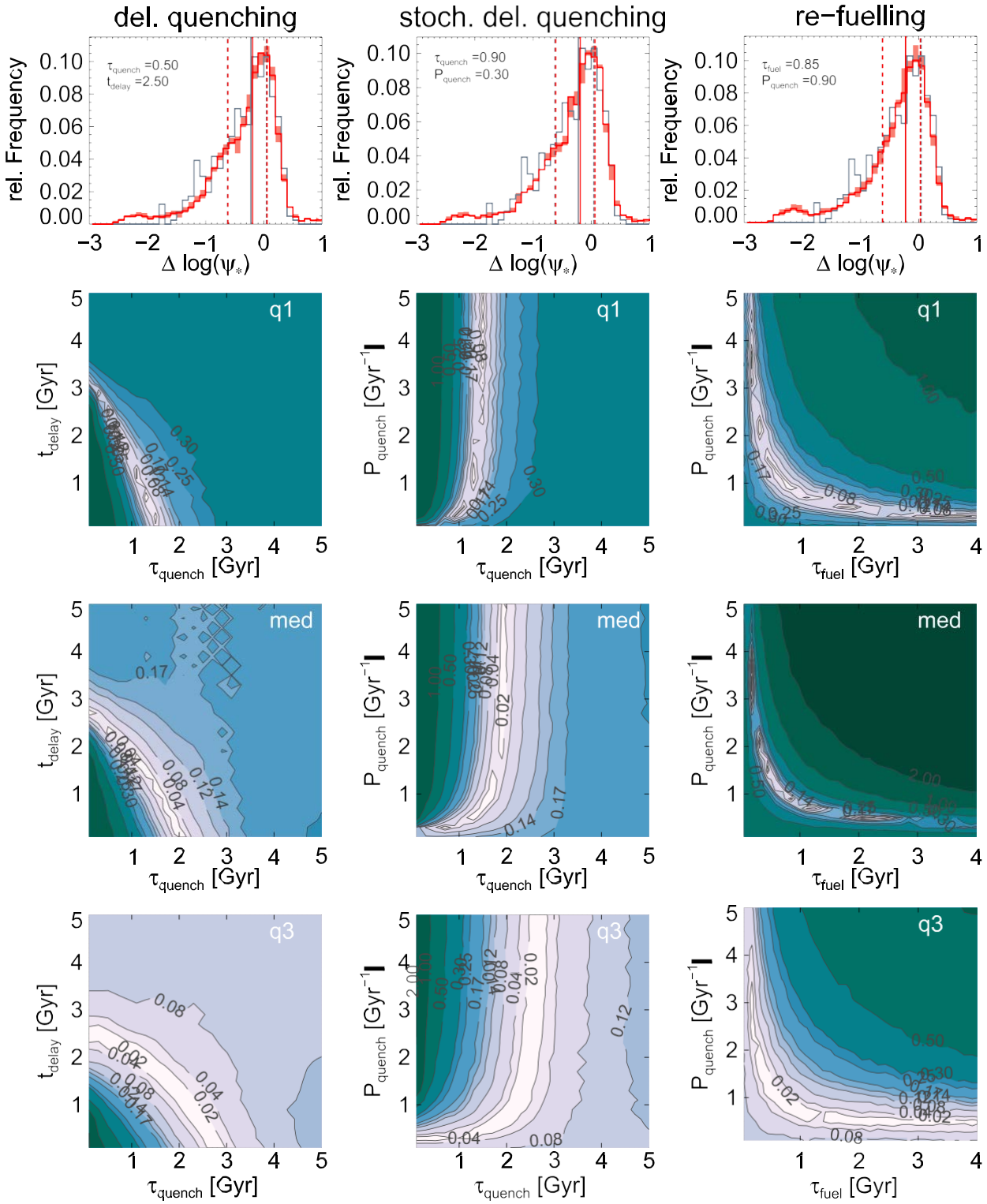

Figure 18. Performance of the family of two-parameter models (the delayed quenching model, the stochastic delayed quenching model, and the refueling model, from left to right) in the stellar mass range $M* \square 10^{10} M_e$. Top: observed distribution of Δlog(ψ*) in gray, with the three characteristics of the observed distribution (the second quartile, the median, and the third quartile) depicted as vertical gray dashed, solid, and dot-dashed lines, respectively. The average of 50 realizations of the model with the parameter values listed at top left (chosen to provide the best simultaneous fit to the three characteristics as determined using Q_m in Figure 20) is overplotted in red, with the three characteristics of the model distribution indicated by vertical red lines (of the same line style). The red shaded region shows the range between the 16th and 84th percentiles in each bin of Δlog(ψ*) as found from 50 realizations of the model. Second from top: topology Δq_1. The color coding of the contours goes from dark green via blue to white for decreasing values of Δq_1. Third from top: as for the panel above, but for Δq_2. Bottom: as for the two panels above, but for Δq_3.

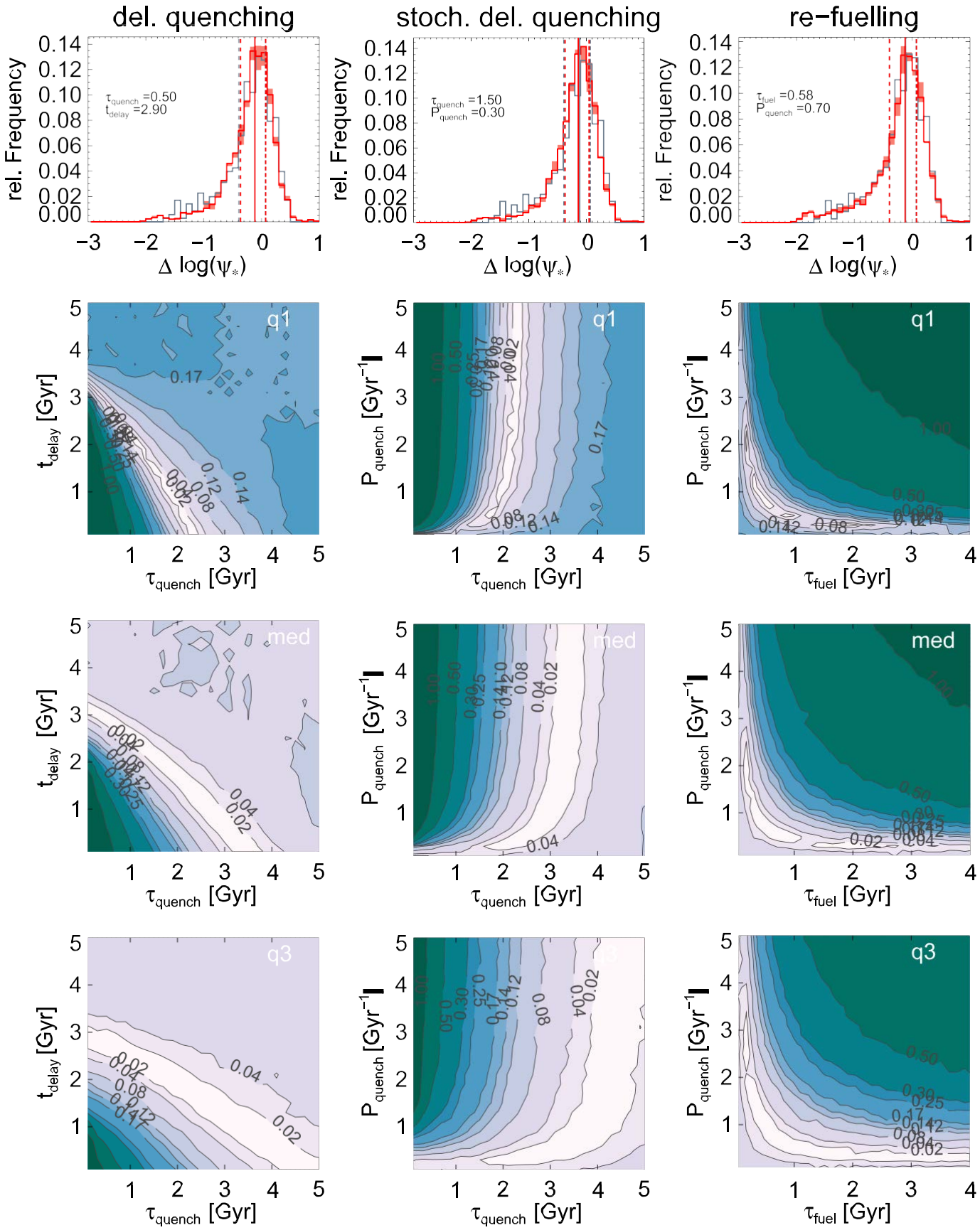

Figure 19. Same as Figure 18, but for the mass range $10^{9.5}\,M_{\rm e}$ □ $M*$ < $10^{10}\,M_{\rm e}$.

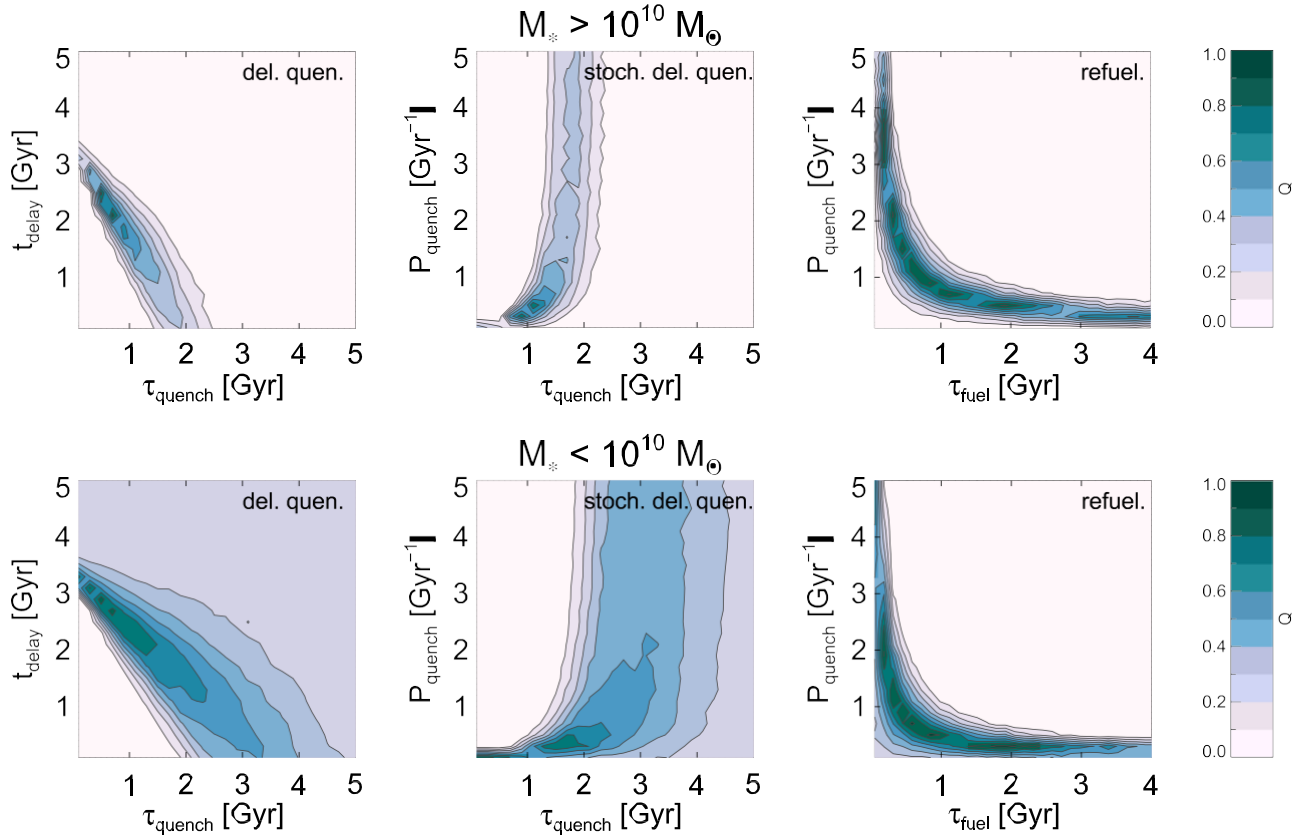

Figure 20. Figure of merit $Q(p_1, p_2)$ indicating the ability of the two-parameter model to simultaneously recover all three characteristics (first quartile, median, third quartile) as a function of both parameters. $0 \leq Q \leq 1$, with 1 corresponding to a perfect simultaneous recovery. The top row shows the results in the high stellar mass range $M* > 10^{10}\,M_e$, while the bottom row shows those for the low stellar mass range $10^{9.5}\,M_e \leq M* \leq 10^{10}\,M_e$. From left to right the columns show the results for the delayed quenching model, the stochastic delayed quenching model, and the refueling model.

As shown in the right column of Figure 20, the refueling model can simultaneously reproduce the three characteristics of the $\Delta\log(\psi*)$ distribution for a wide range of values for the parameters τ_{fuel} and P_{quench} in both the ranges of stellar mass considered. Furthermore, the refueling model achieves values of Q higher than the other two-parameter models in both stellar mass ranges ($Q \geq 0.92$; see Table 5), indicative of a better simultaneous recovery of the observed distribution of $\Delta\log(\psi*)$.

For the high stellar mass range, the preferred parameter values are $\tau_{fuel} = 0.85$ Gyr and $P_{quench} = 0.9\,\mathrm{Gyr}^{-1}$, with these values also providing a good fit to the distribution of $\Delta\log(\psi*)$ as a whole, as shown in the top right panel of Figure 18. However, unlike for the other two-parameter models, there is a pronounced degeneracy between the model parameters, with the models with $\tau_{fuel} = 1.9$ Gyr and $P_{quench} = 0.5\,\mathrm{Gyr}^{-1}$ and those with $\tau_{fuel} = 0.3$ Gyr and $P_{quench} = 2.1\,\mathrm{Gyr}^{-1}$ also performing similarly well.

For the low stellar mass range the results are qualitatively similar (as shown in Figures 19 and 20), albeit with preferred values of $\tau_{fuel} = 0.58$ Gyr and $P_{quench} = 0.7\,\mathrm{Gyr}^{-1}$. Overall, the refueling model is capable of closely reproducing the observed distributions of $\Delta\log(\psi*)$ for a wide range of parameter values, common to both ranges of stellar mass. Finally, it also remains to be noted that the majority of these solutions are nontrivial, as for the higher values of P_{quench} the majority of the model satellites experience at least one quenching and refueling cycle.

In summary, we thus find that all three two-parameter models considered can reproduce the observed distributions of $\Delta\log(\psi*)$, although the refueling model performs best. Independent of the chosen SFH model, however, we find a prolonged (or indefinite) period of star formation at the level of a comparable field galaxy while already a satellite to be required in order to recover the observed distributions.

9. Implications for the Gas Fueling of Satellite Spiral Galaxies

In the previous sections we have presented a detailed empirical analysis of the star formation in satellite spiral/disk galaxies considering the distributions of sSFR and $\Delta\log(\psi*)$. Making use of simple models for the SFHs of satellite spiral galaxies, we have shown that the empirical distributions of $\Delta\log(\psi*)$ favor SFHs for satellite spirals with extended periods of star formation at the level of comparable field spiral galaxies and rapid quenching of star formation and a rapid recovery of star formation, respectively. In the following we will consider the implications of these findings in the context of the gas cycle of spiral satellite galaxies and use them to broadly constrain the gas fueling of these objects. We begin by outlining our methodology, followed by a derivation of estimates for the in- an outflows in the context of our model SFHs. Finally, we discuss the implications of our results with respect to the reservoirs from which gas fueling can potentially be sourced.

Table 5
Summary of Preferred Model Parameter Values for Two-parameter Models

t_{infall} Dist.	$M*$ Range	Del. Q.			Stoch. Del. Q.			Refuel.		
		t_{delay} (Gyr)	τ_{quench} (Gyr)	Q	P_{quench} (Gyr^{-1})	τ_{quench} (Gyr)	Q	P_{quench} (Gyr^{-1})	τ_{fuel} (Gyr)	Q
Con.	$M* < 10^{10}\,M_e$	2.9	0.5	0.87	0.3	1.5	0.79	0.7	0.58	0.93
	$M* \geq 10^{10}\,M_e$	2.5	0.5	0.83	0.3	0.9	0.78	0.9	0.85	0.92
Full	$M* < 10^{10}\,M_e$	4.7	3.7	0.63	0.1	3.1	0.71	0.5	0.45	0.79
	$M* \geq 10^{10}\,M_e$	4.9	1.5	0.75	0.1	1.5	0.84	0.98	0.5	0.92

Note. Preferred parameter values and associated figure of merit Q for the delayed quenching model (Del. Q.), the stochastic delayed quenching model (Stoch. Del. Q.), and the refueling model (Refuel.) in both disjoint ranges of stellar mass considered. Values are supplied for the conservative infall time distribution (Con.; see Section 8, Appendix C, and Figure 24) and for the full distribution (Full; see Section 9.2.4 and Appendix C).

9.1. Constraining the Gas Cycle

To obtain broad quantitative constraints on the flows of gas into and out of the ISM, we will make use of the equations describing the gas cycle of galaxies. Here we present an overview of our methodology, while a full detailed derivation and discussion are supplied in Appendix D.

In a general form, the ISM gas content of a galaxy and its time dependent evolution can be expressed as

$$\dot{M}_{\rm ISM} = \dot{M}_{\rm in} - \dot{M}_{\rm out} - (1-a)\,\Psi_*, \quad (12)$$

where $\dot{M}_{\rm in}$ is the inflow rate of gas into the ISM of the galaxy, $\dot{M}_{\rm out}$ is the outflow rate of gas from the ISM of the galaxy, Ψ_* is the current SFR, and α is a positive constant less than unity that accounts for the recycling of gas from high-mass stars back into the ISM (as detailed in Appendix C, $\alpha = 0.3$ throughout). Assuming a volumetric star formation law

$$\Psi_* = k M_{\rm ISM} \quad (13)$$

following Krumholz et al. (2012), and that the outflow rate can be reexpressed in terms of the ISM content and a typical residence time τ_{res} of a unit mass of gas in the ISM,[45] Equation (12) can be written as

$$\dot{M}_{\rm ISM} = \dot{M}_{\rm in} - \frac{M_{\rm ISM}}{t_{\rm res}} - (1-a)\,k M_{\rm ISM}$$

$$= \dot{M}_{\rm in} - \frac{M_{\rm ISM}}{t_{\rm res}} - k M_{\rm ISM}. \quad (14)$$

Given that $\kappa = 1/\tau_{exhaust}$, where $\tau_{exhaust}$ corresponds to the exhaustion timescale of the ISM in a closed box model, Equation (14) can be reformulated and simplified as

$$\dot{M}_{\rm ISM} = \dot{M}_{\rm in} - \frac{M_{\rm ISM}}{\tilde{t}} \quad (15)$$

using an effective timescale $\tilde{t} = t_{\rm res} t_{\rm exhaust} / (t_{\rm res} + t_{\rm exhaust})$. For our analysis, we assume that t_{res} as well as k, and as such $t_{exhaust}$, are set by galaxy specific processes alone, i.e., are independent of environment. As detailed in Appendix D, the latter quantity has been individually calibrated for both stellar mass ranges considered in our analysis using the model of Popping et al. (2014) and our median $\psi*$–$M*$ relation for the FIELDGALAXY sample.

For spiral galaxies in the field, the SFR is found to evolve only very slowly with redshift and is thought to be determined by a very gradually evolving self-regulated balance between inflow, outflow, and consumption of ISM via star formation (e.g., Kereš et al. 2005; Davé et al. 2011; Lilly et al. 2013; Saintonge et al. 2013) such that at any given time their SFR can be considered quasi-constant. As we show in detail in Appendix D, this quasi-steady state allows an estimate of the inflow rate to be derived as

$$\dot{M}_{\rm in} \gg \frac{M_{\rm ISM}}{\tilde{t}} = \frac{\Psi_*}{k\tilde{t}}, \quad (16)$$

given knowledge of the effective timescale $\tilde{t}$ and the SFR.[46] As shown in Appendix D, the corresponding outflow rate in the steady state can then be estimated as

$$\frac{\dot{M}_{\rm out}}{\Psi_*} = \frac{1}{k\tilde{t}} - (1-a) = \frac{\dot{M}_{\rm in}}{\Psi_*} - (1-a), \quad (17)$$

where $\dot{M}_{\rm in}$ is determined using Equation (16). This approximation will hold as long as the rate at which the inflow changes is small compared to the timescale $\tilde{t}$. As discussed in Appendix D, the deduced values for $\tilde{t}$ are $\sim$1 Gyr, retroactively justifying our use of this approximation.

As the volumetric star formation law—Equation (13)—linearly couples the SFR and ISM mass (at a given stellar mass), in the following we will proceed by identifying solutions of Equation (15) that correspond to the parameterized SFH of the models and directly interpret the preferred values of the model parameters identified in Section 8.2 in terms of mass flows into and out of the ISM. Specifically, we make use of the evolution of the SFR during the quenching and refueling phases of the two-parameter models to constrain $\tilde{t}$, enabling us to use Equation (16) to estimate the value of $\dot{M}_{\rm in}$ required during the prolonged periods of star formation activity comparable to that of field galaxies observed for all these models.

At this point, we note that we will take the term $\dot{M}_{\rm in}$ to represent a pure inflow term, i.e., mass coming into the ISM from outside of the volume of the galaxy occupied by its stellar component. In reality, the ISM of a galaxy will also be fueled by the mass loss from evolved intermediate- and low-mass stars (e.g., TP-AGB stars) not included in the definition of κ. For the Milky Way bulge, where the mass return is dominated by these evolved stars, studies find stellar mass normalized mass return rates of $\sim(10^{11})\,{\rm yr}^{-1}$ (e.g., Ojha et al. 2007). Comparing this to the sSFR of even the higher stellar mass galaxies (i.e., those with a larger old stellar component), one finds that the mass return rate that must be considered is likely $\sim$10% of the

[45] We note that this formulation is equivalent to the widely used mass-loading approximation for parameterizing outflows.

[46] We note that the estimate of the inflow rate given by Equation (16) represents a conservative estimate in our derived framework.

Table 6
Summary of Estimated In- and Outflow Rates

Model	$t_{\rm infall}$ Dist.	Inflow ($\dot{M}_{\rm in}$/SFR)		Outflow ($\dot{M}_{\rm out}$/SFR)	
		$M* < 10^{10}\,M_e$	$M* > 10^{10}\,M_e$	$M* < 10^{10}\,M_e$	$M* > 10^{10}\,M_e$
Del. Q.	Con.	4.56	4.46	3.86	3.76
	Full	L[a]	1.43	L[a]	0.73
Stoch. Del. Q.	Con.	1.46	2.38	0.76	1.68
	Full	L[a]	1.43	L[a]	0.73
Refuel.	Con.	3.78	2.52	3.08	1.82
	Full	4.87	2.18	4.17	1.48

Note. Inflow and corresponding outflow rates as multiples of the SFR for the delayed quenching model (Del. Q.), the stochastic delayed quenching model (Stoch. Del. Q.), and the refueling model (Refuel), as determined under a quasi-steady-state assumption following Equations (16) and (17), as detailed in Sections 9.2.1–9.2.3. Both the conservative distribution of infall times (Con.; see Section 8, Appendix C, and Figure 24) and the full distribution (full; see Appendix C) are considered. In- and outflows have been estimated separately for the stellar mass ranges $10^{9.5}M_e \leq M* < 10^{10}M_e$ and $M* \geq 10^{10}M_e$.
[a] Assumption that quenching timescale is short w.r.t rate of change of inflow violated. Estimate not possible.

observed sSFR. In the following, we have therefore chosen to ignore this contribution, but will return to and justify this choice later.

9.2. Estimates of In- and Outflows

In the following we present the results of applying the approach to constraining the gas cycle outlined above to the two-parameter model family. The estimated in- and outflow rates for each model are listed in Table 6.

9.2.1. The Delayed Quenching Model

Inserting the SFH of the delayed quenching model into Equation (13), we find

$$M_{\rm ISM}(t) = \begin{cases} M_{\rm ISM,field}(t) & \text{for } t < t_{\rm quench} \\ M_{\rm ISM,field}(t_{\rm quench})\,e^{\frac{-(t-t_{\rm quench})}{t_{\rm quench}}} & \text{for } t > t_{\rm quench}, \end{cases} \quad (18)$$

corresponding to the balance between inflow, outflow, and consumption of the ISM via star formation—assumed to be in place for field galaxies—being maintained upon infall of a galaxy for the time $t_{\rm delay}$ until $t = t_{\rm quench}$, followed by an exponential decline of the ISM mass. Solving Equation (15) for this scenario, i.e., with the inflow being cut off for $t > t_{\rm quench}$ ($\dot{M}_{\rm in}(t > t_{\rm quench}) = 0$), we find a solution of the form

$$M_{\rm ISM}(t > t_{\rm quench}) = M_{\rm ISM}(t = t_{\rm quench})\,e^{-\left(\frac{t-t_{\rm quench}}{\tau}\right)}. \quad (19)$$

With the balance between inflow, outflow, and consumption of ISM being maintained as for a corresponding field galaxy while $t_{\rm infall} < t \leq t_{\rm infall}$, we can identify $M_{\rm ISM}(t) = M_{\rm ISM,field}(t)$ "$t \in (t_{\rm infall}, t_{\rm quench}]$. Comparing Equations (19) and (18), we can then immediately identify

$$\tau = t_{\rm quench}. \quad (20)$$

Inserting Equation (20) into Equation (16), we can estimate the rate of inflow from our observations. As previously, we consider the stellar mass ranges $10^{9.5}M_e \leq M* < 10^{10}M_e$ and $M* \geq 10^{10}M_e$ separately. In this fashion, we thus estimate an inflow rate of 4.46 (4.56) times the SFR for the high (low) stellar mass range and find a corresponding outflow of 3.76 (3.86) times the SFR. The estimated in- and outflows are listed in Table 6.

9.2.2. The Stochastic Delayed Quenching Model

The basic functional form of the stochastic delayed quenching model corresponds to that of the delayed quenching model as discussed above, with the only difference being that the fixed delay time $t_{\rm delay}$ is replaced by a probability per unit time that quenching occurs $P_{\rm quench}$. Accordingly, we estimate the in- and outflows based on the preferred parameter values as for the delayed quenching model, finding a required inflow of 2.38 (1.46) times the SFR in the high (low) stellar mass range and a corresponding outflow of 1.68 (0.76) times the SFR as listed in Table 6.

As previously discussed, for the stochastic delayed quenching model we find the preferred solution for each characteristic to become degenerate in $P_{\rm quench}$ for $P_{\rm quench} \geq 1.5\,{\rm Gyr}^{-1}$. As argued above, for the preferred value of $P_{\rm quench} = 0.3\,{\rm Gyr}^{-1}$ (for both stellar mass ranges) this implies that ≥50% of the infalling population does not experience a quenching event and hence must continue to maintain the balance between inflow, outflow, and star formation at the level of a comparable field galaxy over their entire satellite lifetime. In turn, this enables us to interpret the preferred value of $P_{\rm quench}$ in terms of an effective requirement on the duration of the extended period of star formation for satellite galaxies in the group environment. Based on the value of $P_{\rm quench} = 0.3\,{\rm Gyr}^{-1}$ and using the extremely conservative distribution of infall times adopted in our modeling, we find that 30% (20%, 10%) of the satellite galaxies have resided in the group environment without quenching for ≥2 Gyr (≥2.5 Gyr, ≥3 Gyr).

9.2.3. The Refueling Model

As for the delayed quenching model, we insert the SFH embodied by the refueling model—Equation (11)—in Equation (13), finding the refueling model to correspond to a case in which the assumed balance between inflow, outflow, and star formation is initially maintained by galaxies upon becoming satellites, albeit with a probability per unit time $P_{\rm quench}$ that at least a large fraction of the ISM of the galaxy is quasi-instantaneously removed. However, even with the occurrence of a quenching event, the inflow continues as

for a comparable field galaxy, so that the self-regulated balance eventually reinstates itself. Solving Equation (15) for these boundary conditions, i.e., $\dot{M}_{\rm in} = {\rm const.}$[47] and $M_{\rm ISM}(t_{{\rm quench},i}) = 0\ \forall\ i$, we find a solution of the form

$$M_{\rm ISM}(t > t_{{\rm quench},i}) = \dot{M}_{\rm in}\tilde{t}\left(1 - e^{\frac{-(t-t_{{\rm quench},i})}{\tilde{t}}}\right), \quad (21)$$

where we have identified $M_{\rm ISM,field} = \dot{M}_{\rm in}\tilde{t}$ by making use of the special case of the occurrence of only a single quenching event and taking the limit $t \to t_{\rm quench,1}$.

This enables us to identify $\tilde{t} = t_{\rm fuel}$, and we make use of Equations (16) and (17) to estimate the in- and outflow rates for both mass ranges, finding an estimated inflow of 2.52 (3.78) times the SFR and an associated outflow of 1.82 (3.08) times the SFR for the high (low) stellar mass range, as listed in Table 6.

In summary, for all our disparate models, we find a requirement of a rapid cycle of gas into and out of the ISM, with inflow rates well in excess of the SFR (ranging up to ≈3 times the SFR), accompanied by similarly high outflow rates. Comparing these inflow rates with the estimate of the mass return rate from evolved intermediate- and low-mass stars of ≈10% of the SFR, we see that ignoring their contribution to the fueling is retroactively justified for all models considered.[48]

9.2.4. Dependence on the Choice of Infall Time Distribution

In considering the implications of the preferred parameters of our models in terms of the gas flows in satellite spiral/disk-dominated galaxies, we have adopted an extremely conservative assumption concerning the distribution of infall times, i.e., that *only* the youngest satellites retain a spiral morphology. The other possible extreme assumption on the distribution of infall times is to sample the full distribution, assuming that the time spent in the group environment does not influence the probability of the morphological transformation of a galaxy. This is almost certainly not the case. Instead, the true distribution of infall times will fall somewhere between these two extremes.

The results of adopting the latter extreme distribution of infall times are shown in Figures 25 and 26 in Appendix E, with the composite figure of merit Q shown in Figure 27 (the preferred parameter values and associated figure of merit for each model are listed in Table 5). In the high stellar mass range, all three models are formally capable of reproducing the observed distribution of $\Delta\log(\psi*)$. However, while the refueling model (unsurprisingly) favors parameters comparable to those previously found ($\tau_{\rm fuel}$ = 0.98 Gyr, $P_{\rm quench}$ = 0.5 Gyr^{-1}) and achieves Q = 0.92, comparable to that previously obtained, the delayed quenching model and the stochastic delayed quenching model favor a longer quenching timescale ($\tau_{\rm quench}$ = 1.5 Gyr in both models), as well as longer delay times (4.9 Gyr) and lower quenching probabilities (0.1 Gyr^{-1}). While the stochastic delayed quenching model performs as previously in terms of recovering the distribution and characteristics, even achieving a higher value of Q, the performance of the delayed quenching model is considerably worse, only attaining Q = 0.75. In terms of required inflow rates, the preferred parameter values imply a rate of 1.43 times the SFR for the delayed and stochastic delayed quenching models and a rate of 2.18 times the SFR for the refueling model, as listed in Table 6. Again, it is immediately apparent that these inflow rates cannot be supported by mass return from evolved intermediate- and low-mass stars, hence justifying the treatment of $M_{\rm in}$ as a pure inflow.

In the low stellar mass range, the models struggle to reproduce the observed distribution of $\Delta\log(\psi*)$ (see Figure 27). Of the three models, only the refueling model reasonably recovers the observed distribution, achieving a value of Q = 0.79, compared to Q = 0.63 and Q = 0.71 for the delayed and stochastic delayed quenching models, respectively. The preferred parameter values for the refueling model are $\tau_{\rm fuel}$ = 0.45 Gyr and $P_{\rm quench}$ = 0.5 Gyr^{-1}, again comparable to those previously obtained. Both the delayed quenching model and the stochastic delayed quenching model, on the other hand, overpredict the relative number of largely unquenched galaxies and, in the case of the delayed quenching model, markedly underpredict the number of strongly quenched galaxies, i.e., both fail to recover the observed distribution. This is a result of the long preferred quenching timescales of $\tau_{\rm quench}$ = 3.1 Gyr and $\tau_{\rm quench}$ = 3.7 Gyr (for the stochastic delayed and delayed quenching models, respectively), as well as of the low quenching probability $P_{\rm quench}$ = 0.1 Gyr^{-1} and the long delay time $t_{\rm delay}$ = 4.3 Gyr—driven by the large peak of unquenched galaxies—which result in the satellite galaxy population largely mimicking the evolution of a comparable field galaxy. Furthermore, these delay timescales are longer than the previously discussed gas exhaustion timescales.

Converting the preferred model parameters into in- and outflow rates for the refueling model, one obtains a required inflow rate of 4.87 times the SFR with a corresponding outflow of 4.17 times the SFR. For the delayed quenching models, however, the basic requirement that the timescale on which the inflow rate changes be large compared to $\tau_{\rm res}$ and $\tau_{\rm SF}$ is violated, making an estimate of the inflow rate using Equation (16) unreliable.

Overall, we thus find our result of a rapid cycle of gas into and out of the ISM with inflow rates in excess of the SFR to be upheld even under the assumption of the opposite extreme infall time distribution, lending confidence that this finding is robust w.r.t the actual infall time distribution.

9.3. Sources for Replenishment

In general, we find the observed distributions of $\Delta\log(\psi*)$ for satellite spiral/disk-dominated galaxies to imply that, upon becoming satellites, these objects must experience star formation at the level of comparable field galaxies for prolonged periods (several gigayears) if not continuously. In turn, this requires a replenishment of the ISM consumed by star formation, naturally raising the question as to the nature of the gas reservoir from which the replenishment is fueled. In particular, we wish to establish whether the reservoir can be entirely composed of gas associated with the galaxy upon infall, i.e., the ISM and the more loosely bound CGM, or must instead/also be sourced from the IHM of the galaxy group. As mechanisms to replenish the HI reservoirs of galaxies from ionized hydrogen have been put forward (e.g., Hopkins et al.

[47] In this derivation we at all times assume the rate of change of the inflow to be small compared to the other timescales (quenching and replenishment) involved, and we treat $\dot{M}_{\rm in}$ as (quasi-)constant.

[48] Even when considering the total gas return rate from stellar populations, i.e., including the contribution from short-lived stars absorbed in the value of κ, this rate is generally found to be at most several tens of percent of the SFR, both for young lower-mass galaxies, such as the LMC and SMC (Matsuura et al. 2009, 2013), and for more massive and mature spiral galaxies (Tielens 2005), and thus well shy of the required fueling rates.

2008), we include the dominant ionized component of the CGM in our considerations. For the ISM, where the mass fraction of ionized gas is generally found to be □10% in spiral galaxies such as those in our sample, we consider the cold/neutral gas mass as representative of the total ISM mass.

9.3.1. Gas Associated with the Galaxy upon Infall

We begin by considering the gas associated with the galaxy at the time it first became a satellite as a possible reservoir from which the observed ongoing star formation might be fueled. This reservoir consists of the ISM of the galaxy, distributed on scales of ~10 kpc, as well as of the more loosely bound CGM. Recent work on the CGM of isolated typical L^* galaxies out to $z = 0.35$ has found that it may contain a gas mass comparable to the stellar mass of the galaxy within a physical radius of 150 kpc (e.g., Tumlinson et al. 2011, 2013), with 1%–10% of this gas being cold neutral and/or molecular hydrogen.

Based on our results, we rule out the ISM of the galaxy upon infall as the sole reservoir of fuel for star formation. All disparate models that recover the observed distributions of sSFR require strong flows of gas both into and out of the ISM (see Table 6). These findings are in conflict with the ISM being the only source of fuel, because the outflows reduce the residence timescale of the ISM to around 1 Gyr, and because in any case the models require inflows originating exterior to the ISM. Furthermore, if the ISM were the only reservoir of fuel for star formation, the Schmidt–Kennicutt relation would lead one to expect a gradual decline of the SFR, beginning upon a galaxy becoming a satellite. Such an SFH, however, would correspond to the infall quenching model rejected in Section 8.1, and not to the preferred two-parameter models.

Although our empirical results favor significant flows of gas into and out of the ISM, it is possible that these outflows remain bound to the galaxy, i.e., have their end point in the CGM, and can be recycled into the ISM at a later time. Accordingly, we consider the ability of the combined ISM and CGM to support the required star formation, initially assuming all gas to remain bound, and the complete CGM and ISM to be retained upon infall. To this end, we begin by comparing the stellar mass growth of the satellite galaxies during the period of ongoing star formation to the expected total ISM and CGM mass at infall, again distinguishing between the low and high stellar mass ranges. To estimate the stellar mass growth, we consider our fiducial galaxies with $M* = 10^{9.75} M_e$ and $M* = 10^{10.3} M_e$ and assume an SFR for these galaxies based on the y_*–M_* relation defined using the FIELDGALAXY sample. We can then estimate their stellar mass growth over the period of a characteristic delay time by evolving the galaxies backward in time as detailed in Appendix C. For the purposes of this estimate we conservatively adopt a delay time of 2.5 Gyr as a fiducial time for sustained star formation at the level of a field galaxy. This time corresponds to the shortest fixed delay time preferred by the models considered.

Estimating the stellar mass growth in this fashion, we find the lower stellar mass galaxy to have increased its stellar mass by $2.2 \times 10^9 M_e$ (80%; $M_{*,\mathrm{infall}} = 10^{9.45} M_\odot$) over the 2.5 Gyr prior to observation and the stellar mass of the higher stellar mass galaxy to have increased by $5.4 \times 10^9 M_e$ (37%; $M_{*,\mathrm{infall}} = 10^{10.17} M_\odot$).

As current satellite galaxies first became satellites at an earlier time (corresponding to a higher redshift) when galaxies were relatively more gas rich, the initial mass of the ISM upon infall may have been larger than that still present at the redshift of observation. In fact, recent work modeling the evolution of the total gas fraction of star-forming disk galaxies indicates that the total (cold) gas fraction $f_{gas} = (M_{\mathrm{HI}} + M_{\mathrm{H_2}})/(M_{\mathrm{HI}} + M_{\mathrm{H_2}} + M_*)$ was ~1.5 times greater at $z \sim 0.5$ than at $z = 0$ (Lagos et al. 2011; Popping et al. 2014) for a given stellar mass.[49] Following Popping et al. (2014),[50] we estimate an ISM mass of $2.1 \times 10^9 M_e$ ($0.75 \times M_{*,\mathrm{infall}}$) for the low stellar mass galaxy at infall and a mass of $5.3 \times 10^9 M_e$ ($0.36 \times M_{*,\mathrm{infall}}$) for the ISM of the high stellar mass galaxy. Combined with an estimate of the CGM mass at infall being equal to the stellar mass at that epoch, we thus estimate a total reservoir mass at infall of $5 \times 10^9 M_e$ and $2 \times 10^{10} M_e$ in the low and high stellar mass case, respectively. Contrasting these masses with the stellar mass growth, we find that 41% and 27%, respectively, of the gas associated with the galaxy at infall would be required to fuel the stellar mass growth, making fueling of the required star formation from the joint ISM and CGM at infall a seemingly feasible proposition.

In this estimation we have assumed that the outflows from the ISM remain bound to the galaxy in their entirety. However, at least of order 10% of outflows from the ISM of the galaxy are likely to be unbound and escape (e.g., Loeb 2008). Taking this additional mass loss into consideration, i.e., assuming that 10% of the outflows from the galaxy are lost and making use of the ratios of outflow to SFR as determined from our models and listed in Table 6, we find that in the low stellar mass range 49%–69% of the combined CGM and ISM must be retained in order to replenish the mass loss due to star formation and outflows, while for the high stellar mass range the figure is 33%–41%. Nevertheless, it thus appears potentially feasible that the mass of gas associated with the galaxy at infall is sufficient to support the required inflows, outflows, and star formation, provided that it can be retained and can cool efficiently.

9.3.2. Stripping and Dependence on Galaxy Mass/Subhalo Mass

Our previous estimate that the gas initially bound to the galaxy at infall in the form of the CGM, as well as the ISM cycled into the CGM as a result of outflows, suffices to support the observed ongoing star formation is predicated on this diffuse component of gas, distributed over scales of ~100 kpc, remaining bound to the galaxy upon its becoming a satellite, i.e., falling into the more massive DMH of another galaxy/galaxy group. Thus, the question arises to what extent this extended diffuse reservoir of gas can be retained when the galaxy to which it is initially bound is moving relative to the pressurized diffuse IHM of the satellite spiral's host galaxy group, i.e., to what extent ram pressure and/or tidal stripping will unbind and remove this gas reservoir.

We begin by addressing this question empirically, making use of the observed distributions of $\Delta\log(\psi*)$. As we have shown in Section 8, these are only weakly dependent on the mass of the galaxy, with, if anything, stronger effects observed in higher-mass galaxies. As the ability of a galaxy to retain gas

[49] While the evolution of the total cold gas fraction is mild, Popping et al. (2014) predict the molecular gas fraction to evolve strongly with redshift, in agreement with observations (Tacconi et al. 2010; Geach et al. 2011).

[50] We make use of the total cold gas fraction as a function of stellar mass at different redshifts provided in Popping et al. (2014), interpolating between these to a redshift of $z = 0.35$.

against the effects of ram pressure stripping is expected to increase with the depth of its potential well, i.e., with its mass, one would expect higher-mass satellite spiral galaxies to be better able to retain their CGM than lower-mass galaxies. Furthermore, the probability for a low-mass system ($M_* < 10^{10} M_e$) to experience a tidal stripping encounter with a higher-mass system that can remove gas from the lower-mass partner is greater than that for a higher-mass system ($M_* > 10^{10} M_e$). As a result, if retained and recycled CGM and ISM were to constitute the main source of replenishment of the ISM, one would expect shorter delay times t_{delay} and higher quenching probabilities P_{quench} in lower-mass galaxies/subhalos than in higher-mass systems, as well as a higher rate of the occurrence of strongly quenched galaxies at lower galaxy stellar mass. In other words, one would expect the distribution of $\Delta\log(\psi_*)$ to be more strongly skewed toward low values for low stellar mass galaxies than for high stellar mass galaxies. Our empirical results, however, are completely contrary to this expectation. Comparison of the distribution of $\Delta\log(\psi_*)$ for satellite spiral galaxies and field galaxies in Figure 14 shows that the group environment actually has a stronger effect on the sSFR of higher-mass galaxies: the distributions of $\Delta\log(\psi_*)$ for low stellar mass galaxies are also less skewed toward low values of $\Delta\log(\psi_*)$ than those of higher-mass galaxies. In terms of our modeling in Section 8, this translates into delay times for low-mass galaxies that are equal to or longer than those for higher-mass galaxies, and quenching probabilities that are smaller for low-mass galaxies than for high-mass galaxies. The delay timescales (direct and implied by the quenching probabilities), moreover, are longer than the expected time to group pericentric passage (1.5–2 Gyr; Hester 2006), which is the point in the orbit at which stripping effects will be strongest. Thus, we find our empirical results to disfavor retained CGM as the dominant source for the replenishment of the ISM. At this point we reiterate that we have previously shown that our sample of spiral galaxies is mass complete and volume limited, even in the low stellar mass range (Sections 4, 5), and recovers the parent sSFR distribution well (Section 4 and Appendix A). Therefore, the empirical basis for these findings should be considered robust and physical in nature.

Further support for the findings disfavoring the CGM as the dominant reservoir is also provided by a range of theoretical work considering the ram pressure stripping of satellite galaxies in galaxy groups and clusters (e.g., Hester 2006; McCarthy et al. 2008; Bahé & McCarthy 2015). While the temperature and pressure of the diffuse IHM of the galaxy group, responsible for the ram pressure stripping, are expected to increase with group halo mass, thus enhancing the stripping, the ability of a satellite galaxy to retain its gas reservoirs is expected to increase with increasing depth of its potential well, i.e., with increasing stellar mass and DM subhalo mass. As shown by, e.g., Hester (2006), the ram pressure stripping process is not scale-free, so that the degree of stripping depends both on the ratio of satellite to group/cluster DMH mass and on the absolute DMH mass of the group/cluster.

Hester (2006) has considered the case of satellite spiral galaxies subjected to ram pressure stripping in groups and clusters of galaxies using a multicomponent semi-empirical model, finding that ram pressure stripping is expected to completely remove any extended gas halo by the first pericentric passage of the satellite (i.e., within 1.5–2 Gyr), even in the galaxy group environment with DMH masses of $\sim 10^{13} M_e$ (but see also McCarthy et al. 2008). In fact, Hester (2006) shows that depending on the mass ratio of the satellite galaxy DM subhalo and the group DMH, even the extended ISM disk of the galaxy may be partially stripped in both group and cluster environments. These predictions are also supported by recent detailed simulations presented by Bahé & McCarthy (2015).

Splitting our sample of satellite spirals into two mass ranges ($10^{9.5} M_e < M_* < 10^{10} M_e$ and $M_* > 10^{10} M_e$), we find the median dynamical masses of the galaxy groups hosting the satellite spirals to be $10^{13.4} M_e$ for the low stellar mass galaxies and $10^{13.5} M_e$ for the high stellar mass galaxies. As our fiducial galaxies with $M_* = 10^{9.75} M_e$ and $M_* = 10^{10.3} M_e$ correspond to the median stellar masses for systems in the low and high stellar mass range, respectively, we can use these stellar masses to estimate the median mass of the DM subhalos by making use of the average stellar mass–halo mass relation presented by Moster et al. (2010). This results in estimated DM subhalo masses of $10^{11.5}$ and $10^{11.9} M_e$ for the low and high stellar mass range, respectively, corresponding to logarithmic DM subhalo/group halo mass ratios of −1.9 and −1.6. For these ratios of DM subhalo to group halo mass Hester (2006) predicts that by pericentric passage, even in galaxy groups and low-mass clusters, the extended ISM disk of the galaxy will be affected by ram pressure stripping in approximately its outer third to half, with ∼50% of its total mass being stripped, in addition to the complete removal of the diffuse gaseous halo. For the low and high stellar mass ranges of our sample, the removal of the CGM alone would reduce the fraction of gas retained to 43% and 27%, respectively, i.e., below the required levels as previously estimated. Moreover, the expected outflows predicted in our models would easily suffice to cycle >50% of the ISM into the CGM within the delay time of 2.5 Gyr.

Thus, we find that the results of recent work considering the ram pressure stripping of satellite spiral galaxies in the group environment disfavor the retention of a large fraction of the diffuse CGM and recycled ISM, in line with our empirical finding. Accordingly, although the mass *at infall* of the CGM and ISM of a spiral galaxy becoming a satellite may, in principle, be sufficient to sustain the required inflow and star formation over prolonged periods of the galaxy's satellite lifetime, it seems likely that only an insufficient fraction of this reservoir can actually be retained in the group environment and contribute to the fueling of the galaxy. Accordingly, it is probable that at most part of the fuel required for the observed ongoing star formation of satellite spiral galaxies can be sourced from gas that was associated with the galaxy upon infall, with at least a significant fraction being sourced from gas not initially associated with the galaxy.

9.3.3. Replenishment from the IHM

With our empirical results disfavoring the combined CGM and ISM as the source for the inflow of gas required, instead favoring a further reservoir not associated with the galaxy, by process of elimination we conclude that our empirical analysis implies an inflow of gas from the IHM of the group into the ISM of the satellite spiral galaxy as a mechanism to meet the demands of the extended period of star formation at the level of a comparable field galaxy implied for satellite spiral galaxies. Although the exact rate of inflow from the IHM required depends on the degree to which the CGM can be retained, as

well as the fraction of ISM mass lost to winds or while being cycled through the CGM, it nevertheless appears that an inflow from the IHM of order the SFR is required, contrary to the standard paradigm.

Before discussing the physical implications, we first consider whether a possible factor to at least partially ameliorate this conclusion may lie in our simplifying assumption in our modeling that the residence time τ_{res} (i.e., the the time a unit mass of gas spends in the disk of a spiral galaxy before being expelled, introduced in Section 9 and Equation (27) of Appendix D) is independent of environment, depending only on galaxy-specific properties, in particular galaxy mass. For satellite spiral galaxies in galaxy groups, the surrounding medium may, in fact, be more pressurized than for a similar stellar mass galaxy in the field, decreasing the outflows from the satellite galaxy and increasing τ_{res}. However, if the medium surrounding the galaxy were sufficiently pressurized to fully suppress wind-driven outflows from the ISM, this medium would also act to enhance the efficiency of the removal of the CGM via ram pressure stripping (Hester 2006). As discussed in Section 9.3.2, ram pressure stripping is likely sufficient to remove not only the CGM of spiral satellite galaxies but also part of the ISM of these systems, even in groups of the mass scale considered. The resulting requirement of fueling from sources external to the ISM, most notably the IHM, is further compounded by the fact that the estimated total ISM mass associated with the galaxy upon infall is less than the increase in stellar mass over the fiducial 2.5 Gyr delay timescale for both fiducial galaxies considered, as detailed in Section 9.3.1. Nevertheless, the suppression of outflows is potentially amenable to testing by considering the metallicity of satellite spiral galaxies (e.g., Pasquali et al. 2012) and will be pursued for this sample in future work. We note, however, that, e.g., Peng & Maiolino (2014) have investigated the gas-phase metallicity of star-forming satellite and field galaxies, interpreting their results in the sense of a metal-enriched inflow onto star-forming group satellite galaxies, in agreement with our presented results.

Having identified the IHM as a plausible source of fuel to support the inflows and star formation of spiral satellite galaxies, we investigate the viability of this option, considering the IHM as the sole reservoir for the sake of argument. Making use of our group dynamical mass estimates and assuming a universal baryon mass fraction of $\Omega_b/\Omega_M = 1/6$, we can estimate the IHM mass for the galaxy groups in our sample.[51] Comparing this with the total (current) SFR associated with the member satellite spiral galaxies of each group contained in the GROUPGALAXY sample, we find that the timescale on which the IHM would be consumed by this star formation activity is □500 times the Hubble time. As, however, not only satellite spiral galaxies in the GROUPGALAXY sample will be forming stars, as a hypothetical limiting case, we also consider the total star formation of *all* member galaxies of a each group, assuming SFRs based on their stellar mass and the ψ_*–M_* relation for the FIELDGALAXY sample. Nevertheless, even in this case, the median exhaustion timescale of the IHM is □150 times the Hubble time.

[51] We equate the dynamical mass of the system to the halo mass and estimate the total baryonic mass using the universal baryon fraction. We then subtract the total stellar mass of all group members to obtain an estimate of the IHM mass.

Furthermore, numerical simulations indicate that ambient dark and baryonic matter is being accreted onto the DMHs of galaxy groups (e.g., McBride et al. 2009; van de Voort et al. 2011; Wetzel & Nagai 2015). As a result, the IHM of galaxy groups is constantly being replenished. For the galaxy groups in our sample, we estimate the inflow rate of baryons using Equation (9) of McBride et al. (2009), equating the group dynamical mass estimate to the group halo mass and applying our universal baryon mass fraction. Contrasting this inflow rate with the estimate of the total SFR of the GROUPGALAXY satellite spirals in the group, we find the star formation to equate, on average, to ∼1% of the baryon inflow. Even considering the hypothetical limiting case for the total star formation of group member galaxies, we find that the star formation equates to ∼10% of the baryon inflow.

In summary, the rate of replenishment of the IHM and the size of the reservoir imply that, if even only a small fraction of the IHM can cool and be accreted, this reservoir is easily sufficient to support the inflows and prolonged star formation in satellite spiral galaxies required by our empirical results, making the required fueling from the IHM a viable option.

9.3.4. *Variability of SFR of Satellite Spiral Galaxies*

Finally, in the context of the replenishment of the ISM of satellite spiral galaxies, it is interesting to consider the variability of the SFR of these objects. If the required fueling of satellite galaxies is indeed sourced largely from the IHM of the group, it may be expected to take place indefinitely, rather than only occurring for a limited time. In such a scenario both the quenching and the fueling of star formation, and as a result the SFR, might be expected to vary on timescales comparable to the orbital timescale of the galaxy as it transits regions in which gas stripping of the ISM/CGM and the accretion of gas from the IHM into the ISM, respectively, are more/less efficient, e.g., via a dependence on the density and temperature profile of the IHM. Indeed, for the refueling model we find preferred quenching probabilities of ∼0.8–1.2 Gyr^{-1}, corresponding to the inverse of the typical dynamical timescales, and which might be related to pericentric passage of the satellite. This would introduce an additional intrinsic scatter in the ψ_*–M_* relation at fixed M_*, which would potentially offer an explanation to our empirical result that the intrinsic scatter of this relation is higher (at 0.59 dex; 0.44 dex 1σ equivalent) for grouped spirals than for field spirals (at 0.36 dex; 0.27 dex 1σ equivalent).

Overall, in a statistical sample, one thus might expect to find satellite galaxies with increasing and declining SFRs, rather than only such with declining SFR as would be expected if fueling were sourced from a gas reservoir tightly associated with the satellite galaxy and being slowly depleted. We have shown that a refueling model is indeed consistent with the distribution of $\Delta\log(\psi_*)$ for satellites and indeed provides the best fit to the data of the models considered. A ready means to investigate the refueling hypothesis further in future work would be to consider the distribution of short wavelength colors of the galaxy sample, e.g., FUV–NUV or NUV–u. Provided that the timescale the color is sensitive to is short enough, a population of galaxies with increasing star formation should have different colors than one with gradually declining SFR, potentially enabling a distinction between the scenarios.

10. Discussion

Overall, our investigation of the star formation and gas fueling of spiral/disk-dominated galaxies in the local universe has found that these objects are characterized by a rapid cycle of gas into and out of the ISM replenishing the gas consumed by star formation. Based on our consideration of satellite spiral galaxies and regardless of the details of the gas fueling model considered, we conclude that the fueling of spiral galaxies is largely independent of environment, with substantial flows of gas into and out of the ISM of the satellite galaxies on timescales of several gigayears *while* the galaxy is a satellite. Furthermore, consideration of the reservoirs of gas available to these satellite galaxies on infall and the dependence of SFH on galaxy mass favor scenarios in which this sustained accretion is fueled from the IHM of the DMHs of their host galaxy group, rather than from gas associated with the galaxy before it became a satellite.

10.1. Implications for the IHM

The fundamental question posed by our findings is that of the nature of the mechanism that enables the accretion of gas from the IHM into galaxies in general and into satellite galaxies in galaxy groups in particular. In the mass range of our groups, the virial temperature is generally $\gtrsim 10^6$ K, yet IHM gas must be at least as cool as $T_{\rm gas} \gtrsim 10^5$ K in order to accrete directly onto the ISM of massive spiral galaxies in our sample and cooler still if the accretion occurs first onto the CGM. Our results also require IHM fueling of the low-mass galaxies in our sample, for which even lower IHM temperatures are required. Thus, our findings fundamentally require the IHM of galaxy groups to be a two-phase medium, encompassing a cold phase and a warm/hot phase, with fueling of the galaxies occurring more or less continuously in small increments from this IHM, largely independent of the galaxies' environment. This is unlike the standard picture of cold-mode accretion with its associated dominant streams and halo mass dependence (Kereš et al. 2005; Dekel & Birnboim 2006; Torrey et al. 2012; but see also Kereš et al. 2009). Further indirect observational support for a multiphase IHM in galaxy groups may also be supplied by the recent findings that the distribution of Mg II absorption around "isolated" central galaxies, indicative of a cold clumpy component, is self-similar as a function of DMH mass, extending to halos of mass $M_{\rm halo} \approx 10^{14}\,M_e$ (Churchill et al. 2013), implying that a multiphase medium can exist in halos of the mass scale of the galaxy groups studied here.

This cold phase of the IHM, by necessity, must have a relatively small volume filling factor and pervade the volume sampled by the orbits of the satellite galaxies, rather than be associated with the CGM of the individual galaxies, as we have previously argued. Future work will have to focus on understanding the origin of this two-phase medium, and in particular that of the cold phase. One possible solution is that the hot gas atmosphere does not extend to the group virial radius, but rather ends at much lower group-centric distances due to cooling processes operating in the IHM of galaxy groups spanning the mass range from $\sim 10^{11.75}$ to $10^{14.4}\,M_e$ of the groups considered in this work. This, in turn, would imply that the tipping point for the free-fall timescale of the groups to exceed the cooling timescale of the IHM in the groups occurs at higher group masses than expected, due to some cooling mechanism operating in the IHM that has not previously been considered.

One possibility is cooling of the IHM due to inelastic collisions of ions and electrons in the plasma with dust particles. This process is the most efficient coolant for hot gas with $T \gtrsim 10^{5.5}$ K (see, e.g., Dwek & Werner 1981). Simulations by Montier & Giard (2004) show that dust cooling exceeds gas-phase cooling processes if the dust-to-gas ratio in the IHM exceeds $\sim 10^{-4}$ by mass ($\sim$1% of the value in the ISM). There is some observational evidence that there is sufficient dust in the IHM for this mechanism to be operating in Stefan's Quintet compact galaxy group (Natale et al. 2010). The mechanism requires a continuous injection of dust into the IHM to balance losses of grains through sputtering in the hot plasma. Possible sources for dust can be the injection via stars released from galaxies into the IHM during galaxy–galaxy interactions (Natale et al. 2010), or through winds driven out of satellite galaxies depositing dust along their orbits. Support for the latter is provided through observations of individual edge-on spiral galaxies in the field revealing copious amounts of dust in their CGM scattering non-ionizing UV light from massive stars in the disk (Hodges-Kluck & Bregman 2014; Seon et al. 2014). If, as we have argued in Sections 9.3.2 and 9.3.3, the CGM will be stripped from the host galaxy on entry into a group, the dust in the CGM would thereby be injected into the IHM (see also Popescu et al. 2000). Future analysis of diffuse FIR emission of groups on scales of 0.1–1 Mpc could in principle determine the total cooling rate of the hot component of the IHM due to dust.

10.2. Implications for the Color–Density Relation

Having controlled for both morphology and environment in our analysis, we can also leverage our results to shed light on the mechanisms underlying the color–density relation (e.g., Lewis et al. 2002; Pimbblet et al. 2002; Gómez et al. 2003; Baldry et al. 2004; Balogh et al. 2004; Kauffmann et al. 2004; Blanton & Roweis 2007; Bamford et al. 2009; Cucciati et al. 2010; Zehavi et al. 2011). This relation simply states that the colors of galaxies are redder (indicative of less star formation activity) in denser environments. Since the pioneering work of Hubble & Humason (1931) and Dressler (1980), it is also known that early-type galaxies predominantly reside in denser regions, and it has also been shown that color/SFR and morphological type of a galaxy are correlated (James et al. 2008). Finally, although local density (as measured in fixed apertures or out to a specified nth neighbor) and host DMH mass are correlated, mapping from one to the other is nontrivial, in particular in the regime of galaxy groups, due to the considerable scatter (Haas et al. 2012).

The question thus arises whether the color–density relation is driven by galaxy–galaxy interactions or some other process changing the morphological mix of galaxies, or whether it is driven by a changed thermodynamic state of the IHM, leading to a decrease in availability of gas sufficiently cold to be accreted onto galaxies and fuel star formation. Since we have controlled for morphology, we can differentiate between these scenarios. In particular, we have presented evidence in favor of the ongoing gas fueling of a highly pure morphologically selected sample of disk-dominated galaxies in the group environment, with this fueling being sourced from reservoirs extraneous to the galaxy—in particular the IHM. We therefore conclude that the color–density relation is not predominantly due to the gas fueling rate as determined by the host DMH mass, but rather, to a large part, is due to a change in the

morphological type of galaxies toward more bulge-dominated systems (a comparison of spiral fraction for field and group galaxies is shown in the top panel of Figure 3). Most particularly for satellite galaxies in groups, there seems to be no obvious reason why the rate of inflow of gas on >100 kpc scales from the IHM onto a galaxy should be influenced by whether the galaxy is disk or spheroid dominated. As such, the underlying physical mechanism of the color–density relation likely links the ability of a galaxy to retain gas and convert it into stars to its morphology, i.e., to the relative importance of the bulge. This is in line with findings that galaxies with prominent bulges (which we have deliberately excluded from our analysis) are driving the downturn in slope of the SFMS at higher stellar mass. In this picture, the rate at which star formation is decreased over time within the group environment is controlled by the rate at which the galaxy morphology is transformed, in which case one might expect the bulge-to-disk ratio to increase with decreasing group-centric distance (since the latter is a proxy for lookback time since a galaxy first entered the group). Indeed, George et al. (2013) find exactly this, even among the quenched population (but see Carollo et al. 2016 for a contrasting view[52]).

If morphological transformation is indeed mainly driven by galaxy–galaxy interactions, the interpretation of the color–density relation presented is entirely consistent with the idea that galaxy–galaxy interactions are the main factor driving the evolution of galaxies in the group environment, as often argued in recent works (e.g., Robotham et al. 2013, 2014; Alatalo et al. 2015; Davies et al. 2015; Bitsakis et al. 2016). It seems to be the morphological transformations (in the sense of an increase of the bulge component) triggered by these events, rather than the increasing dominance of hot gas in collapsing structures, that is the main factor causing the star formation of the galaxy population to switch off in the present epoch on the megaparsec scale of the composite halos of galaxy groups.

Nevertheless, we have also shown that there are also (rare) events by which the star formation of a spiral/disk can be quenched without it undergoing morphological transformation, as evidenced by our population of quenched spiral/disks. These findings are in line with Masters et al. (2010), who also identify a population of red spirals with intrinsically low sSFR. However, these will be primarily of interest in what they can tell us about the process of gas fueling, rather than in their direct effect on the observed properties of the galaxy population in groups, which, as we have shown, is relatively small.

[52] Carollo et al. (2016) find that the morphological mix among quenched galaxies in the group environment is constant as a function of group-centric distance. Based on this finding, they argue in favor of a process linked to the large-scale group DMH halo driving the quenching of satellite galaxies, with the efficiency in terms of number of affected satellites increasing toward the group center, and identifying secular differential fading of the disk component in quenched galaxies as being responsible for the differences in the morphological mix between star-forming and quenched satellites. Considering the implications of the scenario suggested by Carollo et al. (2016) in the context of our empirical analysis, we find that, as our morphological selection should be robust to disk fading on the timescale of several gigayears (see Appendix A) and the differential fading mechanism proposed by Carollo et al. (2016) is predicated on a rapid quenching of star formation, under this alternative scenario we would expect a substantial population of disk galaxies with very highly suppressed SFR in the group environment, in excess of that found in our analysis. Furthermore, we note that the steep radial age gradients in the stellar population required in terms of the differential fading model appear to be in conflict with the shallow gradients observed in local spiral galaxies (e.g., MacArthur et al. 2009; Sánchez-Blázquez et al. 2011, 2014).

Finally, we may also note that the more complex shorter-term variations in SFR exhibited by interacting galaxy pairs, which are observed to die down as a function of separation (e.g., Davies et al. 2015), are also consistent with, and may require, a recovery of gas fueling to its pre-interaction level relatively soon after an interaction event has changed the amount and/or distribution of gas in the ISM of a galaxy. In this sense, it would appear that galaxy–galaxy interactions may only be able to manifest as the dominant process influencing SFR due to the surprising constancy of the gas fueling process in all non-interacting systems, independent of the larger-scale environment, as evidenced by the present analysis.

10.3. Implications for the Morphological Transformation of Satellite Galaxies

Although the morphological transformation of galaxies from disk- to bulge-dominated systems is generally ascribed to galaxy–galaxy interactions and the secular fading of the disk component after quenching of star formation, the prolonged, substantial accretion (see Table 6) of group IHM onto satellite galaxies will impact the morphology of these galaxies and may provide an additional pathway for morphological transformation.

Unlike for central galaxies, where angular momentum is added coherently from the angular momentum of the group, for satellite galaxies accreting gas from the IHM, the accreted gas will have no preferred angular momentum vector with respect to that of the galaxy, resulting in a net angular momentum of zero for the accreted IHM. Considering our fiducial high and low stellar mass galaxies over the characteristic delay time of 2.5 Gyr, the ongoing accretion will result in between 3.4 and 6.5 (2.2 and 6.9) times the ISM mass upon infall being accreted into the ISM of the galaxy in the high (low) stellar mass ranges, and between 2.4 and 5.4 (1.2 and 5.9) times the ISM mass being expelled. This will clearly suffice to obliterate the original angular momentum of the gaseous ISM disk. Thus, the fact that star-forming disks are observed in satellite spirals would seem to imply that angular momentum from some reservoir can be transferred to the accreted gas. For satellite galaxies being fueled from the IHM the available reservoirs of angular momentum are (i) the stellar disk and (ii) the DM subhalo.

If the angular momentum of the ISM is (partly) replenished from that of the stellar component, then the specific angular momentum of the stellar and gas disks will decrease with continuing accretion. In addition, the formation of additional stars, potentially in part from gas accreted with zero net angular momentum, will further reduce the specific angular momentum of the stellar disk. One consequence of such a decrease in specific angular momentum is that the gas of the galaxy will settle more toward the center of the galaxy. Thus, the more centrally concentrated distribution of gas in satellite galaxies (Cayatte et al. 1994; Koopmann & Kenney 2004; Cortese et al. 2010; Bretherton et al. 2013; Dénes et al. 2016) may, at least in part, be the result of the continued inflow of gas rather than of the stripping of gas due to environmental processes. Furthermore, this will potentially result in less star formation and redder colors in the outer disks of satellite spiral galaxies than in comparable field galaxies, i.e., in different color gradients for these two categories of spiral galaxies.

In addition, a decrease in the specific angular momentum of the stellar component (primarily built up when the galaxy was a central and subsequently diluted by stars formed from accreted

gas with low angular momentum) will cause the stellar disk of the galaxy to shrink and the old stellar population to compactify (see also Elmegreen et al. 2014). As a result, at given stellar mass, satellites with ongoing accretion of IHM material would be predicted to have a more dominant bulge component and smaller disks than comparable field galaxies, driving them toward more lenticular/early-type morphologies. As such, ongoing accretion onto satellite galaxies may represent a further secular pathway for the morphological evolution of a galaxy from late to early type.

To obtain a simple conservative order-of-magnitude estimate of the reduction in specific angular momentum of the composite gas + stellar system, we consider the effect of mass growth as a result of accretion with zero net angular momentum, disregarding, in the first instance, the effects of mass outflows and the probable stochastic nature of gas fueling from the IHM. We consider two cases making use of our fiducial galaxies by (i) adding the total cycled gas mass[53] to the gas + stellar mass at infall and (ii) adding (only) the mass of newly formed stars. Assuming that the size of the disk of a galaxy is proportional to the specific angular momentum (e.g., Bullock et al. 2001), one would expect a decrease in disk size by (i) ∼0.29 dex (∼0.54 dex) in the high (low) stellar mass range and (ii) of 0.1 dex (0.16 dex) for the high (low) stellar mass range, over a period of 2.5 Gyr.

In the light of the ongoing accretion of gas from the IHM implied by our study, this would seem to imply that the specific angular momentum of the ISM and stellar component would need to be replenished from the DM subhalo of the satellite galaxy. As shown in Figure 23 in Appendix B, which displays the distributions of galaxy size as a function of stellar mass for the GROUPGALAXY and FIELDGALAXY samples, the median size of the GROUPGALAXY sample is smaller, though only by ∼0.03 dex (at all stellar masses). In light of the result of ongoing accretion, this may imply that the specific angular momentum of the ISM and stellar component is replenished from the DM subhalo of the satellite galaxy. However, theoretical studies indicate that strong stellar feedback and outflows from galaxies may enhance the effective retention of specific angular momentum in galaxies by preferentially removing low angular momentum gas (e.g., Sommer-Larsen et al. 1999; Governato et al. 2007; Agertz et al. 2011; Dalla Vecchia & Schaye 2012; Vogelsberger et al. 2013; Übler et al. 2014; Genel et al. 2015), in which case our simple consideration of case (ii) might be more appropriate, mitigating the need for angular momentum transfer from the DM subhalo. A detailed consideration of these processes for satellite galaxies is beyond the scope of this paper and will require future detailed theoretical and empirical consideration. Here, we limit ourselves to drawing attention to the possibility that the inflow of IHM gas onto satellite galaxies at the rate implied by our measurements of SFR represents a secular process through which disk-dominated galaxies can evolve into spheroid-dominated ones. Moreover, as discussed in Section 10.2, our analysis of the gas flows required to reproduce the observed distributions of SFR in our very pure sample of disk-dominated satellite galaxies shows that it is most likely a change in the mix of galactic morphologies in the group environment compared to the field, rather than a reduced propensity of the IHM to cool and fuel star formation, that is primarily responsible for the reduction in star formation activity of the galaxy population as a whole in groups compared to the field. It therefore follows, somewhat paradoxically, that the ongoing gas fueling of disk galaxies in the group environment may itself lead to a secular quenching of the star formation of galaxies after falling into groups. This route for the quenching of star formation in disk galaxies would be tantamount to death by gluttony, in marked contrast to a death by starvation, which most previous studies have invoked. Future work will place further constraints on the efficacy and timescales for this secular quenching mechanism and the relative importance to mechanisms for morphological transformation and quenching related to galaxy–galaxy interactions by considering the SFRs and SFHs of group galaxies divided into finer morphological classifications, most particularly in the range from S0 to Sa.

[53] We make use of the inflow rates derived for the refueling model.

11. Summary and Conclusions

Making use of morphologically selected samples of disk-dominated/spiral galaxies, we have conducted a detailed investigation of the impact of the group environment on the star formation activity of central and satellite group spiral galaxies, as well as of a sample of largely isolated field (central) spiral galaxies, isolating the effects of galaxy–IHM interactions from those of galaxy–galaxy interactions. We have described the samples in detail and present the results of our analysis as an empirical reference for current and future theoretical work aimed at understanding the importance and impact of galaxy–IHM interactions, including gas fueling, for the evolution of galaxies in the group environment.

This analysis has made use of the NUV emission of a galaxy as a tracer of its SFR, rather than Hα. In addition to reliably sampling the total star formation activity of the galaxy (which may be inhomogeneously distributed), this choice also renders our analysis largely robust against uncertainties of the IMF, as well as against stochastic variations in the SFR, while providing enough time resolution to resolve (in time) processes linked to the environment and its characteristic timescale of ∼1 Gyr. Furthermore, we have employed newly developed radiation-transfer-based techniques to account for the effect of dust on the ratio between observed and intrinsic NUV emission, enabling the intrinsic SFR of the galaxy sample to be determined with great precision, including the SFR of a full set of quenched spirals.

Having made the isolation of the effects of galaxy–IHM interactions from those of galaxy–galaxy interactions a main objective of our sample construction, we have been able to interpret our empirical results on the SFR distribution of our galaxy sample in terms of the gas cycle of these galaxies via implementation of the Schmidt–Kennicutt relation,[54] with particular focus on their gas fueling, i.e., the accretion of gas from the IHM onto the galaxy. This has led us to a number of new results, some of which force us to question our knowledge of the process and regulatory agents of gas accretion by galaxies in the group environment. In the following, we briefly summarize our main results and conclusions as presented and discussed in the preceding sections.

[54] Although our inferences are thus, by necessity, indirect, they will be testable by SKA pathfinders—e.g., the DINGO survey of the ASKAP will provide HI data of sufficient depth covering the GAMA regions to test if and how the gas content of spiral galaxies reflects the NUV-based sSFR.

(1) *Central spiral galaxies*

In our analysis we have considered the isolated field central spiral galaxies and group central spiral galaxies separately. In doing so, we have found the following:

(a) The ψ_*–M_* relation for largely isolated central spiral galaxies is well characterized by a single power law $\psi_* \propto M_*^{\gamma}$ with $\gamma = -0.45 \pm 0.01$ and a very low scatter of 0.36 dex interquartile (1σ 0.27 dex) around the relation (see Figure 8 and Table 2). This also implies that the turnover in the main sequence of star-forming galaxies reported by other authors (e.g., Lee et al. 2015; Schreiber et al. 2015; Erfanianfar et al. 2016) is due to an increase of (more) bulge-dominated galaxies at higher mass in their samples of star-forming galaxies.

(b) The existence of a remaining population of strongly quenched field spiral galaxies, predominantly at higher stellar mass, in spite of the reduction in scatter, implies the existence of a possibly mass-dependent secular quenching mechanism for field spiral galaxies.

(c) The normalization of the ψ_*–M_* relation for largely isolated central spiral galaxies evolves gradually but noticeably over the short redshift range of $z = 0.05$–0.1 (see Figure 9). This evolution is shown to be in agreement with that predicted by the empirical fit to the evolution of the main sequence of star-forming galaxies presented by Speagle et al. (2014).

(d) The ψ_*–M_* for group central spiral galaxies is very close to and largely coincides with that for field central spiral galaxies over the full mutual range of stellar mass, implying a lack of environmental dependence of the gas fueling of central spiral galaxies (see Figure 13).

A further discussion of these findings is deferred to a future paper in this series.

(2) *Satellite Spiral Galaxies*

Considering the ψ_*–M_* relation for satellite spiral galaxies, we find the median relation to be offset from that of the field and group central spiral galaxies by $\sim$0.1–0.2 dex at all M_* (see Figure 13 and Table 2). Making use of the full distribution of the offset of ψ_* around the median for a given stellar mass M_*, we find the offset in the median to arise from a minority population of galaxies with strongly suppressed sSFR with respect to that of comparable field spiral galaxies, while the majority of satellite spiral galaxies at all M_* display sSFRs akin to those of comparable field spiral galaxies (see Figure 14).

Contrasting the observed distributions of sSFRs for group spiral galaxies with those obtained from a number of empirically informed models of the SFH of spiral galaxies in the group environment designed to bracket the range of plausible SFHs (see Figures 18–20), we find the following:

(a) The gas cycle of spiral/disk galaxies is characterized by a rapid cycle of gas into and out of the ISM, with rates of inflow and outflow comparable to or larger than the SFR. Furthermore, this rapid cycle is largely independent of the galaxies' environment, being inferred for field, group central, and group satellite spirals.

(b) In order to reproduce the observed distributions, contrary to the standard paradigm of satellite galaxy evolution, we require the ongoing replenishment of the ISM of spiral satellite galaxies *while* they are satellites in a galaxy group. This replenishment must take place over gigayear timescales and be comparable to that which is generally assumed to support the quasi-constant star formation in field spiral galaxies.

(c) Furthermore, simple conservative considerations of the depletion timescales and gas reservoirs for group satellite spiral galaxies favor the IHM of the host group being accreted into the ISM of satellite galaxies, rather than material associated with the galaxy at the time it became a satellite, as a source of fuel for this replenishment, also contrary to the standard paradigm of satellite galaxy evolution.

(d) The ongoing fueling of spiral satellite galaxies implies that the color–density relation is the result of an increase in the fraction of morphologically late-type galaxies in denser environments rather than an environmental effect on the gas fueling of galaxies. The dichotomy in sSFR at given stellar mass between early- and late-type galaxies, accordingly, is driven by galaxy-specific processes likely linked to their morphology.

(e) The implied ongoing substantial accretion of gas with zero net angular momentum by satellite spiral galaxies represents an additional efficient mechanism capable of facilitating the morphological transformation of late-type galaxies to more bulge-dominated earlier types in the (denser) environment of galaxy groups. Potentially, therefore, this continued gas accretion and star formation will lead to a gradual buildup of spheroidal components in satellite disk galaxies, which, in turn, will lead to a secular quenching of the star formation, representing a "death by gluttony," in sharp contrast to the "death by starvation" scenario previously invoked for such mechanisms.

Overall, our analysis has returned a number of surprising results that are difficult to reconcile with the standard picture of galaxy evolution in the group environment. The emerging picture is that of an ongoing process of gas fueling for both central and satellite spiral galaxies, largely independent of environment, supporting spiral galaxies as systems characterized by a rapid in- and outflow of gas, cycling the fuel needed to support star formation in and out of the ISM of the disk and replenishing it as required. Nevertheless, a small minority of satellite spiral galaxies with strongly quenched star formation are observed, whose provenance remains unclear. Overall, we are left to conclude that our current understanding of galaxy evolution in the group environment remains incomplete.

We would like to thank the anonymous referee for insightful comments that helped us improve the manuscript. M.W.G. and R.J.T. thank Jay Gallagher for helpful discussions during the formative phases of this project.

M.W.G. gratefully acknowledges the support provided by the International Max-Planck Research School on Astronomy and Astrophysics Heidelberg (IMPRS-HD) and the Heidelberg Graduate School for Fundamental Physics (HGSFP) during the performance of some of the work presented here. C.C.P.

acknowledges support from the Leverhulme Trust Research Project Grant RPG-2013-418 and from a previous grant from the UK Science and Technology Facilities Council (STFC; grant ST/J001341/1).

GAMA is a joint European-Australasian project based around a spectroscopic campaign using the Anglo-Australian Telescope. The GAMA input catalog is based on data taken from the Sloan Digital Sky Survey and the UKIRT Infrared Deep Sky Survey. Complementary imaging of the GAMA regions is being obtained by a number of independent survey programs, including *GALEX* MIS, VST KiDS, VISTA VIKING, *WISE*, *Herschel*-ATLAS, GMRT, and ASKAP, providing UV to radio coverage. GAMA is funded by the STFC (UK), the ARC (Australia), the AAO, and the participating institutions. The GAMA Web site is http://www.gama-survey.org.

GALEX (*Galaxy Evolution Explorer*) is a NASA Small Explorer, launched in 2003 April. We gratefully acknowledge NASA's support for construction, operation, and science analysis for the *GALEX* mission, developed in cooperation with the Centre National d'Etudes Spatiales (CNES) of France and the Korean Ministry of Science and Technology. We are grateful to the institutions in the GAMA/H-Atlas/Dingo Consortia, which made possible further *GALEX* observations of GAMA fields as part of the *GALEX* Sky Completion Project.

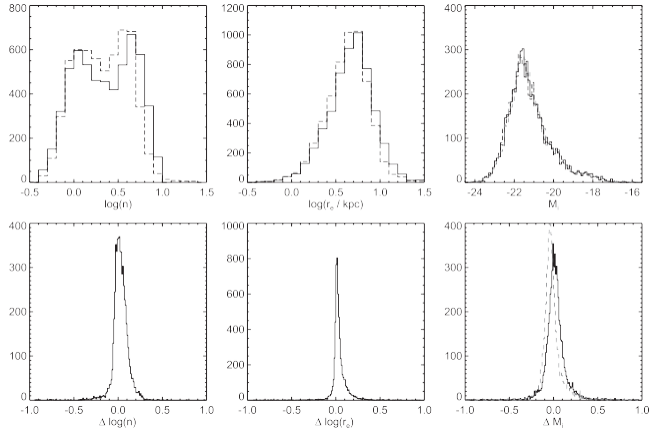

Figure 21. Top row: distributions of the parameters log(n), log(r_e), and M_i for the 5747 galaxies common to GAMA and the data set used by Grootes et al. (2014). The values from Grootes et al. (2014) are shown as solid lines, and those determined by GAMA are shown as dot-dashed lines. For the parameter M_i the GAMA single Sérsic magnitudes are shown as a black dot-dashed line, and the fixed aperture magnitudes are shown as a gray dashed line. Bottom row: distributions of the differences of the parameter values (Grootes et al. (2014) value – GAMA value) for common galaxies. For M_i the difference to the GAMA single Sérsic profiles is shown as a black solid line, while the difference to the fixed aperture photometry is shown as a gray dashed line.

Appendix A
Selection of Disk/Spiral Galaxies

A main requirement of our analysis is that the sample of spirals used be selected purely based on morphology and provide an unbiased representation of the SFR distribution of spiral galaxies both in the field and in groups. Furthermore, the sample used must be as pure and simultaneously complete as possible. Recently, Grootes et al. (2014) have presented a method of morphologically identifying spiral galaxies capable of meeting these requirements. Their method identifies the morphology of a galaxy based on its position in a 3D parameter space spanned by a range of optical wavelength galaxy properties. In our analysis we have chosen to use the parameters Sérsic index n, r-band effective radius r_e as determined from the single Sérsic fit, and i-band absolute magnitude M_i, i.e., the combination (log(n), log(r_e), M_i), which has been shown to recover highly complete, pure, and unbiased samples of spiral galaxies.

As emphasized in Grootes et al. (2014), their classification tables have been calibrated using SDSS DR7 photometry and single Sérsic fits performed by Simard et al. (2011) using GIM2D, and researchers using the classifications are cautioned to check whether their data are compatible, ideally by using a common subsample. Figure 21 shows the distributions of log(n), log(r_e), and M_i for 5747 galaxies common to GAMA and the data set used in Grootes et al. (2014). The agreement in the parameter values is very good for all parameters, so that we find the selection scheme to be applicable as calibrated. While Grootes et al. (2014) extrapolate the SDSS DR7 Petrosian photometry to total Sérsic magnitudes using the prescription of Graham & Worley (2008), GAMA provides both single Sérsic profile and fixed aperture i-band photometry. For the purpose of identifying galaxies using the method of Grootes et al. (2014) we have made use of the single Sérsic (total) magnitudes. However, with the GAMA data used in our analysis reaching a depth of $r \sim 19.4$ and extending to a redshift of $z = 0.13$, a non-negligible fraction of the fainter sources is only marginally resolved. For these, Sérsic profile fitting may not always provide the most accurate or reliable estimate of the total galaxy flux. In selecting our sample, we have therefore independently classified our sample using the GAMA i-band single Sérsic profile and fixed aperture photometry. Sources with differing classifications have been visually inspected and manually classified to obtain our final sample of spiral galaxies. In selecting spiral galaxies we have chosen to use the calibration of the combination (log(n), log(r_e), M_i) using threshold values of $\sigma_{sp} \sim 0.4$ and $D\sigma_{sp,rel} \sim 1$ as specified in Grootes et al. (2014). Finally we emphasize that, although largely complete, as demonstrated in Grootes et al. (2014), this selection places slightly more emphasis on the purity of the spiral samples.

While Grootes et al. (2014) have demonstrated the performance of the selection method on samples with no distinction of galaxy environment, for the purposes of defining the GROUPGALAXY sample, we must consider an additional possible difficulty. If a spiral galaxy consists of an old stellar bulge component with no (or little) star formation, as well as a disk in which the bulk of the star formation takes place, a cessation of star formation will cause the disk to fade relative to the bulge. In turn, this might affect the values of n and r_e, causing a spiral galaxy to no longer be classified as such without any actual change in morphology. Importantly, this would lead to a preferential loss of quenched spiral galaxies.

To gain a simple insight into the potential impact of this scenario, we consider a fiducial spiral galaxy that consists of a bulge component with luminosity B_0 and a disk component with luminosity D_0 such that the total luminosity $T_0 = B_0 + D_0$. We further assume the age of the stellar population of the bulge to be such that any fading over a timescale of several gigayears prior to observation is negligible, i.e., $B_{fade} = B_0$, and assume all recent and midterm star

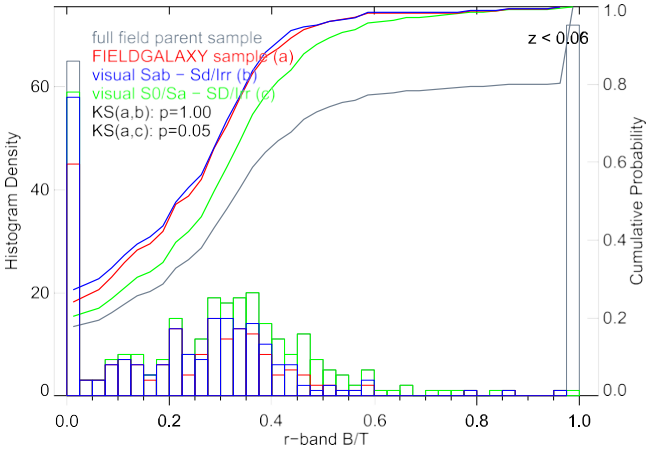

Figure 22. Distribution of r-band B/T values for GAMA sources in the FIELDGALAXY (red) and FIELDGALAXY parent sample (gray) with $z \leq 0.06$ as determined by Lange et al. (2016). Those members of the FIELDGALAXY parent sample visually classified (Kelvin et al. 2014) as Sab—Sd/Irr galaxies are shown in blue, while the superset additionally including S0/Sa galaxies is shown in green. Cumulative distribution functions are overplotted as colored lines. The p-values of Kolmogorov–Smirnov tests comparing the distributions are shown in the figure.

formation ($\geq$8 Gyr prior to observation) to have taken place in the disk. For a given quenching/fading scenario we can express the luminosity of the faded disk component as $D_{\rm fade} = \eta D_0$, which enables us to estimate the faded bulge-to-total ratio as

$$(\mathrm{B}/\mathrm{T})_{\rm fade} = \frac{(\mathrm{B}/\mathrm{T})_0}{h + (1-h)(\mathrm{B}/\mathrm{T})_0} \quad (22)$$

following Carollo et al. (2016).

Combining the visual morphological classifications of GAMA sources with $z \leq 0.06$ presented by Kelvin et al. (2014) and the bulge–disk decompositions of this sample presented by Lange et al. (2016) and cross-matching with our samples using GAMA's unique source identifier, we find an average r-band B/T value of B/T = 0.3 (0.18) in the high (low) stellar mass range of the FIELDGALAXY sample and a comparable value of B/T = 0.32 (0.19) for those galaxies in the FIELDGALAXY parent sample visually classified as S0/Sa–Sd/Irr. As fading will only act to increase the B/T ratio, we restrict ourselves to considering the high stellar mass range as our fiducial galaxy. As such, for the SFH of our disk component we adopt an exponentially declining SFH over the last 8 Gyr prior to observation with a timescale of 3.5 Gyr, which provides a good fit to the SFH of our fiducial high stellar mass galaxy evolving according to the SFMS of Speagle et al. (2014) over that time. We use this SFH as our baseline and modify it in accordance with a range of quenching scenarios. Subsequently, we make use of STARBURST99 (Leitherer et al. 1999, 2014) to model the (intrinsic) spectral energy distribution (SED) of the disk component and determine the degree of fading for each scenario.

Assuming an exponentially declining SFR over the 2.5 Gyr (1 Gyr, 2 Gyr, 3 Gyr) prior to observation with a time constant of 0.5 Gyr, i.e., a rapid quenching (e.g., Wetzel et al. 2013), we find $\eta = 0.64$ (0.82, 0.69, 0.59) and $(\mathrm{B}/\mathrm{T})_{\rm fade} = 0.40$ (0.34, 0.38, 0.42). Considering slower declines in the star formation activity, i.e., longer time constants as favored by more gradual quenching models and some quenching models in our analysis, the change in B/T ratio is even smaller. For a time constant of 1 Gyr we find a $(\mathrm{B}/\mathrm{T})_{\rm fade}$ of 0.37 (0.32, 0.35, 0.39) for 2.5 Gyr (1 Gyr, 2 Gyr, 3 Gyr) evolution, while for a time constant of 1.5 Gyr the B/T ratio decreases to 0.35 (0.31, 0.34, 0.36) for an onset of quenching 2.5 Gyr (1 Gyr, 2 Gyr, 3 Gyr) prior to observation. As such, we do not expect disk fading due to quenching over timescales of several gigayears to shift a significant fraction of sources out of the range of B/T values recovered by the method of Grootes et al. (2014) (see Figure 22). Accordingly, we conclude that, while the secular fading of stellar disks may lead to the loss of some quenched galaxies from the GROUPGALAXY sample, this will affect only a minority of potential sample members and will not strongly bias the samples. Furthermore, as the adopted selection method recovers the underlying SFR distribution of disk galaxies (see Grootes et al. 2014 and Section 4.2), our conservative treatment of the infall time distribution can adequately limit any potential remaining bias.

Appendix B
Deriving Attenuation Corrections

Dust in the interstellar medium of galaxies can strongly affect the ratio of observed to intrinsic emission from these objects, typically attenuating the emission of late-type galaxies by a factor of 2–10 in the NUV. Thus, in order to make use of the NUV emission of a galaxy as a tracer of its SFR, it is essential to correct for this attenuation and make use of the *intrinsic* emission. In principle, an accurate correction is only possible by modeling the full FUV–FIR SED using radiation transfer techniques in conjunction with independent knowledge of the geometry and orientation of the galaxy. However, the majority of galaxies in our sample are not detected in the FIR. We therefore make use of the method of obtaining accurate radiation-transfer-based attenuation corrections for samples of spiral galaxies without available FIR data presented by Grootes et al. (2013). These authors have shown that the critical parameter determining the attenuation of emission from a galaxy, i.e., the opacity due to dust, can be accurately estimated using the stellar mass surface density. As demonstrated by Grootes et al. (2013) using the GAMA survey, this technique, which makes use of the radiation transfer model of Popescu et al. (2011), enables the derivation of highly accurate attenuation corrections for large samples of spiral galaxies.

In determining attenuation corrections we have proceeded as follows.

The GAMA measurements of galaxy stellar mass and size have been used to determine the effective stellar mass surface density μ_* as

$$\mu_* = \frac{M_*}{2\pi D_A^2(z) q_{e,ss,r}^2}, \quad (23)$$

where $D_A(z)$ is the angular diameter distance corresponding to the redshift z, M_* is the stellar mass, and $q_{e,ss,r}$ is the angular size corresponding to the effective radius of the r-band single Sérsic profile. Using this estimate of μ_*, we have used Equation (5) of Grootes et al. (2013) to determine the central face-on opacity in the B band t_B^f.[55]

[55] t_B^f constitutes a reference value for the radiation transfer model of Popescu et al. (2011). The reader is referred to Grootes et al. (2013) and Popescu et al. (2011) for details of the parameters.

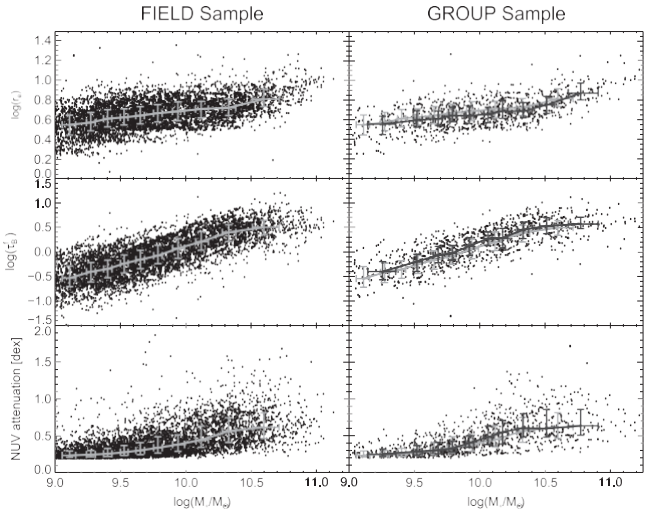

Figure 23. Distribution of r-band effective radius (top) as a function of $M*$ for the FIELDGALAXY (left) and GROUPGALAXY (right) samples. The resulting distributions t_B^f and the attenuation corrections applied in the NUV are shown in the middle and bottom panels, respectively. The median distributions for the FIELDGALAXY sample are shown as solid gray lines, while those of the GROUPGALAXY sample are shown as a solid black line in the right panels. The error bars indicate the interquartile ranges in bins containing equal numbers of galaxies (10% of the respective parent samples).

Next, the r-band axis ratio of each galaxy, as measured by the single Sérsic profile fit, is used to estimate its inclination. These inclinations are then corrected for the effects of finite disk thickness as detailed in Grootes et al. (2013) and in Section 3 of Driver et al. (2007), with an assumed intrinsic ratio of scale height to semimajor axis of 0.12.

Combining the estimates of the galaxy's t_B^f and inclination, we then determine the attenuation of the (NUV) emission using the model of Popescu et al. (2011).

The relation between t_B^f and μ_* presented in Grootes et al. (2013) has been calibrated on a subsample of spiral galaxies and accounts for the effect of dust on observed disk size (e.g., Möllenhoff et al. 2006; Pastrav et al. 2013a) using the corrections of Pastrav et al. (2013b). As this relation was calibrated on a sample of galaxies chosen with no regard to their environment, it is likely to have been dominated by galaxies that would belong to our FIELDGALAXY sample.

If the size of a galaxy at given mass varies with environment, this will affect the attenuation corrections applied in a systematic manner. Figure 23 shows the distribution of galaxy size r_e as a function of $M*$ for the GROUPGALAXY and FIELDGALAXY samples, as well as the distributions of the derived parameter t_B^f and the attenuation corrections as a function of $M*$. The correction distributions are very similar for both samples, although group galaxies appear to be slightly smaller at a given stellar mass than field galaxies (0.03 dex). However, the resulting shift in attenuation correction is negligible, as shown in the right bottom panel of Figure 23. Thus, under the assumption that the t_B^f–$M*$ relation is independent of environment, the method of Grootes et al. (2013) should supply accurate attenuation corrections.

However, environment-driven shifts in the spatial distribution of gas and dust with respect to the stellar component, as observed, e.g., in galaxies in the Virgo Cluster (Cortese et al. 2012a; Pappalardo et al. 2012), as well as systematic differences in the dust content of galaxies of a given mass as a function of environment, can be envisaged and represent a major source of uncertainty in the attenuation corrections applied and by extension in our analysis.

As discussed in Grootes et al. (2013), the underlying driver of the t_B^f–$M*$ appears to be the near-linear relation between $M*$ and $M_{\rm dust}$. If the dust content of galaxies is systematically different in the group and field environment, this will affect the attenuation corrections applied. However, with the stripping of material from galaxies by various mechanisms known to affect galaxies in groups, as seen in the Virgo Cluster (e.g., Chung et al. 2009; Pappalardo et al. 2012), it appears likely that any systematic difference will tend toward the ratio of gas to stars being smaller in groups. This would lead to overcorrections of the observed emission, making any observed suppression of star formation activity a lower limit on the actual suppression. However, it is also likely that this effect may be balanced by an increase in metallicity of the ISM of galaxies in the cluster environment, leading to higher dust-to-gas ratios. This might account for the empirical result that the dust content of spiral galaxies in the Virgo Cluster shows a lack of strong variation as a function of cluster-centric radius (Popescu et al. 2002; Tuffs et al. 2002). In addition, the observed radial gradients in the dust-to-gas ratio indicate that gas is much more efficiently removed than dust (Cortese et al. 2012b; Pappalardo et al. 2012), especially within the optical stellar disk. As the dust in the outer regions of the disk has a smaller effect on the observed NUV flux than that in the inner regions, this will mitigate the effect of stripping on the attenuation corrections.

Unfortunately, a detailed analysis of the t_B^f–$M*$ relation for galaxies in different group environments has not yet been performed, due largely to the lack of FIR data for these objects. Therefore, in this analysis, we *adopt* the assumption that the t_B^f–$M*$ relation is (largely) independent of environment. The systematic uncertainties due to environmental effects in the attenuation corrections are probably the largest systematic uncertainty in the study. In this context, we note that to explain a shift of ~0.1 dex in NUV flux by a shift via the calibration of the t^f–μ_* relation alone would typically require a systematic shift in $M*$ or t_B^f by ~25%.

Modeling the Star Formation History of Group Satellite Spiral Galaxies

In order to gain a quantitative understanding of the potential requirement of ongoing gas fueling in satellite spiral galaxies, we have constructed a number of models with parameterized SFHs (see Section 8) from which the distributions of $\Delta\log(\psi*)$ can be predicted, and which we can contrast with those observed for the GROUPGALAXY sample in the mass ranges $10^{9.5}\,M_\odot \le M* < 10^{10}\,M_\odot$ and $10^{10}\,M_\odot \le M*$. Here we describe how the model populations are constructed.

The construction of a model realization of the group galaxy population for a given SFH as satellite galaxies in the group environment requires the knowledge of the time since a galaxy first became a satellite $t_{\rm infall}$, the SFR of the galaxy at the time of infall $\psi_{*,\rm in}$, and the stellar mass at time of infall $M_{*,\rm in}$.

Provided this information, we can simply evolve the galaxy forward in time according to the chosen parameterized SFH.

Our goal in this modeling is to make as few a priori assumptions about the underlying physical drivers of the SFH

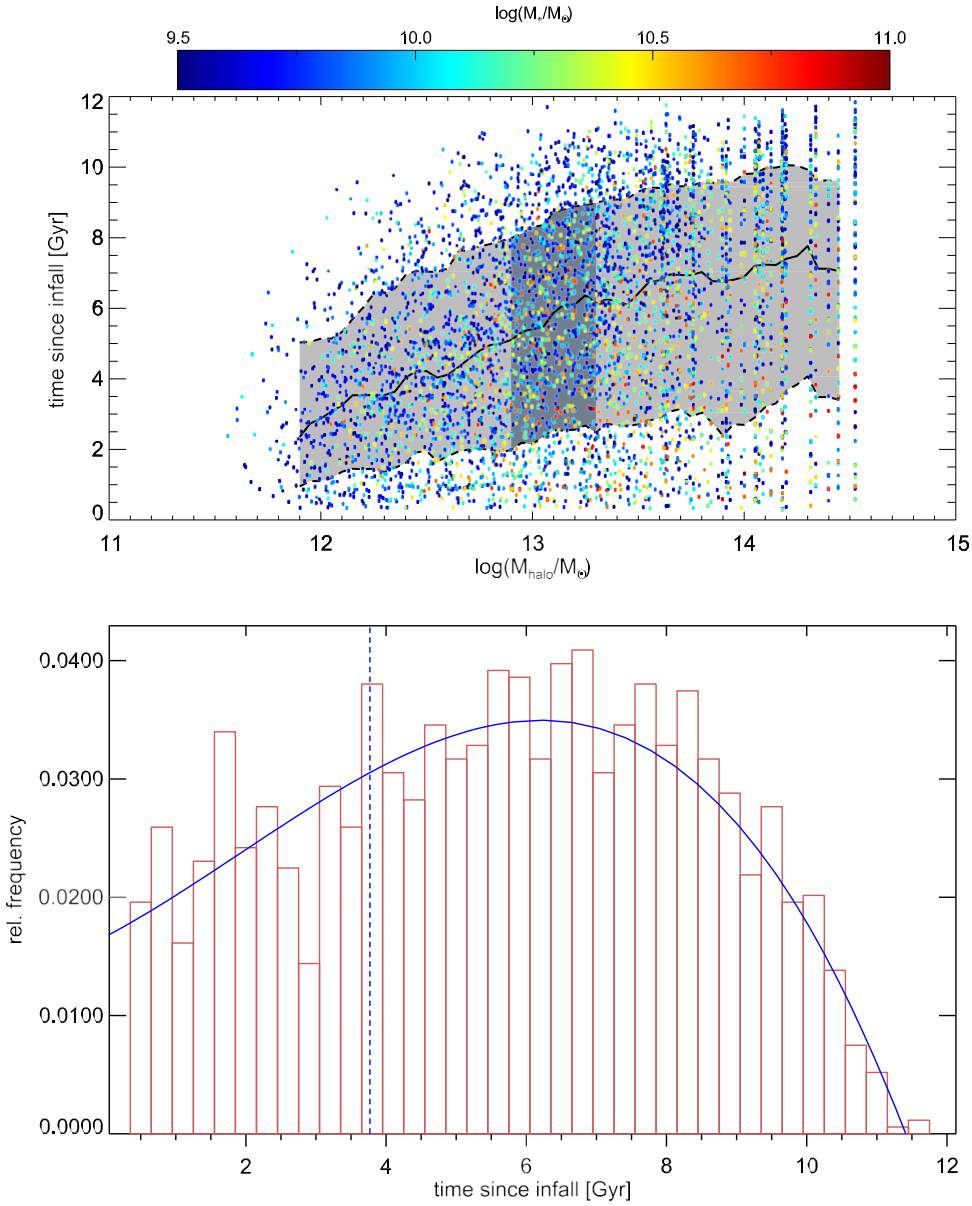

Figure 24. Top: time since infall as a function of host DMH mass for all satellite galaxies with $M* \geq 10^{9.5}$ from the mock GAMA survey light cones with $z \leq 0.13$. The stellar mass of the galaxy is encoded by the color of the symbol as indicated in the figure. The strong quantization at high halo masses is a result of the scarcity of such objects in the limited volume of the mock survey; however, this does not impinge on the mass range relevant to this analysis. The light-gray shaded area indicates the range between the 16th and 84th percentiles (both shown as black dot-dashed lines), in a moving bin of 0.2 dex width in $M_{\rm halo}$ with a step size of 0.05 dex. The median in these bins is shown as a solid black line. Superimposed on this is the dark-gray shaded area showing the range of DMH mass from which the distribution of infall times has been constructed. Bottom: distribution of time since infall for satellite galaxies residing in host DMHs with $12.9 \leq \log(M_{\rm halo}/M_{\rm e}) \leq 13.3$ in bins of 0.3 Gyr width. The blue solid line shows the result of a third-order polynomial fit ($a_0 = 0.01668$, $a_1 = 0.00314$, $a_2 = 0.00041$, $a_3 = -7.1 \times 10^{-5}$) to the distribution (assuming Poisson errors on each bin). The vertical blue line at 3.77 Gyr corresponds to the 30% shortest times since infall, the extremely conservative limit used in our modeling.

as possible, and rather to identify the best-fitting parameterized SFH and then in a second step interpret their physical implications. Therefore, we have chosen to rely on structure growth/galaxy evolution simulations only to determine the distribution of infall times (which is predominantly linked to the underlying DMH merger history) and to obtain the values of $F_{*,\rm in}$ and $M_{*,\rm in}$ using empirical relations.

In order to obtain a distribution of infall times for satellite galaxies, we make use of the mock GAMA light cones produced using the Millennium DM structure formation simulation (Springel et al. 2005) and the GALFORM semianalytic galaxy evolution model (Bower et al. 2006; Merson et al. 2013). Figure 24 shows the distribution of time since becoming a satellite galaxy for all satellite galaxies with $M* \geq 10^{9.5} M_{\rm e}$ in the mock GAMA survey out to a redshift of $z = 0.13$, as a function of the mass of the halo in which they reside. We find the distribution of time since infall to be very broad, with the median time since becoming a satellite increasing toward more massive host DMHs. Considering the satellite spiral galaxies of the GROUPGALAXY sample, we find that 68% of these reside in DMHs with masses between $10^{12.9}$ and $10^{14.03} M_{\rm e}$, with a median DMH of $10^{13.5} M_{\rm e}$. Therefore, in order to obtain a

conservative estimate of the infall time distribution for our modeling purposes, we use mock satellite galaxies residing in halos in the mass range $10^{12.9}\,M_e \leq M_{halo} \leq 10^{13.3}\,M_e$ and fit the resulting distribution of infall times with a third-order polynomial, as shown in Figure 24.

As is immediately apparent from Figure 6, showing the spiral fractions of the FIELDGALAXY sample and of the satellite galaxies, not all galaxies that fall into a group as a spiral retain this morphology. Instead, the spiral fraction of group satellite galaxies decreases by ~30%–40% with respect to the group environment over the stellar mass range $M_* \geq 10^{9.5}\,M_e$. Performing a weighted average over the spiral fraction of satellite galaxies in stellar mass bins of 0.2 dex covering the range $M_* \geq 10^{9.4}\,M_e$, we find an average spiral fraction of 30%. Here, we make the conservative assumption that *only* the youngest 30% of all satellite galaxies have a spiral morphology. Accordingly, in assigning infall times, we only consider the age range corresponding to the youngest 30% of the distribution, resulting in a maximum time since infall of 3.77 Gyr.

Having obtained a distribution of infall times, we proceed in constructing our model group satellite spiral populations as follows:

1. Create a Monte Carlo realization of the observed FIELDGALAXY sample in terms of stellar mass by sampling the observed distribution of M_*.
2. Assign each galaxy an infall time by sampling from the infall time distribution.
3. Assign each galaxy an SFR by sampling from the observed SFR distribution of the FIELDGALAXY sample in bins of 0.2 dex in M_*, using the bin that contains the assigned stellar mass of the galaxy.
4. Assign each galaxy an NUV background value and an NUV effective exposure time by sampling the observed distributions of both quantities.
5. Evolve the galaxy backward to t_{infall} using the empirical relation describing the evolution of the SFMS presented by Speagle et al. (2014). Here, we use a time step of 10^7 yr and assume that a fraction of $\alpha = 0.3$ of the total ISM mass converted to stars is immediately returned (e.g., Calura et al. 2014). We calculate the stellar mass at $t = t_{i-1}$ as

$$M_*(t_{i-1}) = M_*(t_i) - (1 - a)F_*(t_i)*\Delta t \quad (24)$$

and the SFR as

$$F_*(t_{i-1}) = F_*(t_i)\,\frac{S(t_{i-1}, M_*(t_{i-1}))}{S(t_i, M_*(t_i))}, \quad (25)$$

where $S(t, M_*)$ is the empirical relation describing the evolution of the SFMS provided in Equation (28) of Speagle et al. (2014).[56]
6. Evolve the galaxy forward in time to the assumed observation redshift of $z = 0.1$ according to the desired parameterized SFH, again assuming a return fraction of $\alpha = 0.3$. For each galaxy we convert its SFR into a UV flux by inverting Equation (1) and assuming that it is a point source at $z = 0.1$. We then compare this with our S/N requirement of S/N ≥ 2.5 using the assigned background and exposure time values. Where the predicted flux would lie below the S/N ≥ 2.5 limit, we have instead adopted an NUV flux at this level and have converted this back to an SFR, replacing the original estimate. This treatment is entirely analogous to our treatment of upper limits in the observed data.

For each of our one- and two-parameter models we create 50 realizations of ≈1000 galaxies (corresponding to the size of the GROUPGALAXY) sample at 31 and 31 × 31 sampling positions in the 1D and 2D parameter spaces, respectively. These model populations are then treated completely analogously to the observed satellite spiral galaxy sample in terms of the construction of the distributions of $\Delta\log(\psi_*)$. We subsequently average over the models to obtain an estimate of the distribution and of the variability.

We note that our forward modeling assumes that the evolution of the gas and stellar content of satellite spiral galaxies, as well as their SFR, is not significantly affected by galaxy interactions and/or merger events. Clearly, this assumption will not hold for nonspiral satellite galaxies, but is reasonable for morphologically classified spiral galaxies. Indeed, Robotham et al. (2014) show that, on average, the growth of stellar mass in galaxies is dominated by continuous accretion rather than (minor) mergers for galaxies with $M_* \geq 10^{10.7}\,M_e$. This will only be exacerbated for our sample of spiral galaxies *not* in close pairs, as the average merger rate for these objects will be lower than that determined for the close pairs of galaxies on which the analysis of Robotham et al. (2014) is based. In essence, we thus assume that the mass accretion history of the galaxies in our sample is dominated by smooth continuous accretion of gas and that any galaxy—galaxy interaction that significantly affects the stellar mass, gas mass, and star formation of a galaxy alters its morphology sufficiently to remove it from our sample. The second assumption is that we have assumed that the SFR and M_* distributions of field galaxies currently on the SFMS and of present-day satellites were the same at the epoch when the present-day satellites first became satellites. Given the only very weak dependence of infall time on stellar mass, this seems to be sufficiently fulfilled for the purposes of our simple models.

Appendix D
Constraining the Gas Cycle of Satellite Spiral Galaxies

In a general form the ISM content of a galaxy and its time-dependent evolution can be expressed as a balance between an inflow of gas into the ISM with a rate $\dot{M}_{in}$, an outflow of gas from the ISM with a rate $\dot{M}_{out}$, and the consumption of ISM by star formation as

$$\dot{M}_{ISM} = \dot{M}_{in} - \dot{M}_{out} - (1 - a)F_*, \quad (26)$$

where the factor $(1 - a)$ accounts for the (instantaneous) recycling of gas from high-mass stars back into the ISM.

Departing from Equation (26), it is reasonable to assume that the outflow rate $\dot{M}_{out}$ is proportional to the ISM mass of the

[56] Speagle et al. use the age of the universe in their equation. For our purposes, we have assumed an age of the universe at time of observation $t_{obs} = 12.161$ Gyr corresponding to a redshift of $z = 0.1$—the median redshift of the GROUPGALAXY sample for $M_* \geq 10^{9.5}\,M_e$—in our adopted cosmology. The input time to $S(t, M_*)$ is then correctly expressed as $t_i = t_{obs} - i * \Delta t$.

galaxy, i.e., can be reexpressed as

$$\dot{M}_{\rm out} = \frac{1}{t_{\rm res}} M_{\rm ISM}, \quad (27)$$

where the constant of proportionality is cast in terms of a typical residence time $\tau_{\rm res}$ of a unit mass of gas in the ISM.[57] In the following we assume $\tau_{\rm res}$ to be determined by galaxy-specific processes, i.e., to be constant for galaxies of a given stellar mass. $\tau_{\rm res}$ may, however, be expected to vary as a function of stellar mass, e.g., as a result of variations in the ratio of the feedback energy per unit mass to the depth of the potential well. Making use of $\tau_{\rm res}$ as defined above, we can reformulate Equation (26) as

$$\dot{M}_{\rm ISM} = \dot{M}_{\rm in} - \frac{M_{\rm ISM}}{t_{\rm res}} - (1-a)\Psi_*. \quad (28)$$

Empirically, it is well known that star formation and galaxy gas content are connected, with star-forming galaxies, and in particular star-forming spiral galaxies, being found to follow the Schmidt–Kennicutt relation (Schmidt 1959; Kennicutt 1998a), i.e., $\dot{\Sigma}_* \propto \Sigma^n$ with $n \approx 1.5$. Although this empirical relation connects the surface densities of gas and star formation, recent theoretical work (e.g., Krumholz et al. 2012, and references therein) suggests that this results from an underlying volumetric star formation law. Specifically, Krumholz et al. (2012) argue that the underlying physical relation has the form $\rho_* \propto \rho/t_{\rm col}$, where $t_{\rm col} = \sqrt{3\pi/32G\rho}$ is the timescale for the *star-forming cloud* to collapse under its self-gravity. In terms of extragalactic observations, where only surface densities are available, this becomes $\dot{\Sigma}_* \propto \Sigma/t_{\rm col}$. In fact, Krumholz et al. (2012) show that in this formulation objects from giant molecular clouds to high-redshift starburst galaxies all fall on the same relation. In the redshift range considered in this analysis the typical locus of star formation may be assumed to be molecular clouds, for which, to first order, the density, and hence $\tau_{\rm col}$, can be assumed to be constant (Krumholz et al. 2012). Thus, in a spatially integrated form, we can assume

$$\Psi_* = \kappa M_{\rm ISM} \quad (29)$$

and indirectly obtain information on a galaxy's gas content by measuring its SFR.

A caveat to this, however, is the fact that Krumholz et al. (2012) considered only H_2, while our analysis considers the total HI + H_2 in the ISM. The ratio of molecular to total neutral hydrogen will vary with, e.g., galaxy stellar mass, and even if that were not the case, the numerical value needed to link $M_{\rm ISM}$ to Ψ_* would differ from that provided by Krumholz et al. (2012). For the purpose of our analysis, we have therefore chosen to recalibrate κ for the two mass ranges considered, using the fiducial stellar mass for the relevant range in each case ($10^{9.75}$ and $10^{10.3}\,M_\odot$, respectively). To determine the total HI + H_2 gas mass for both values of M_*, we make use of the model of Popping et al. (2014), which shows good agreement with the measurements of Leroy et al. (2008), Saintonge et al. (2011), Catinella et al. (2013), and Boselli et al. (2014). We then use the average SFR derived from our FIELDGALAXY sample at the appropriate masses to empirically determine the constant of proportionality, finding $\kappa = 0.46\,{\rm Gyr}^{-1}$ and $\kappa = 0.47\,{\rm Gyr}^{-1}$ for the low and high stellar mass ranges, respectively.

Inserting Equation (29) into Equation (28), we obtain

$$\dot{M}_{\rm ISM} = \dot{M}_{\rm in} - \frac{M_{\rm ISM}}{t_{\rm res}} - \kappa M_{\rm ISM}, \quad (30)$$

$$= \dot{M}_{\rm in} - \beta\Psi_* - (1-a)\Psi_*, \quad (31)$$

where we have defined $k = (1-a)\kappa$ in Equation (30) and $\beta = 1/(t_{\rm res}\kappa)$ in Equation (31). A volumetric star formation law enables the general time-dependent evolution of the ISM content of a galaxy to be equivalently formulated in terms of ISM mass and SFR.

Finally, considering the last term in Equation (30), we can express the constant of proportionality κ in terms of a timescale $t_{\rm exhaust}$, where

$$t_{\rm exhaust} = \frac{1}{k} = \frac{1}{(1-a)\kappa} \quad (32)$$

corresponds to the exhaustion timescale of the ISM in a closed box model, i.e., due to star formation alone. Inserting Equation (32) in Equation (30), and introducing the effective timescale

$$\tilde{t} = \frac{t_{\rm res}\, t_{\rm exhaust}}{t_{\rm res} + t_{\rm exhuast}}, \quad (33)$$

we obtain

$$\dot{M}_{\rm ISM} = \dot{M}_{\rm in} - \frac{M_{\rm ISM}}{\tilde{t}}, \quad (34)$$

i.e., Equation (15) of Section 9.1.

As stated in Section 9.1, for spiral galaxies in the field, the SFR is found to evolve only very slowly with redshift and is thought to be determined by a self-regulated balance between inflow, outflow, and consumption of the ISM via star formation that only evolves very gradually (Kereš et al. 2005; Davé et al. 2011; Lilly et al. 2013; Saintonge et al. 2013) such that at any given time their SFR can be considered quasi-constant. Via the volumetric star formation law this implies a constraint on $\dot{M}_{\rm ISM}$ that can be used to enable estimates of $\dot{M}_{\rm in}$ from Equations (30) and (31).

As suggested by Lilly et al. (2013), a good description of the quasi-steady state is given by the requirement

$$m = \frac{M_{\rm ISM}}{M_*} = {\rm const.}, \quad (35)$$

i.e., that the ISM mass per unit stellar mass, and accordingly the sSFR, be constant. As these authors show, this formulation allows for the dependence of gas metallicity on SFR, in line with observations. However, as the stellar mass increases, the galaxy will also change its position along the Ψ_*–M_* relation, shifting toward a higher value of M_* and an accordingly lower expected value of the sSFR. Considering a period of time over which the accumulated stellar mass is negligible, an alternative implementation of the quasi-steady state is that the ISM mass remains constant, i.e., $\dot{M}_{\rm ISM} = 0$. Clearly, these scenarios bracket the behavior of $M_{\rm ISM}$ that can be expected in the quasi-steady state. In the following we will derive an estimate of the inflow rate using the requirement given by Equation (35) following Lilly et al. (2013), and subsequently we will compare it to the result obtained using $\dot{M}_{\rm ISM} = 0$.

[57] We note that for a volumetric star formation law, as we will motivate in the following, this formulation is equivalent to the widely used mass-loading parameterization $\dot{M}_{\rm out} = \beta\Psi_*$.

We begin by considering the total time derivative of μ given by

$$\frac{d}{dt}m = \frac{1}{M_*}\frac{\partial M_{\rm ISM}}{\partial t} + \frac{M_{\rm ISM}}{M_*^2}\frac{\partial M_*}{\partial t} \quad (36)$$

$$= \frac{1}{M_*}\frac{\partial M_{\rm ISM}}{\partial t} + \frac{1}{M_*}m(1-a)f, \quad (37)$$

from which we obtain

$$\dot{M}_{\rm ISM} = \frac{\partial M_{\rm ISM}}{\partial t} = m(1-a)f + M_*\frac{d}{dt}m. \quad (38)$$

Inserting Equation (38) into Equation (31) and isolating $M_{\rm in}$, we obtain

$$M_{\rm in} = [(1-a)(1+m) + l]f + M_*\frac{d}{dt}m. \quad (39)$$

As we assume μ to be quasi-constant in the (quasi-)steady state, the term $(d/dt)m$ will be negligible compared to the other terms in Equation (39). Thus, for the quasi-steady state, the inflow of gas to the galaxy will be given by

$$M_{\rm in} \gg [l + (1-a) + m(1-a)]f. \quad (40)$$

Comparing the estimate for the inflow given in Equation (40) with that which can immediately be obtained from Equation (31) for $\dot{M}_{\rm ISM} = 0$, i.e.,

$$\dot{M}_{\rm in} = [l + (1-a)]\mathrm{F}_* = \frac{\mathrm{F}_*}{k\tilde{t}} \quad (41)$$

(where we have made use of Equations (34) and (13) for the last equality), it is clear that the inflow given by Equation (40) is larger by a factor of $m(1-a)$, with the end point of this fraction of the flow being the (growing) ISM of the galaxy. As the actual inflow will lie somewhere between the bracketing cases considered here, we have chosen to adopt Equation (41) as a conservative estimate of the inflow to the galaxy in the quasi-steady state in the context of this work.

Although we have derived an estimate of the inflow of gas into the ISM making use of the quasi-steady state, this is still predicated on our knowledge of the outflow, i.e., of the parameters λ and $\tau_{\rm res}$. To this end, we consider the effective timescale

$$\tilde{t} = \frac{t_{\rm res}\,t_{\rm exhaust}}{t_{\rm res} + t_{\rm exhaust}} = \frac{1}{k(1-a+l)}, \quad (42)$$

from which we obtain

$$l = \frac{1}{k\tilde{t}} + a - 1. \quad (43)$$

As discussed in Section 9.1, independent of any assumptions with regard to the quasi-steady state, $\tilde{t}$ can be determined from the quenching and refueling phase(s) of the fitted parameterized SFHs. Accordingly, the outflow estimate given by Equation (43) holds regardless of steady-state description adopted, and if we adopt Equation (41) as an inflow estimate and insert it into Equation (43), we obtain the expression given by Equation (17) in Section 9.1.

Finally, we reiterate that the derivation presented above with the corresponding approximations will hold as long as the rate at which the inflow changes is small compared to the timescale $\tilde{t}$. For the majority of our considered cases we find the adopted approximations to be retroactively justified, as we find $\tilde{t} \gtrsim 1$ Gyr following Equation (33). Where this is not the case, we can no longer derive meaningful constraints using the equations derived above.

Appendix E
Sampling the Full Distribution of $t_{\rm INFALL}$—Results for Two-parameter Models

For the main purpose of our analysis we have adopted the very conservative assumption that only the youngest 30% of satellite galaxies are spirals (i.e., have retained their spiral morphology), and we have accordingly limited the maximum time since infall in our modeling to $t_{\rm infall} \lesssim 3.77$ Gyr. The opposite extreme assumption is that the group environment has no impact on the probability of a spiral to transform its morphology, in which case it would be appropriate to sample the full distribution of infall times. While this is almost certainly not the case, the true distribution of infall times will lie between these two extremes, albeit likely more on the side of the conservative estimate. Therefore, in order to gain an understanding of the importance of the infall time distribution to the performance of our models, it is informative to consider their performance using the extreme assumption that the full distribution of $t_{\rm infall}$ is sampled. Figures 25, 26, and 27, which are analogous to Figures 18 and 19, show the results of the models using this extreme assumption. We find that all three models are formally capable of reproducing the observed distributions even under the extreme infall time distribution. For the delayed quenching model, the preferred parameter values are $\tau_{\rm quench} = 1.5$ Gyr and $t_{\rm delay} = 4.9$ Gyr, while the preferred values for the stochastic delayed quenching model are $\tau_{\rm quench} = 1.5$ Gyr and $P_{\rm quench} = 0.1\,\mathrm{Gyr}^{-1}$. For both models, the quenching timescales are longer than when assuming the conservative infall time distribution; notably, however, the delay time is much longer, and the quenching probability is lower, expanding beyond realistic estimates of the depletion timescale, as discussed in Section 9.2.4. In contrast, the refueling model prefers parameter values $\tau_{\rm fuel} = 0.98$ Gyr and $P_{\rm quench} = 0.5\,\mathrm{Gyr}^{-1}$, comparable to those previously found, although the refueling is slower and the occurrence of quenching is lower. However, as a comparison of Figures 20 and 27 reveals, the degenerate parameter space is largely the same under both extreme infall time distributions.

In the high stellar mass range, we

In the low stellar mass range, the refueling model best reproduces the observed distribution of $\Delta\log(\psi_*)$, still attaining a value of $Q = 0.79$ for the preferred parameter combination ($\tau_{\rm fuel} = 0.45$ Gyr, $P_{\rm quench} = 0.5\,\mathrm{Gyr}^{-1}$), albeit 0.14 lower than that found for the conservative distribution of infall times and requiring a high rate of recovery. In contrast, the stochastic delayed quenching model ($\tau_{\rm quench} = 3.1$ Gyr, $P_{\rm quench} = 0.1\,\mathrm{Gyr}^{-1}$) and the delayed quenching model ($\tau_{\rm quench} = 3.7$ Gyr, $t_{\rm delay} = 4.3$ Gyr) struggle to reproduce the observed distribution under the adopted infall time distribution, both overpredicting the relative number of largely unquenched galaxies, and in the case of the delayed quenching model, markedly underpredicting the number of strongly quenched galaxies. This is also evident from Figure 27 and Table 5, where the attained values of Q are noticeably lower than for the conservative infall time distribution. Furthermore, the long delay time/low quenching probability is difficult to reconcile with realistic gas exhaustion timescales.

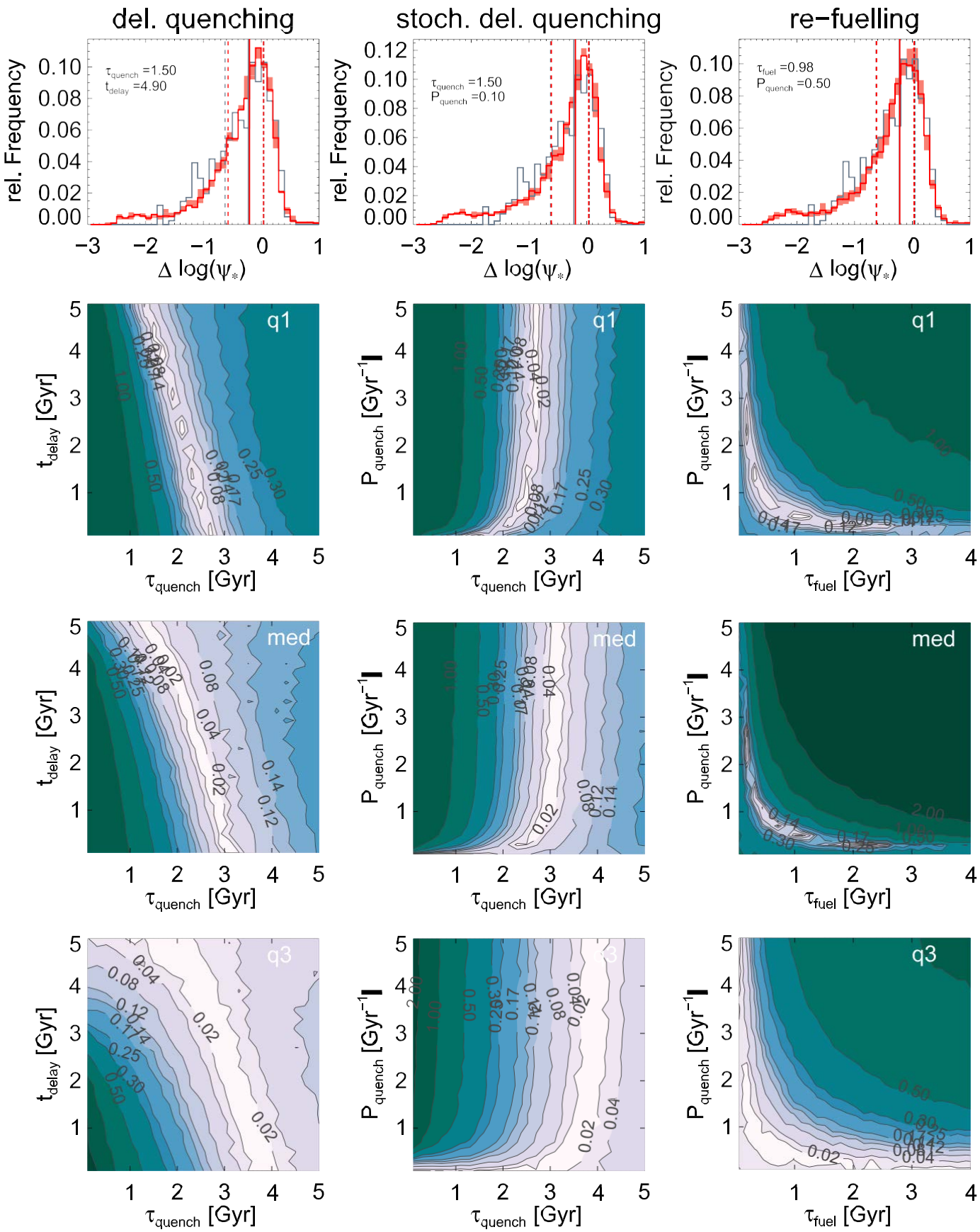

Figure 25. Same as Figure 18, i.e., for the mass range $M_* \sim 10^{10} M_e$, but for models sampling the full distribution of infall times as shown in Figure 24.

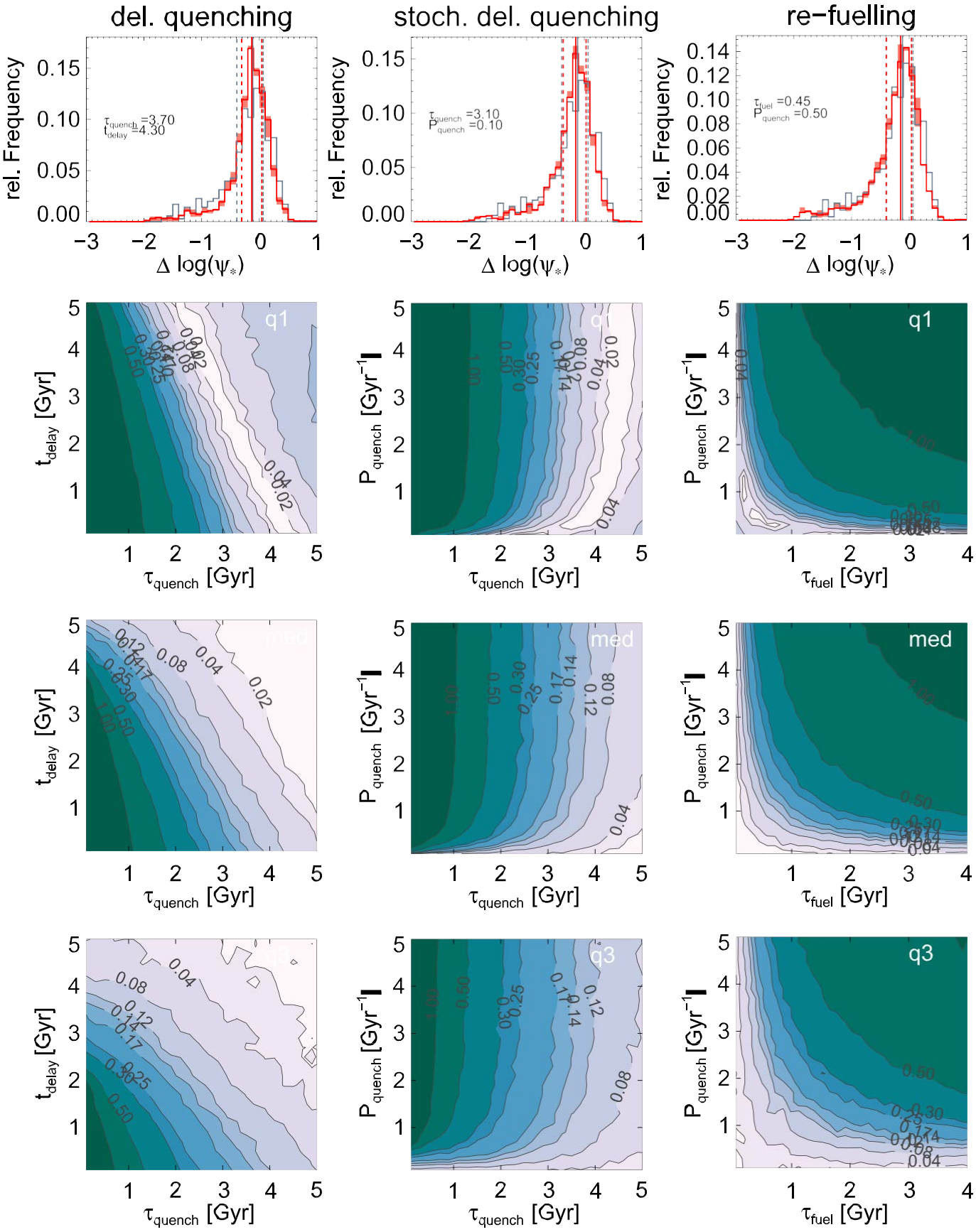

Figure 26. Same as Figure 25, but for the mass range $10^{9.5} M_e \square M* \square 10^{10} M_e$.

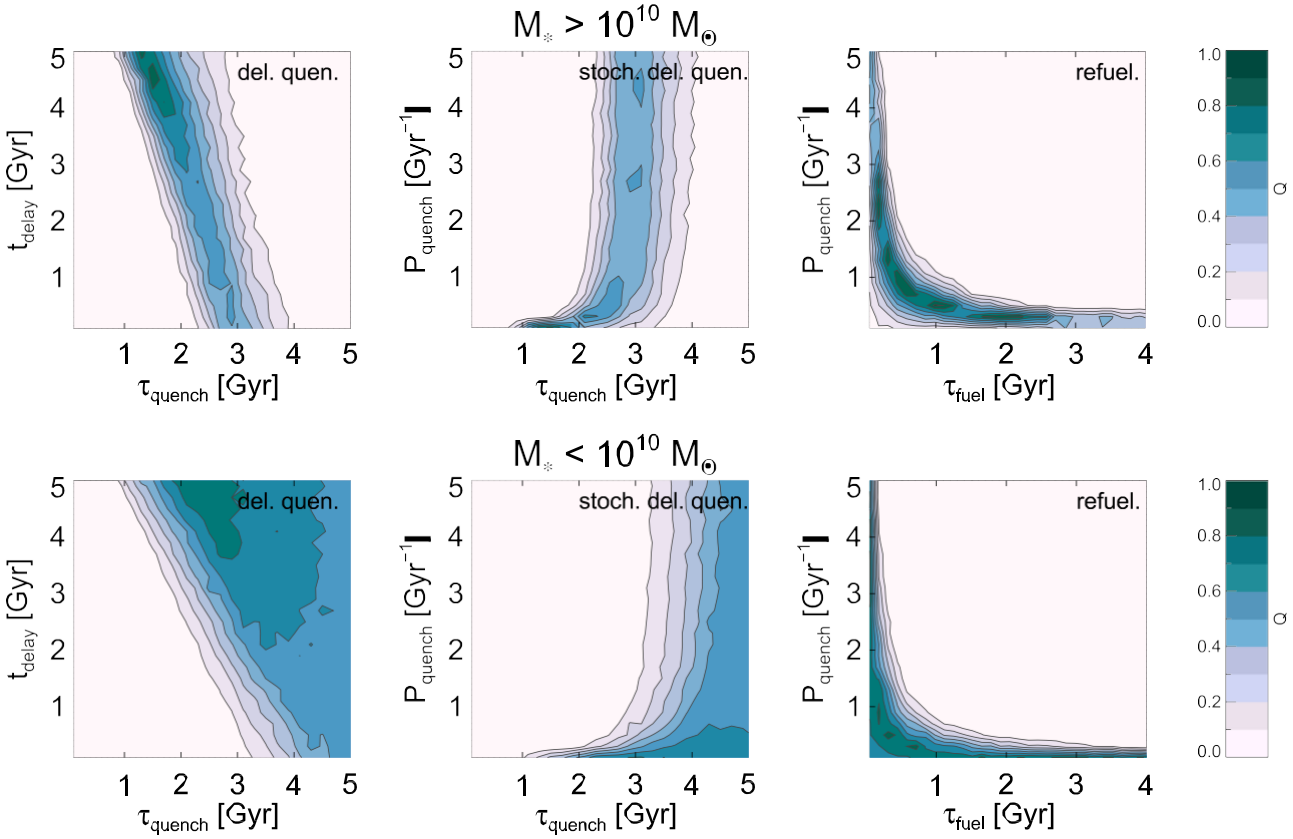

Figure 27. Same as Figure 20, but for models sampling the full distribution of infall times as shown in Figure 24.

References

Abadi, M. G., Moore, B., & Bower, R. G. 1999, MNRAS, 308, 947
Agertz, O., Teyssier, R., & Moore, B. 2011, MNRAS, 410, 1391
Alatalo, K., Appleton, P. N., Lisenfeld, U., et al. 2015, ApJ, 812, 117
Alpaslan, M., Robotham, A. S. G., Driver, S., et al. 2014, MNRAS, 438, 177
Avni, Y., Soltan, A., Tananbaum, H., & Zamorani, G. 1980, ApJ, 238, 800
Bahé, Y. M., & McCarthy, I. G. 2015, MNRAS, 447, 969
Baldry, I. K., Glazebrook, K., Brinkmann, J., et al. 2004, ApJ, 600, 681
Baldry, I. K., Robotham, A. S. G., Hill, D. T., et al. 2010, MNRAS, 404, 86
Balogh, M., Bower, R. G., Smail, I., et al. 2002, MNRAS, 337, 256
Balogh, M. L., Baldry, I. K., Nichol, R., et al. 2004, ApJL, 615, L101
Balogh, M. L., McGee, S. L., Mok, A., et al. 2016, MNRAS, 456, 4364
Bamford, S. P., Nichol, R. C., Baldry, I. K., et al. 2009, MNRAS, 393, 1324
Barton, E. J., Geller, M. J., & Kenyon, S. J. 2000, ApJ, 530, 660
Behroozi, P. S., Wechsler, R. H., & Conroy, C. 2013, ApJL, 762, L31
Benson, A. J., & Bower, R. 2011, MNRAS, 410, 2653
Benson, A. J., Pearce, F. R., Frenk, C. S., Baugh, C. M., & Jenkins, A. 2001, MNRAS, 320, 261
Bertin, E., & Arnouts, S. 1996, A&AS, 117, 393
Bertin, E., Mellier, Y., Radovich, M., et al. 2002, in ASP Conf. Ser. 281, Astronomical Data Analysis Software and Systems XI, ed. D. A. Bohlender, D. Durand, & T. H. Handley (San Francisco, CA: ASP), 228
Bertschinger, E. 1985, ApJS, 58, 39
Bett, P., Eke, V., Frenk, C. S., Jenkins, A., & Okamoto, T. 2010, MNRAS, 404, 1137
Binney, J. 1977, ApJ, 215, 483
Birnboim, Y., & Dekel, A. 2003, MNRAS, 345, 349
Bitsakis, T., Dultzin, D., Ciesla, L., et al. 2016, MNRAS, 459, 957
Blanton, M. R., & Berlind, A. A. 2007, ApJ, 664, 791
Blanton, M. R., & Roweis, S. 2007, AJ, 133, 734
Boselli, A., Cortese, L., Boquien, M., et al. 2014, A&A, 564, A66
Bower, R. G., Benson, A. J., Malbon, R., et al. 2006, MNRAS, 370, 645
Bretherton, C. F., Moss, C., & James, P. A. 2013, A&A, 553, A67
Brooks, A. M., Governato, F., Quinn, T., Brook, C. B., & Wadsley, J. 2009, ApJ, 694, 396
Bruzual, G., & Charlot, S. 2003, MNRAS, 344, 1000
Bullock, J. S., Dekel, A., Kolatt, T. S., et al. 2001, ApJ, 555, 240
Calura, F., Ciotti, L., & Nipoti, C. 2014, MNRAS, 440, 3341
Calzetti, D., Armus, L., Bohlin, R. C., et al. 2000, ApJ, 533, 682
Carollo, C. M., Cibinel, A., Lilly, S. J., et al. 2016, ApJ, 818, 180
Catinella, B., Schiminovich, D., Cortese, L., et al. 2013, MNRAS, 436, 34
Cayatte, V., Kotanyi, C., Balkowski, C., & van Gorkom, J. H. 1994, AJ, 107, 1003
Chabrier, G. 2003, PASP, 115, 763
Chung, A., van Gorkom, J. H., Kenney, J. D. P., Crowl, H., & Vollmer, B. 2009, AJ, 138, 1741
Churchill, C. W., Trujillo-Gomez, S., Nielsen, N. M., & Kacprzak, G. G. 2013, ApJ, 779, 87
Collister, A. A., & Lahav, O. 2005, MNRAS, 361, 415
Cortese, L., Boissier, S., Boselli, A., et al. 2012a, A&A, 544, A101
Cortese, L., Ciesla, L., Boselli, A., et al. 2012b, A&A, 540, A52
Cortese, L., Davies, J. I., Pohlen, M., et al. 2010, A&A, 518, L49
Cucciati, O., Iovino, A., Kovač, K., et al. 2010, A&A, 524, A2
Dalla Vecchia, C., & Schaye, J. 2012, MNRAS, 426, 140
Davé, R., Oppenheimer, B. D., & Finlator, K. 2011, MNRAS, 415, 11
Davies, L. J. M., Driver, S. P., Robotham, A. S. G., et al. 2016, MNRAS, 461, 458
Davies, L. J. M., Robotham, A. S. G., Driver, S. P., et al. 2015, MNRAS, 452, 616
Dekel, A., & Birnboim, Y. 2006, MNRAS, 368, 2
Dekel, A., Birnboim, Y., Engel, G., et al. 2009, Natur, 457, 451
Dekel, A., Zolotov, A., Tweed, D., et al. 2013, MNRAS, 435, 999
Dénes, H., Kilborn, V. A., Koribalski, B. S., & Wong, O. I. 2016, MNRAS, 455, 1294
Dressler, A. 1980, ApJ, 236, 351
Driver, S. P., Hill, D. T., Kelvin, L. S., et al. 2011, MNRAS, 413, 971
Driver, S. P., Popescu, C. C., Tuffs, R. J., et al. 2007, MNRAS, 379, 1022
Dwek, E., & Werner, M. W. 1981, ApJ, 248, 138
Elmegreen, B. G., Struck, C., & Hunter, D. A. 2014, ApJ, 796, 110
Erfanianfar, G., Popesso, P., Finoguenov, A., et al. 2014, MNRAS, 445, 2725
Erfanianfar, G., Popesso, P., Finoguenov, A., et al. 2016, MNRAS, 455, 2839
Fabian, A. C. 2012, ARA&A, 50, 455
Fall, S. M., & Efstathiou, G. 1980, MNRAS, 193, 189

Faucher-Giguère, C.-A., Kereš, D., & Ma, C.-P. 2011, MNRAS, 417, 2982
Feigelson, E. D., & Nelson, P. I. 1985, ApJ, 293, 192
Fillmore, J. A., & Goldreich, P. 1984, ApJ, 281, 1
Fumagalli, M., Fossati, M., Hau, G. K. T., et al. 2014, MNRAS, 445, 4335
Gavazzi, G., Fumagalli, M., Fossati, M., et al. 2013, A&A, 553, A89
Geach, J. E., Smail, I., Moran, S. M., et al. 2011, ApJL, 730, L19
Genel, S., Fall, S. M., Hernquist, L., et al. 2015, ApJL, 804, L40
George, M. R., Ma, C.-P., Bundy, K., et al. 2013, ApJ, 770, 113
Gómez, P. L., Nichol, R. C., Miller, C. J., et al. 2003, ApJ, 584, 210
Goto, T., Yamauchi, C., Fujita, Y., et al. 2003, MNRAS, 346, 601
Governato, F., Willman, B., Mayer, L., et al. 2007, MNRAS, 374, 1479
Graham, A. W., & Worley, C. C. 2008, MNRAS, 388, 1708
Grootes, M. W., Tuffs, R. J., Popescu, C. C., et al. 2013, ApJ, 766, 59
Grootes, M. W., Tuffs, R. J., Popescu, C. C., et al. 2014, MNRAS, 437, 3883
Gunn, J. E., & Gott, J. R., III 1972, ApJ, 176, 1
Haas, M. R., Schaye, J., & Jeeson-Daniel, A. 2012, MNRAS, 419, 2133
Hahn, O., Teyssier, R., & Carollo, C. M. 2010, MNRAS, 405, 274
Hashimoto, Y., Oemler, A., Jr., Lin, H., & Tucker, D. L. 1998, ApJ, 499, 589
Hester, J. A. 2006, ApJ, 647, 910
Hester, J. A. 2010, ApJ, 720, 191
Hickox, R. C., Mullaney, J. R., Alexander, D. M., et al. 2014, ApJ, 782, 9
Hill, D. T., Kelvin, L. S., Driver, S. P., et al. 2011, MNRAS, 412, 765
Hodges-Kluck, E., & Bregman, J. N. 2014, ApJ, 789, 131
Hopkins, A. M., Driver, S. P., Brough, S., et al. 2013, MNRAS, 430, 2047
Hopkins, A. M., McClure-Griffiths, N. M., & Gaensler, B. M. 2008, ApJL, 682, L13
Hubble, E., & Humason, M. L. 1931, ApJ, 74, 43
James, P. A., Knapen, J. H., Shane, N. S., Baldry, I. K., & de Jong, R. S. 2008, A&A, 482, 507
Jeltema, T. E., Mulchaey, J. S., Lubin, L. M., Rosati, P., & Böhringer, H. 2006, ApJ, 649, 649
Karim, A., Schinnerer, E., Martínez-Sansigre, A., et al. 2011, ApJ, 730, 61
Kauffmann, G., White, S. D. M., Heckman, T. M., et al. 2004, MNRAS, 353, 713
Kawata, D., & Mulchaey, J. S. 2008, ApJL, 672, L103
Kelvin, L. S., Driver, S. P., Robotham, A. S. G., et al. 2012, MNRAS, 421, 1007
Kelvin, L. S., Driver, S. P., Robotham, A. S. G., et al. 2014, MNRAS, 439, 1245
Kennicutt, R. C., Jr. 1998a, ApJ, 498, 541
Kennicutt, R. C., Jr. 1998b, ARA&A, 36, 189
Kereš, D., Katz, N., Fardal, M., Davé, R., & Weinberg, D. H. 2009, MNRAS, 395, 160
Kereš, D., Katz, N., Weinberg, D. H., & Davé, R. 2005, MNRAS, 363, 2
Kewley, L. J., Dopita, M. A., Sutherland, R. S., Heisler, C. A., & Trevena, J. 2001, ApJ, 556, 121
Kimm, T., Somerville, R. S., Yi, S. K., et al. 2009, MNRAS, 394, 1131
Koopmann, R. A., & Kenney, J. D. P. 1998, ApJL, 497, L75
Koopmann, R. A., & Kenney, J. D. P. 2004, ApJ, 613, 866
Krumholz, M. R., Dekel, A., & McKee, C. F. 2012, ApJ, 745, 69
Lagos, C. D. P., Baugh, C. M., Lacey, C. G., et al. 2011, MNRAS, 418, 1649
Lange, R., Moffett, A. J., Driver, S. P., et al. 2016, MNRAS, 462, 1470
Larson, R. B., Tinsley, B. M., & Caldwell, C. N. 1980, ApJ, 237, 692
Lee, N., Sanders, D. B., Casey, C. M., et al. 2015, ApJ, 801, 80
Leitherer, C., Ekström, S., Meynet, G., et al. 2014, ApJS, 212, 14
Leitherer, C., Schaerer, D., Goldader, J. D., et al. 1999, ApJS, 123, 3
Leroy, A. K., Walter, F., Brinks, E., et al. 2008, AJ, 136, 2782
Lewis, I., Balogh, M., De Propris, R., et al. 2002, MNRAS, 334, 673
Lilly, S. J., Carollo, C. M., Pipino, A., Renzini, A., & Peng, Y. 2013, ApJ, 772, 119
Lintott, C., Schawinski, K., Bamford, S., et al. 2011, MNRAS, 410, 166
Liske, J., Baldry, I. K., Driver, S. P., et al. 2015, MNRAS, 452, 2087
Loeb, A. 2008, First Light (Heidelberg: Springer-Verlag)
MacArthur, L. A., González, J. J., & Courteau, S. 2009, MNRAS, 395, 28
Martin, D. C., Fanson, J., Schiminovich, D., et al. 2005, ApJL, 619, L1
Masters, K. L., Nichol, R., Bamford, S., et al. 2010, MNRAS, 404, 792
Matsuura, M., Barlow, M. J., Zijlstra, A. A., et al. 2009, MNRAS, 396, 918
Matsuura, M., Woods, P. M., & Owen, P. J. 2013, MNRAS, 429, 2527
McBride, J., Fakhouri, O., & Ma, C.-P. 2009, MNRAS, 398, 1858
McCarthy, I. G., Frenk, C. S., Font, A. S., et al. 2008, MNRAS, 383, 593
McGee, S. L., Bower, R. G., & Balogh, M. L. 2014, MNRAS, 442, L105
Merson, A. I., Baugh, C. M., Helly, J. C., et al. 2013, MNRAS, 429, 556
Mo, H. J., Mao, S., & White, S. D. M. 1998, MNRAS, 295, 319
Möllenhoff, C., Popescu, C. C., & Tuffs, R. J. 2006, A&A, 456, 941
Montier, L. A., & Giard, M. 2004, A&A, 417, 401
Morrissey, P., Conrow, T., Barlow, T. A., et al. 2007, ApJS, 173, 682
Moster, B. P., Somerville, R. S., Maulbetsch, C., et al. 2010, ApJ, 710, 903
Nair, P. B., & Abraham, R. G. 2010, ApJS, 186, 427
Natale, G., Tuffs, R. J., Xu, C. K., et al. 2010, ApJ, 725, 955
Nelson, D., Vogelsberger, M., Genel, S., et al. 2013, MNRAS, 429, 3353
Noeske, K. G., Weiner, B. J., Faber, S. M., et al. 2007, ApJL, 660, L43
Ojha, D. K., Tej, A., Schultheis, M., Omont, A., & Schuller, F. 2007, MNRAS, 381, 1219
Oke, J. B., & Gunn, J. E. 1983, ApJ, 266, 713
Oosterloo, T., Morganti, R., Crocker, A., et al. 2010, MNRAS, 409, 500
Pappalardo, C., Bianchi, S., Corbelli, E., et al. 2012, A&A, 545, A75
Pasquali, A., Gallazzi, A., & van den Bosch, F. C. 2012, MNRAS, 425, 273
Pasquali, A., van den Bosch, F. C., Mo, H. J., Yang, X., & Somerville, R. 2009, MNRAS, 394, 38
Pastrav, B. A., Popescu, C. C., Tuffs, R. J., & Sansom, A. E. 2013a, A&A, 553, A80
Pastrav, B. A., Popescu, C. C., Tuffs, R. J., & Sansom, A. E. 2013b, A&A, 557, A137
Pavlovski, G., & Pope, E. C. D. 2009, MNRAS, 399, 2195
Peeples, M. S., Werk, J. K., Tumlinson, J., et al. 2014, ApJ, 786, 54
Peng, Y., Maiolino, R., & Cochrane, R. 2015, Natur, 521, 192
Peng, Y.-j., Lilly, S. J., Kovač, K., et al. 2010, ApJ, 721, 193
Peng, Y.-j., Lilly, S. J., Renzini, A., & Carollo, M. 2012, ApJ, 757, 4
Peng, Y.-j., & Maiolino, R. 2014, MNRAS, 438, 262
Peto, R., & Peto, J. 1972, Journal of the Royal Statistical Society. Series A (General), 135, 185
Pfleiderer, J., & Krommidas, P. 1982, MNRAS, 198, 281
Pichon, C., Pogosyan, D., Kimm, T., et al. 2011, MNRAS, 418, 2493
Pimbblet, K. A., Smail, I., Edge, A. C., et al. 2006, MNRAS, 366, 645
Pimbblet, K. A., Smail, I., Kodama, T., et al. 2002, MNRAS, 331, 333
Pope, E. C. D. 2007, MNRAS, 381, 741
Popescu, C. C., Tuffs, R. J., Dopita, M. A., et al. 2011, A&A, 527, A109
Popescu, C. C., Tuffs, R. J., Fischera, J., & Völk, H. 2000, A&A, 354, 480
Popescu, C. C., Tuffs, R. J., Völk, H. J., Pierini, D., & Madore, B. F. 2002, ApJ, 567, 221
Popping, G., Somerville, R. S., & Trager, S. C. 2014, MNRAS, 442, 2398
Rees, M. J., & Ostriker, J. P. 1977, MNRAS, 179, 541
Robotham, A., Driver, S. P., Norberg, P., et al. 2010, PASA, 27, 76
Robotham, A., Wallace, C., Phillipps, S., & De Propris, R. 2006, ApJ, 652, 1077
Robotham, A. S. G., Driver, S. P., Davies, L. J. M., et al. 2014, MNRAS, 444, 3986
Robotham, A. S. G., Liske, J., Driver, S. P., et al. 2013, MNRAS, 431, 167
Robotham, A. S. G., Norberg, P., Driver, S. P., et al. 2011, MNRAS, 416, 2640
Saintonge, A., Kauffmann, G., Kramer, C., et al. 2011, MNRAS, 415, 32
Saintonge, A., Lutz, D., Genzel, R., et al. 2013, ApJ, 778, 2
Salim, S., Rich, R. M., Charlot, S., et al. 2007, ApJS, 173, 267
Salpeter, E. E. 1955, ApJ, 121, 161
Sánchez-Blázquez, P., Ocvirk, P., Gibson, B. K., Pérez, I., & Peletier, R. F. 2011, MNRAS, 415, 709
Sánchez-Blázquez, P., Rosales-Ortega, F. F., Méndez-Abreu, J., et al. 2014, A&A, 570, A6
Schlegel, D. J., Finkbeiner, D. P., & Davis, M. 1998, ApJ, 500, 525
Schmidt, M. 1959, ApJ, 129, 243
Schreiber, C., Pannella, M., Elbaz, D., et al. 2015, A&A, 575, A74
Seon, K.-i., Witt, A. N., Shinn, J.-h., & Kim, I.-j. 2014, ApJL, 785, L18
Simard, L., Mendel, J. T., Patton, D. R., Ellison, S. L., & McConnachie, A. W. 2011, ApJS, 196, 11
Skibba, R. A., Bamford, S. P., Nichol, R. C., et al. 2009, MNRAS, 399, 966
Smail, I., Edge, A. C., Ellis, R. S., & Blandford, R. D. 1998, MNRAS, 293, 124
Smith, M. W. L., Gomez, H. L., Eales, S. A., et al. 2012, ApJ, 748, 123
Sommer-Larsen, J., Gelato, S., & Vedel, H. 1999, ApJ, 519, 501
Speagle, J. S., Steinhardt, C. L., Capak, P. L., & Silverman, J. D. 2014, ApJS, 214, 15
Spergel, D. N., Verde, L., Peiris, H. V., et al. 2003, ApJS, 148, 175
Springel, V., White, S. D. M., Jenkins, A., et al. 2005, Natur, 435, 629
Tacconi, L. J., Genzel, R., Neri, R., et al. 2010, Natur, 463, 781
Taylor, E. N., Hopkins, A. M., Baldry, I. K., et al. 2011, MNRAS, 418, 1587
Tielens, A. G. G. M. 2005, The Physics and Chemistry of the Interstellar Medium (Cambridge: Cambridge Univ. Press)
Torrey, P., Vogelsberger, M., Sijacki, D., Springel, V., & Hernquist, L. 2012, MNRAS, 427, 2224
Tuffs, R. J., Popescu, C. C., Pierini, D., et al. 2002, ApJS, 139, 37
Tuffs, R. J., Popescu, C. C., Völk, H. J., Kylafis, N. D., & Dopita, M. A. 2004, A&A, 419, 821
Tumlinson, J., Thom, C., Werk, J. K., et al. 2011, Sci, 334, 948

Tumlinson, J., Thom, C., Werk, J. K., et al. 2013, ApJ, 777, 59
Übler, H., Naab, T., Oser, L., et al. 2014, MNRAS, 443, 2092
Urquhart, S. A., Willis, J. P., Hoekstra, H., & Pierre, M. 2010, MNRAS, 406, 368
van de Voort, F., Schaye, J., Booth, C. M., Haas, M. R., & Dalla Vecchia, C. 2011, MNRAS, 414, 2458
van den Bosch, F. C., Abel, T., Croft, R. A. C., Hernquist, L., & White, S. D. M. 2002, ApJ, 576, 21
van den Bosch, F. C., Pasquali, A., Yang, X., et al. 2008, arXiv: 0805.0002
van der Wel, A., Bell, E. F., Holden, B. P., Skibba, R. A., & Rix, H.-W. 2010, ApJ, 714, 1779
Vogelsberger, M., Genel, S., Sijacki, D., et al. 2013, MNRAS, 436, 3031
Weinmann, S. M., Kauffmann, G., von der Linden, A., & De Lucia, G. 2010, MNRAS, 406, 2249
Weinmann, S. M., van den Bosch, F. C., Yang, X., & Mo, H. J. 2006, MNRAS, 366, 2
Werner, N., Oonk, J. B. R., Sun, M., et al. 2014, MNRAS, 439, 2291
Wetzel, A. R., & Nagai, D. 2015, ApJ, 808, 40
Wetzel, A. R., Tinker, J. L., Conroy, C., & Bosch, F. C. v. d. 2014, MNRAS, 439, 2687
Wetzel, A. R., Tinker, J. L., Conroy, C., & van den Bosch, F. C. 2013, MNRAS, 432, 336
Wheeler, C., Phillips, J. I., Cooper, M. C., Boylan-Kolchin, M., & Bullock, J. S. 2014, MNRAS, 442, 1396
Whitaker, K. E., van Dokkum, P. G., Brammer, G., & Franx, M. 2012, ApJL, 754, L29
White, S. D. M., & Frenk, C. S. 1991, ApJ, 379, 52
White, S. D. M., & Rees, M. J. 1978, MNRAS, 183, 341
Wuyts, S., Förster Schreiber, N. M., van der Wel, A., et al. 2011, ApJ, 742, 96
Wyder, T. K., Martin, D. C., Schiminovich, D., et al. 2007, ApJS, 173, 293
Yuan, T.-T., Kewley, L. J., & Richard, J. 2013, ApJ, 763, 9
Zehavi, I., Zheng, Z., Weinberg, D. H., et al. 2011, ApJ, 736, 59